

Creep behaviour of Magnesia Carbon refractory

Investigating the influence of binder and
aluminium content on creep development

Marlee Spreij



Delft University of Technology

Creep behaviour of Magnesia Carbon refractory

Investigating the influence of binder and
aluminium content on creep development

by

Marlee Spreij

Student number: 4445775

In partial fulfilment of the requirements of the degree of

Master of Science

in Materials Science and Engineering

Supervisors: Dr. Vera Popovich
Drs. Fons Vermeulen
Dr. Bruno Luchini
Ir. Pieter Put

Thesis committee: Dr. Vera Popovich
Prof.Dr.Ir. Jilt Sietsma
Ir. Zhaoying Ding
Dr. Bruno Luchini

Project duration: November 15, 2021 - August 29, 2022

Defense date and time: August 29, 2022 at 13:00h

Delft University of Technology

Faculty of Mechanical, Maritime and Materials engineering

in collaboration with Tata Steel IJmuiden

Abstract

Refractories are widely used as lining material in the steelmaking industry. This class of materials is known for its superior creep resistance. However, creep of refractory linings is a known phenomenon in refractory science. Therefore, knowledge on creep behaviour is critical for furnace lining life predictions and selection of materials. This work, in collaboration with Tata Steel IJmuiden, focuses on creep development in magnesia carbon (MgO-C), a refractory often found in Basic Oxygen Furnaces (BOF).

In this research, the influence of binder and aluminium content on creep development in MgO-C was investigated. This was addressed, based on the microstructural changes, phase transformations and thermo-mechanical properties. Microscopy, scanning electron microscopy, X-Ray diffraction, cold crushing strength, hot modulus of rupture, dilatometry, refractoriness under load and hot compressive strength tests were conducted in order to explain creep behaviour. For creep testing, a non-standardised set-up was designed to be able to retrieve creep data more efficiently. The experimental configuration increased the load every 5 hours (multi-stage). Resulting creep rates were validated against a single-load stage creep measurement. A small difference of 5% in creep rates was observed. This indicated that the multi- and single-stage results are within range of each other. Therefore, the proposed multi-stage creep test can be considered a viable creep testing method.

A trend of decreasing creep rates with increasing binder content was found. Increasing the content from 2% to 3% showed a maximum decrease in creep rates of 80%. A further increase of binder content from 3% to 4% showed a maximum decrease in creep rates of 30%. This behaviour was mainly attributed due to volatilisation of the binder and magnesium, and densification due to carbonisation of the binder. Increasing the aluminium content from 0 to 1% resulted in a maximum decrease in creep rates of 70%. This was mainly attributed due to spinel formation. The irreversible volume expansion due to spinel formation, increased the density and the stress state within the material. As a result, micro cracks formed which strengthened the material and improved creep resistance. The outcomes of this work are an important contribution to refractory science. However, further development of refractories is still necessary, especially due to the increasing pressure on the steelmaking sector to make its processes more sustainable.

Acknowledgement

Dear reader,

The master thesis lying in front of you is part of my Material Science and Engineering master, and presents the work I performed in collaboration with the company Tata Steel IJmuiden. After following Dr. Popovich's course on Materials at High Temperatures, I found my passion in material science: materials which are used in high temperature applications. With this in mind I embarked on my search of finding a company to collaborate with for my thesis. My desire was to collaborate, since this would provide me with the opportunity to work on something that could contribute to solving very practical (societal) problems. Moreover, in times of COVID-19 it enabled me to get out of the house more often, which was a very welcome change of scenery. I like being among people, and I could not have wished for nicer colleagues than I got to work with during my time at Tata Steel IJmuiden. Doing a master thesis during a pandemic is not always easy and straight-forward and can work demotivating at times, but I am glad that I was able to make the most out of it as the last part of my "adventure" at Delft University of Technology.

I could not have done all that on my own, but fortunately I had some help during the past 9 months. Firstly, I want to thank Fons for his support during my project. You were always able to provide me with new insights and ideas. Even though you were often quite busy, you always found time to help me out. I especially improved my writing skills thanks to you. At least, I'll let you, the reader, be the judge of that. Secondly I would like to thank Bruno for your help along the way. You made me feel appreciated and you stimulated me to keep improving my work. I enjoyed our biweekly meetings, where you and I would brainstorm on certain theories that I may have had. I learned a lot from you, not just regarding this thesis topic, but also about soft skills when working in a company. Thirdly, I would like to thank Pieter for helping me perform the creep measurements. We overcame some hardships together, regarding the creep testing machinery. In the end, you helped provide me with substantial data that formed the entire basis of this thesis. Furthermore, I want to thank Vera for her guidance during this thesis. You were always able to provide me with insights from a different kind of perspective. You always found things I could improve on, which greatly helped me shape the final version of this thesis. And of course, thanks to all other colleagues at Tata Steel IJmuiden for all the help during these past months. In addition, thanks to all the interns for keeping me sane and distracting me whenever I needed a (mental) break.

Other people I would like to thank are: Jilt Sietsma and Zhaoying Ding for taking the time to be in my thesis committee. A massive thanks also to Tim, for allowing me to express my love-hate relationship with my thesis to every so often. You were always able to keep me cool, calm and collected. Sometimes more than others. I'm also thankful for my dad, who often tried to help me over a glass of craft beer (or two). I look forward to discussing more work-related issues with you in the future. Finally, a huge thank you to my family, housemates and friends, who supported me enormously and helped me through some difficult moments.

I hope you enjoy your reading and hereby I proudly present to you: my master thesis.

*Marlee Spreij
Delft, August 2022*

Contents

Nomenclature	iv
List of Figures	v
List of Tables	vii
1 Introduction	1
2 Theoretical Background	3
2.1 Basic Oxygen Steelmaking	3
2.2 Refractory linings	3
2.3 Creep behaviour of refractories	4
2.3.1 Effect of binder content on creep	5
2.3.2 Effect of aluminium content on creep	6
3 Materials and Methods	8
3.1 Materials	8
3.2 Methods	9
3.2.1 Microstructural characterisation	9
3.2.2 Mechanical characterisation	9
3.2.3 Creep testing	11
3.2.4 Creep modeling	16
4 Results and Discussion	18
4.1 Microstructural characterisation	18
4.2 X-Ray Diffraction	22
4.3 Permanent linear change (PLC)	23
4.4 Cold crushing strength (CCS)	24
4.5 Hot modulus of rupture (HMOR)	25
4.6 Dilatometry	26
4.7 Refractoriness under load (RuL)	28
4.8 Hot compressive strength (HCS)	29
4.9 Creep in compression	29
4.9.1 Effect of increasing binder content on creep development	38
4.9.2 Effect of increasing aluminium content on creep development	39
5 Conclusion and Recommendations	41
5.1 Conclusions	41
5.2 Recommendations	42
References	45
A Processing	46
A.1 Pressing of refractory bricks	46
B Materials and Methods	49
C Results experiments	56
C.1 Microstructural characterisation	56
C.2 XRD	60
C.3 Refractoriness under load	64
C.4 Hot compressive strength	66
C.5 Creep in compression	68

Nomenclature

Abbreviations

Abbreviation	Definition
BOF	Basic Oxygen Furnace
BOS	Basic Oxygen Steelmaking
CCS	Cold Crushing Strength
CIC	Creep in Compression
CTE	Coefficient of Thermal Expansion
EAF	Electric Arc Furnace
EDS	Energy Dispersive Spectroscopy
FEM	Finite Element Modelling
HCS	Hot Compressive Strength
HMOR	Hot Modulus of Rupture
MA	Magnesium Aluminate
MgO-C	Magnesia-carbon
PLC	Permanent Linear Change
RuL	Refractoriness under Load
SEM	Scanning Electron Microscope
UCS	Ultimate Compressive Strength
XRD	X-Ray Diffraction

Symbols

Symbol	Definition	Unit
C_1	Model coefficient	$[\frac{1}{Pa \cdot s}]$
C_2	Model coefficient	[-]
C_3	Model coefficient	[K]
d	Displacement	[mm]
E	Youngs Modulus	[MPa]
L	Sample length	[mm]
p	Pressure	[MPa]
t	Time	[h]
T_M	Temperature	[°C]
T_M	Melting temperature	[°C]
T_g	Glass transition temperature	[°C]
ε	Strain	[-]
ε_{tot}	Total strain	[-]
ε_{el}	Elastic strain	[-]
ε_{pl}	Plastic strain	[-]
ε_{cr}	Creep strain	[-]
$\dot{\varepsilon}_{cr}$	Creep strain rate	[1/s]
$\ddot{\varepsilon}_{cr}$	Creep strain acceleration	[1/s ²]
σ	Load	[MPa]
ρ	Density	[kg/m ³]

List of Figures

2.1	Schematic representation of the BOF [11].	3
2.2	Three stages of creep with creep strain (ε_{cr}), strain rate ($\dot{\varepsilon}_{cr}$) and acceleration of strain rate ($\ddot{\varepsilon}_{cr}$) [13].	5
2.3	Crystal structure and formation mechanism of Magnesium Aluminate spinel.	6
3.1	Experimental setup of the compressive creep testing rig at the CRC at Tata Steel IJmuiden.	11
3.2	Schematic representation of sample set up. Sample is protected by graphite rings, pet coke, a TFF 180 alumina ring and Alsint alumina disks.	12
3.3	Schematic representation of multi stage creep measurement.	13
3.4	Schematic stress-strain curve. Black curve indicates regular loading-unloading curve. Blue curve shows results for a creep test. Dotted lines indicate unloading path.	14
3.5	Example of a schematic strain curve.	15
3.6	Example of a schematic strain rate curve.	15
3.7	Flow chart of the creep testing methodology	17
4.1	Microscopy image of a green PMC-3% binder sample. Microscopy image shows top-view of a cylindrical sample	19
4.2	Microscopy image of a PMC-2% binder sample, fired at 1350 °C. Microscopy image shows lengthwise cross section of a cylindrical creep sample.	20
4.3	Microscopy image of a PMC-4% binder sample, fired at 1350 °C. Microscopy image shows lengthwise cross section of a cylindrical creep sample.	20
4.4	SEM image of a PMC-3% binder-1% Al green sample. Image shows aluminium (Al), magnesia (MgO), graphite (G) and impurities (i).	21
4.5	SEM image of a PMC-3% binder-1% Al sample, pre-treated at 1500 °C. Image shows carbides (AC), whiskers, MA spinel (MAS) and magnesia (MgO).	22
4.6	Cold crushing strength of all recipes versus binder content.	24
4.7	Hot modulus of rupture of all recipes, tested at 1400 °C.	25
4.8	Hot modulus of rupture of all recipes, tested at 1500 °C.	26
4.9	Dilatometry curve of a PMC-2% binder sample.	26
4.10	Dilatometry curve of a PMC-3% binder sample (left) and a PMC-4% binder sample (right).	27
4.11	Dilatometry curve of a PMC-3% binder-1% Al sample (left) and a PMC-3% binder-3% Al sample (right).	28
4.12	Experimental strain curve of PMC-3% binder T = 1500 °C.	30
4.13	Experimental strain rates of a multi stage measurement, testing a PMC-3% binder sample at T = 1500 °C.	30
4.14	Experimental strain rates for a single stage measurement at 8 MPa for a PMC-3% binder sample at T=1500 °C.	31
4.15	Modelled creep rate isoplot for PMC-2% binder recipe.	33
4.16	Modelled creep rate isoplot for PMC-3% binder recipe.	34
4.17	Modelled creep rate isoplot for PMC-4% binder recipe.	34
4.18	Modelled creep rate isoplot for PMC-3% binder-1% Al recipe.	35
4.19	Differences in creep rates between PMC-2% binder and PMC-3% binder.	36
4.20	Differences in creep rates between PMC-3% binder and PMC-4% binder.	36
4.21	Differences in creep rates between PMC-3% binder and PMC-3% binder-1% Al.	37
A.1	Weighing the raw materials	46
A.2	Mixer (A) with operating cabinet (B), heating unit (C), extractor hood (O), cover (P), rod used to tip over and empty the mixer (Q) and security handle (R).	47
A.3	Hydraulic press used to make the refractory bricks	47

A.4	Final bricks after pressing	48
B.1	Recipe for PMC-2% binder.	51
B.2	Recipe for PMC-3% binder.	52
B.3	Recipe for PMC-4% binder.	53
B.4	Recipe for PMC-3% binder-1% Al.	54
B.5	Recipe for PMC-3% binder-3% Al.	55
C.1	Detailed overview of a green PMC-3%-binder sample. Taken at magnification of 5 times.	56
C.3	Mozaic image of a PMC-3%-binder sample that has been fired at 1600 °C.	57
C.4	Mozaic image of a PMC-3% binder-1% Al sample that has been fired at 1500 °C. Yellow square indicates location where SEM was performed.	58
C.5	Image of a PMC-3% binder-1% Al sample that has been fired at 1500 °C. Yellow square indicates location where SEM was performed.	59
C.6	PMC-2% binder sample after creep testing.	60
C.7	Recorded and fitted X-ray pattern along with phase proportions of green PMC-2%-binder sample. Reported Rwp=10.59	60
C.8	Recorded and fitted X-ray pattern along with phase proportions of green PMC-3%-binder sample. Reported Rwp=9.54	61
C.9	Recorded and fitted X-ray pattern along with phase proportions of green PMC-4%-binder sample. Reported Rwp=9.91	61
C.10	Recorded and fitted X-ray pattern along with phase proportions of green PMC-3% binder-1% Al sample. Reported Rwp=8.39	62
C.11	Recorded and fitted X-ray pattern along with phase proportions of green PMC-3% binder-3% Al sample. Reported Rwp=8.47	62
C.12	Recorded and fitted X-ray pattern along with phase proportions of pre-treated PMC-3% binder-1% Al sample.	63
C.13	Recorded and fitted X-ray pattern along with phase proportions of pre-treated PMC-3% binder-1% Al sample.	63
C.14	Refractoriness under load curve of a PMC-2% binder sample.	64
C.15	Refractoriness under load curve of a PMC-3% binder sample.	64
C.16	Refractoriness under load curve of a PMC-4% binder sample.	65
C.17	Refractoriness under load curve of a PMC-3% binder-1% Al sample.	65
C.18	Refractoriness under load curve of a PMC-3% binder-3% Al sample.	66
C.19	Hot compressive strength, tested at 1400 and 1500 ° for PMC-2% binder.	66
C.20	Hot compressive strength, tested at 1400 and 1500 °C for PMC-3% binder.	67
C.21	Hot compressive strength, tested at 1400 and 1500 °C for PMC-4% binder.	67
C.22	Hot compressive strength, tested at 1400 and 1500 °C for PMC-3% binder-1% Al.	68
C.23	Accepted and rejected data for PMC-2% binder recipe.	68
C.24	Accepted and rejected data for PMC-3% binder recipe..	69
C.25	Accepted and rejected data for PMC-4% binder recipe.	69
C.26	Accepted and rejected data for PMC-3% binder-1% Al recipe.	70
C.27	Residual modelled creep rates. Determined by subtracting rates from PMC-4% binder from PMC-2% binder data.	70
C.28	Residual modelled creep rates. Determined by subtracting rates from PMC-3% binder from PMC-2% binder data.	71
C.29	Residual modelled creep rates. Determined by subtracting rates from PMC-4% binder from PMC-3% binder data.	71

List of Tables

2.1	Thermal and Physical properties of $MgAl_2O_4$, MgO and Al_2O_3 at 1000 °C [14, 6].	7
3.1	Raw materials used for all recipes.	8
3.2	Additives of each refractory brick.	8
4.1	Phase distributions of all the recipes. n.d. not detected; with detection limit of $\pm 0.5\text{wt}\%$. 22	
4.2	Phase distributions of a PMC-3% binder-1% Al sample after pre-treating at 1400 °C and 1500 °C.	23
4.3	Bulk densities and porosities of green samples (before heat treatment) and after heating up, and permanent linear change of all recipes. Experiments were conducted at room temperature.	23
4.4	Coefficients of thermal expansion for all recipes, determined between 1000-1600 °C. * measured in non-reducing atmosphere.	28
4.5	Refractoriness under load results for all recipes.	28
4.6	Ultimate compressive strength values measured at 1400 °C and 1500 °C.	29
4.7	Creep rates with corresponding loads for single and multi stage experiment.	31
4.8	Experimental pressures, temperatures and creep rates that were used for the model.	32
4.9	Model coefficients for all recipes. Recall: $\dot{\epsilon}_{II} = C_1 \cdot \sigma^{C_2} \cdot e^{-(C_3/T)}$ where $C_1 = A, C_2 = n, C_3 = \frac{Q_{act}}{R}$	33
4.10	Experimental and modelled creep rates and their corresponding differences.	35
4.11	R^2 for all recipes.	35

Introduction

In the steelmaking industry, refractories are used as lining material in various installations. Different refractories are used, depending on the type and location within the installation. Iron and steel ladles, basic oxygen furnaces (BOF) and electric arc furnaces (EAF) are few of many installations where refractories are found. The main characteristic of refractory materials are excellent heat resistance due to their high melting temperatures. This is a necessity during steelmaking, as this industry operates under extreme conditions. Temperatures as high as 1600 °C may for instance be reached when a BOF is in commission. Refractories play a vital role, protecting many installations from these extreme conditions. Without refractory linings, steelmaking would not be possible.

Excellent heat resistance, make refractories have superior creep resistance. Nevertheless, refractories usually do experience creep at high temperatures under thermo-mechanical loads in service [24], due to restricted thermal expansion and high temperatures [27]. Creep can be a bottleneck in lining lifetime and cause premature failure of the refractory, leading to additional standstills and accompanying financial losses. Therefore, knowledge on creep behaviour is critical for furnace lining life predictions and selection of materials.

Little is known about the development at high pressures and temperatures, and the driving material characteristics behind creep behaviour [26]. This makes it difficult to predict creep resistance. Material characteristics such as porosity, density, chemical composition, binder type, particle size distribution and addition of antioxidants are known to influence creep behaviour [15]. In this thesis, the focus has been put on a two material characteristics, so that an in-depth evaluation could be done. The chosen characteristics are: the binder content and addition of anti-oxidants, in this case: aluminium. Some research has been done on the effect of different binder systems on the effective thermo-mechanical properties of refractories [1, 2, 3, 12, 17, 19, 28, 29, 35]. However, the effect of binder content on creep development for a magnesia carbon refractory remains to be investigated. In addition, the same can be said for altering the aluminium content in a magnesia carbon system.

Accurate creep test methods that simulate the operating environmental conditions to which magnesia-carbon refractory bricks are exposed, are paramount for assessing creep development. The experimental setup of creep measurements depends on the type of sample and load condition (compressive or tensile). International standardised creep tests (ISO3187:1989(EN)) are used for quality control, selection of materials and product definition. The benefit of using this method, is that it is internationally accepted and used by industries, contractors and refractory suppliers alike. The drawback is that the testing pressure is fixed at 0.2 MPa, which does not resemble pressures imposed in actual working conditions (e.g. 20 MPa for steel ladle wear linings [32]). Currently, a non-standardised set-up is designed at the Ceramic Research Centre (CRC) at Tata Steel IJmuiden, to be quicker and able to apply variable (higher) pressures. Pressures can be increased after a variable time-step at a constant temperature while measuring the creep. This method has proven promising but requires further validation against a static creep test.

The main objective of this thesis, is to investigate the influence of binder and aluminium content on creep development in magnesia-carbon refractories. In order to achieve this objective, the following sub-objectives are defined:

- To evaluate if a multi-stage creep test can shorten the creep testing campaign.
- To validate data from a multi-stage creep test against a static creep test.
- To quantify the effect of increasing binder content in an MgO-C refractory brick on creep development.
- To determine the contribution of spinel formation on the effective thermo-mechanical properties of the material.
- To quantify the effect of increasing aluminium content in an MgO-C refractory brick on creep development.

To meet these objectives, a literature study is performed first, which gives more insight in to the refractory system, creep analysis methods and creep behaviour of magnesia carbon refractories. Subsequently, different magnesia-carbon recipes are defined and pressed in to bricks, where binder and aluminium content is varied. Samples, resulting from the pressed bricks, are then used to characterise the material's microstructure and analyse its thermo-mechanical behaviour.

The report structure is as follows:

- Chapter 2 provides background information on steelmaking, refractory linings and creep behaviour of refractories.
- Chapter 3 describes the materials and methods used in this work.
- Chapter 4 gives an overview of the obtained results for the different experiments, along with discussions and explanations.
- Chapter 5 concludes this work and provides recommendations for further investigation

2

Theoretical Background

This chapter is dedicated to providing background information that will serve as the foundation of this thesis. First, the principles of basic oxygen steelmaking are discussed. The important role that refractories play here is highlighted. Thereafter, the main constituents of the refractory of interest (MgO-C) are highlighted with their advantageous properties. This information is critical for the reader to understand why the refractory system achieves certain thermo-mechanical properties. Finally, creep behaviour of refractories is discussed. More detail is given on how binder and aluminium content may influence creep.

2.1. Basic Oxygen Steelmaking

Basic oxygen steelmaking (BOS) is a method of primary steelmaking applied at Tata Steel IJmuiden. Molten metal (or: "pig iron") from the blast furnace is poured into an iron ladle. The material in the ladle is pre-treated to remove sulphur, silicon and phosphorus impurities. It is then poured in to the converter (schematically represented in [Figure 2.1](#)) where metal scrap is added as well. A water cooled lance then blows oxygen at supersonic speed in to the converter. As a result, the carbon content is reduced, and carbon dioxide and carbon monoxide are formed. Fluxes (e.g. lime) are added to remove impurities and minimise refractory wear. A slag forms at the top of the converter, which is removed after tapping of the molten metal. Liquid steel can then be transported to the direct sheet plant or continuous caster.

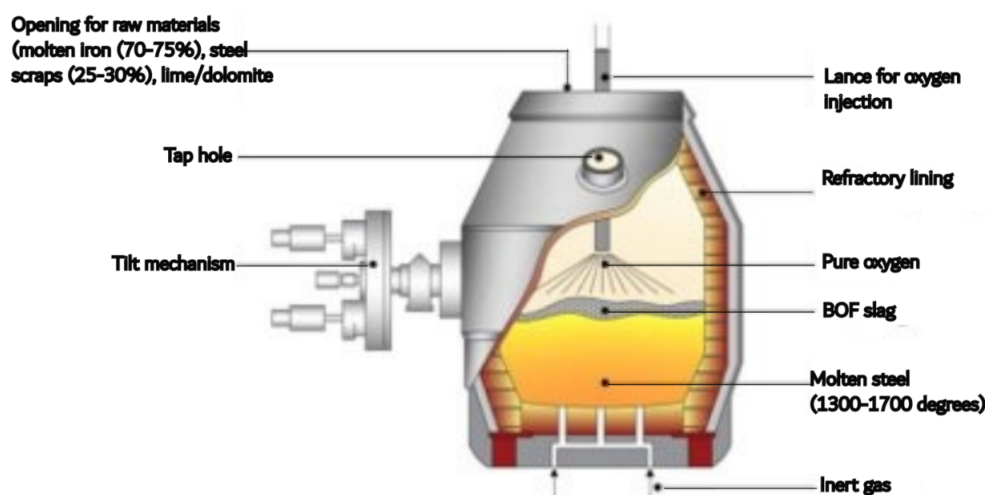


Figure 2.1: Schematic representation of the BOF [11].

2.2. Refractory linings

During BOS, temperatures inside the converter may be as high as 1600 °C [33]. These extreme conditions call for adequate protection of the converter. This is where refractories come in to play.

Magnesia-carbon (MgO-C) is a type of refractory material used during primary and secondary steel-making. These bricks are referred to as "MC bricks". Different types of MC bricks are used as lining materials. The MC brick composition is chosen based on its location. For example, the bricks at the top of the converter should have some mechanical resistance against the scrap that is charged into the furnace. For MC bricks at the bottom of the converter, this is less relevant. This composite type of unfired refractory is bound together by an organic binder, usually pitch or resin, which allows for a uniform distribution of carbon and magnesia [15]. Some of the main properties of this refractory are [15, 25]:

- High refractoriness due to utilisation of magnesia and absence of low melting phases.
- Slag penetration and spalling of material is reduced by graphite, due to its high thermal conductivity and low thermal expansion coefficient.
- High effective thermal conductivity.
- As a result of a high effective thermal conductivity, and low effective thermal expansion, the thermal shock resistance of the refractory is high.
- High corrosion resistance against slag due to hydrophobic character of graphite.

The different components of the MgO-C refractory system are:

- **Magnesia**, which is the main component of the refractory brick. It comprises of 80-90 wt% of the total material and mainly attributes to the high refractoriness and corrosion resistance [15].
- **Carbon (graphite)**. Better resistance against chemical attack imposed on the refractory grains, is inhibited by the non-wetting hydrophobic character of graphite [2]. Furthermore, graphite increases the thermal conductivity of the material, and subsequently the thermal shock resistance as well [15].
- **An organic binder** such as phenolic resin (Novolac). This component will mainly serve as an adhesive and additional source of carbon.
- **Antioxidants** such as metallic aluminium. Carbon oxidation is retarded due to the addition of antioxidants. Addition of aluminium to the MgO-C brick leads to a numerous amount of side-reactions taking place at 1200 to 1500 °C [15]. The addition leads to formation of Al_4C_3 , AlN , Al_2O_3 and magnesium aluminate (MA) spinel [25].

2.3. Creep behaviour of refractories

Refractories are known to have superior creep resistance. Nevertheless, refractories usually do experience creep at high temperatures under thermo-mechanical loads in service [24], due to restricted thermal expansion and high temperatures [27].

Creep response can be divided in to three stages. These are described by Jin, Harmuth, and Gruber [13] as the primary, secondary and tertiary stage. During the primary stage, strain hardening is the dominant process, as resistance to dislocation movement is increased. Hence, this part of the creep curve has a negative slope ($\dot{\epsilon}_{cr} < 0$), as can be seen in Figure 2.2. In the secondary stage, a balance between strain hardening and softening is reached. During this steady state, the creep curve has a constant slope ($\dot{\epsilon}_{cr} = 0$). In the tertiary stage, this balance is disturbed by localised necking, micro-void formation, intergranular cracking and precipitation of brittle particles. This part of the creep curve is characterised by an increasing strain rate ($\dot{\epsilon}_{cr} > 0$), which will ultimately lead to sample rupture.

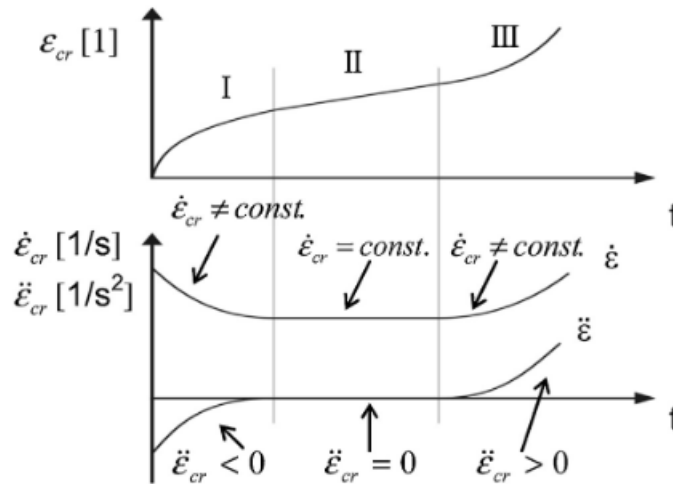


Figure 2.2: Three stages of creep with creep strain (ϵ_{cr}), strain rate ($\dot{\epsilon}_{cr}$) and acceleration of strain rate ($\ddot{\epsilon}_{cr}$) [13].

Refractory materials are complex due to their heterogeneity. Their microstructure, which can be multi-phased, has a wide spread of grain sizes. Moreover, their matrix is composed of bonded fines and defects (cracks and pores) [24]. Due to this complexity, assessing the contributions of different creep mechanisms (e.g. slipping across the grain boundaries, diffusional creep) is difficult [30].

Refractory materials can be shaped into bricks. Here, creep can be related to thermal stresses that originate on a microstructural level and on a brick/lining level [10]. On a microstructural level, thermal stresses originate due to restriction of thermal expansion/shrinkage between the different parts of the refractory brick. Different Coefficients of Thermal Expansion (CTE) are related to these thermal stresses. This CTE mismatch has an impact on the fracture behaviour of the refractory brick. It is therefore an important design parameter.

On the brick/lining level, thermal stresses can form due to a temperature gradient within the brick. These stresses are induced from the hot face to the cold face. The temperature gradient causes the brick to expand, and as a result a stress gradient forms within the brick. Compressive stresses form near the hot face (where expansion is restricted by the cooler part of the material) and tensile stresses form away from the hot face [10]. External mechanical constraints play a role in the formation of thermal stresses as well. When placed in a cylindrical structure, the surrounding bricks impose an external constraint. As a result, the bricks have insufficient space to expand, possibly leading to creep or failure of the brick due to formation of compressive strains [10].

Creep behaviour in refractories can be described using different types of models. Examples are: the θ projection concept [18, 26], the rheological [5] and Norton Bailey models [26]. Besides determining which creep model is appropriate, testing parameters such as applied load and temperature play an important role in studying creep behaviour. The experimental set-up of creep measurements and modelling of creep behaviour will be further elaborated on in [Section 3.2](#).

2.3.1. Effect of binder content on creep

Binder systems are added to refractories to serve as a bonding agent. On one hand, binders such as coal-tar pitch and phenolic thermosetting resins help to increase the thermal conductivity. On the other hand, they reduce the Young's modulus, thermal expansion coefficient and wettability by molten metals and slags [17]. Moreover, the presence of a glassy phase with a low melting point, highly affects the thermo-mechanical behaviour of refractories [35]. Low wettability allows the glassy phase to partially penetrate grain boundaries, causing weakening of the bonds between the grains. A high concentration of the glassy phase and other low melting phases, may form a continuous network should grain boundaries be destructed under elevated temperatures and loads [35].

The creep behaviour of refractory materials is influenced by the following binder parameters:

- **Concentration.** A high concentration of the glassy phase, and other phases with a low melting point, leads to an increase in creep sensitivity due to weakening of bonds on grain boundaries [35].
- **Degree of localisation of the glassy phase.** The localisation of the glassy phase relates to the distribution of this phase in the matrix, between the grains. In the case of resin bonded materials, the ordering of the glassy phase is a factor that improves mechanical parameters. [19]
- **Structure and density of the binder.** If the structure and density of the binder are elevated, the effective viscosity of the material will increase, and as a result the creep resistance will increase. [36]
- **Adhesive strength.** The adhesive strength relates to the wettability of the binder. If the level of wettability is low, the glassy phase may be able to penetrate in the grain boundaries. This causes weakening of the bonds between grains, and thus an increase in creep deformation due to easier sliding. [35]

Impurities within the raw materials may influence the creep behaviour as well. Lime (CaO) and silica (SiO₂) may be present within the samples. Creep resistance, may be influenced by these impurities [26, 31]. Secondary phases that are able to form due to a low CaO/SiO₂ (C/S) ratio, decrease the creep resistance.

2.3.2. Effect of aluminium content on creep

The addition of aluminium leads to formation of Al₄C₃, AlN, Al₂O₃ and MA spinel [25]. Spinel structures, with a general formula of AB₂O₄, form a group of oxides. MA spinel has a high melting point ($T_M = 2135$ °C), a low density (3.58 g/cm³) and low thermal conductivity (5 W/mK) [4]. A formation mechanism of spinel from alumina and magnesia is related to counter-diffusion of the Al³⁺ and Mg²⁺ cations (seen in Figure 2.3).

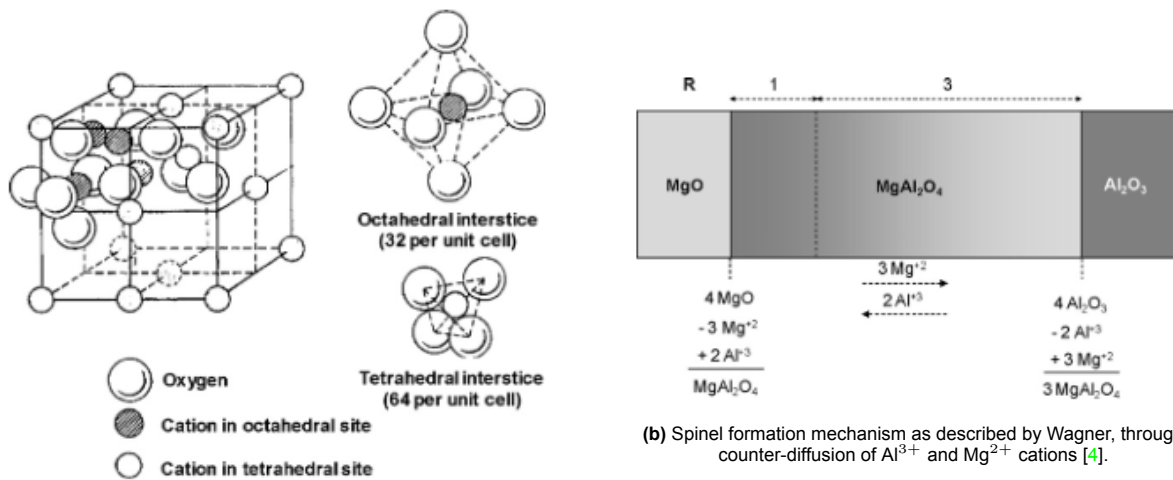


Figure 2.3: Crystal structure and formation mechanism of Magnesium Aluminate spinel.

Physical and thermal properties of the reactants (MgO and Al₂O₃) and spinel are shown in Table 2.1. When MA spinel is formed, it is paired with an irreversible volume expansion within the refractory due to differences in density between the reactants and MA spinel. Their differences in thermal expansion are in part responsible for the superior thermal shock resistance of spinel [22]. On one hand, an increase in volume is advantageous. It enables pore filling and joint closure, and thus the porosity is decreased. On the other hand, an excess of volume expansion will increase the stress state within the refractory brick. As a result, cracking may occur [9].

	MgAl ₂ O ₄	MgO	Al ₂ O ₃
Density (g/cm ³)	3.58	3.65	3.99
Thermal Conductivity (W/mK)	5	7	7
Thermal Expansion Coefficient ($\cdot 10^{-6}/^{\circ}\text{C}$)	8.4	13-15	8.7-9.3

Table 2.1: Thermal and Physical properties of MgAl₂O₄, MgO and Al₂O₃ at 1000 °C [14, 6].

Research has been done on the thermo-mechanical behaviour of spinel [24, 34, 30, 4, 18]. Certain features are discussed such as phase transformation, thermal expansion behaviour, refractoriness under load and flexural strength (hot modulus of rupture, HMOR). Ghosh et al. [9] found a trend of increasing HMOR with increasing spinel content, until 20 wt% is reached. Beyond this value the flexural strength decreases. It is hypothesised by the authors that this is due to tensile hoop stresses forming around the spinel grains. However, it is observed that for a spinel content of 30 wt% cracks propagate due to a higher extent of micro cracking, and hence the strength deteriorates. This result shows that spinel content is an important parameter for the thermo-mechanical properties of a spinel-containing refractory brick.

Another feature that can be formed due to aluminium additions, is whiskers. Routbort et al. [23] hypothesised that whisker formation can improve creep resistance, as they are able to pin grain boundaries and hence prevent grain boundary sliding in low stress regions. Nevertheless, damage can be promoted due to whiskers in high stress regions. Routbort et al. [23] stated that oxidation of SiC whiskers and the presence of a glass phase can be detrimental to creep resistance. Furthermore, assessing the presence of whiskers in a material is difficult due to their needle-shaped appearance. Confirming their presence via microscopy and determining their chemical composition, are therefore vital when studying the thermo-mechanical behaviour of such a refractory brick.

3

Materials and Methods

In this chapter, the materials and methods used during this thesis are described. Experiments were conducted on five different recipes, where binder wt% and aluminium wt% were altered. These recipes will be studied throughout this thesis to highlight the effect of altering binder- and aluminium content on microstructural and mechanical properties, all with a focus towards creep behaviour. The raw materials and their weight percentages of each recipe, are specified in [Section 3.1](#). Bricks were pressed for each recipe, from which samples were drilled for certain experiments. The processing step of making the bricks is described in [Appendix A](#). The recipes can be found in [Appendix B](#). In [Section 3.2](#), the methodology of all experiments that were conducted during this thesis is described. Emphasis is put on the creep testing in [Section 3.2.3](#), as this is the main focus of this research. Other experiments are conducted to give insight in material properties and/or to understand certain creep behaviour.

3.1. Materials

Experimental work was conducted on samples originating from bricks that were pressed at the CRC at Tata Steel IJmuiden. Five different recipes were defined, where binder wt% and aluminium wt% were altered. The recipes formulated were comprised of the same base composition: 12 wt% C (graphite, 92N, Skaland graphite) and 88 wt% MgO (magnesia, FM 97.8, YAS). The raw materials and their type or fraction are stated in [Table 3.1](#).

Raw materials	Type or fraction	wt. %
Graphite	92N	12.0
Magnesia	0-0.25 mm	23.8
	0.25-1 mm	22.1
	1-2 mm	22.1
	2-4 mm	20.0

Table 3.1: Raw materials used for all recipes.

The recipes were named according to their composition. Here, the term 'PMC' (referring to a magnesia-carbon refractory) is followed by binder wt% and aluminium wt%. Novolac resin (Bakelite 8505F) was used as the binder material. The binder requires a hardener, which allows it to set properly upon fabricating the refractory brick. In this study, hexamethylenetetramine was used as a hardener. Its content is a function of the wt% of added binder. Metallic aluminium (G341, powder) was added to the final two recipes.

Raw materials [wt.%]	PMC-2% binder	PMC-3% binder	PMC-4% binder	PMC-3% binder -1% Al	PMC- 3% binder -3% Al
Metallic aluminium	0.0	0.0	0.0	1.0	3.0
Hexamethylenetetramine	0.2	0.3	0.4	0.3	0.3
Novolac resin	2.0	3.0	4.0	3.0	3.0

Table 3.2: Additives of each refractory brick.

3.2. Methods

Section 3.2 is divided into two subsections. Section 3.2.1 describes the experiments that were performed to characterise the microstructure and phase distributions. The former is done by performing microscopy and SEM (Scanning Electron Microscopy) analyses, the latter via X-Ray Diffraction (XRD). Section 3.2.2 describes the experiments that were conducted to characterise the mechanical behaviour. These will give a first understanding on how the materials (thermo-)mechanical properties are defined, and how these may be related to its creep behaviour.

3.2.1. Microstructural characterisation

The aim of these experiments are to visualise and describe the microstructure and gain understanding about microstructural processes occurring inside the material (i.e. cracking, pore formation, sintering etc). XRD (X-Ray Diffraction) analyses were performed to determine phase distributions in the sample. XRD measurements were conducted at room temperature and with increasing temperature. The main aim was to determine which secondary phases form at which temperatures. These secondary phases may influence creep resistance or other (thermo-)mechanical properties.

A Zeiss AxioImager Z1 automated **microscope** was used to perform microstructural characterisations of the samples. Images were taken using reflected polarised light and magnifications between 50 and 200 times.

The microstructure can also be visualised via a **Scanning Electron Microscope (SEM)**. Samples were carbon coated prior to analysis. Images were taken on the JEOL JSM-7001-F SEM. Oxford Aztec 6.0 software was used to visualise the microstructure and quantify mineral wt% using EDS (Energy Dispersive Spectroscopy). EDS analyses lasted 20s.

In addition, **X-Ray Diffraction** analyses were performed. Samples were first fired at 110 °C, and were then cooled before conducting the XRD measurement. Phase proportions of samples were determined by XRD and subsequent Rietveld analysis. The XRD patterns were recorded in the range of 10 to 130° (2 θ) in reflection mode using a fully automated Bruker D8 Endeavour diffractometer (CoK α -radiation) equipped with a position sensitive detector. The step size was n.d. 0.02°, time per step was 200 s. Quantitative determination was performed to determine phase proportions, by Rietveld analysis. The refinement was done on the assumption of pure phases. Unit cell parameters, background coefficients, preferred orientations, profile parameters and phase proportions were refined using the TOPAS software package for Rietveld refinement.

A PANalytical X'Pert Pro XRD (with CuK α -radiation) was used to perform XRD measurements at elevated temperatures. The XRD patterns were recorded in the range of 30 to 100° (2 θ) in reflection mode. An inert environment is created by using nitrogen gas. Temperature is increased at a rate of 2 °C/min, where measurements were performed every 40 °C. Eurotherm tools is used to monitor the temperature, and X'Pert Pro DataCollector is used to set-up the XRD measurement.

3.2.2. Mechanical characterisation

Section 3.2.2 describes the experiments that were conducted to characterise the mechanical behaviour. The results of these experiments can be used to explain creep behaviour. Furthermore, intrinsic material properties can be determined which can be related to the usefulness for the real-life application.

Permanent linear change (PLC)

The PLC is a measure that indicates the expansion of the refractory brick after being subjected to a specified temperature for a specified time. Once the sample was cooled down, the bulk density ρ_b and apparent porosity π_a were determined during the PLC measurement. Samples used for experimenting are 50 mm in diameter and 60 mm in height. At the CRC at Tata Steel, the ISO 2478:1987 standard is used for measuring the PLC. Measurements were conducted to determine the densities and porosities before and after heat treatment. In addition, the expansive behaviour can be analysed via this experiment, and linked to its real-life application and other deformation experiments.

Cold crushing strength (CCS)

The Cold Crushing Strength test (CCS) provides information about the compressive strength of the material at room temperature. A first impression of the material's cold compressive strength will result from a CCS measurement. The CCS is the ratio between maximum force and cross-sectional area.

$$CCS = \frac{F_{max}}{A_0} \quad (3.1)$$

Where F_{max} is the force on the sample at the moment of breakage or pulverisation (in Newton), and A_0 is the cross-sectional area (mm^2). Measuring of the CCS for dense materials at the CRC at Tata Steel IJmuiden is measured according to the ISO 10059-1 standard.

Hot modulus of rupture (HMOR)

The HMOR (i.e. flexural strength) indicates the maximum load at high temperatures at which a rectangular test piece breaks when loaded according to a three-point bending. The dimensions of this test piece are 150 mm x 25 mm x 25 mm. As mentioned, the measurement at the CRC at Tata Steel is based on a three-point bending test, according to the ISO 5014 standard. HMOR testing was performed at the same temperature as the PLCs (1400 and 1500 °C). The resulting porosities, densities and expansive behaviour from the PLC measurements may be linked to the HMOR results.

Dilatometry

Dilatometry was performed to measure dimensional changes whilst subjected to increasing/decreasing temperature. This may be linked to phase transformations. In addition, the Coefficient of Thermal Expansion (CTE) was determined from the dilatometry measurements. During measuring, the change in sample dimensions was tracked, whilst heating up to a predefined maximum temperature. Heating up of the sample was done with a rate of 2 °C/min. At the CRC at Tata Steel IJmuiden, the NEN-EN 933-19 standard is used for performing dilatometry measurements. It should be noted that according to the standard, dilatometry measurements should be performed pressure-less. However, at the CRC at Tata Steel IJmuiden, a pressure of 0.02 MPa is applied on the sample during testing.

The CTE can be determined in a certain temperature range from the dilatometry curves. This was done using the following equation:

$$CTE = \frac{1}{L} \frac{dL}{dT} \quad (3.2)$$

Where L is the original sample length, dL the change in length and dT the change in temperature.

Refractoriness under load (RuL)

Refractoriness under load is a measure of the behaviour of a refractory material subjected to the combined effects of load, rising temperature and time. During testing, the test piece was subjected to a fixed load of 0.2 MPa whilst heating up. In this thesis, samples were heated to the test temperature (1600 °C). This was the maximum temperature the device could reach. Samples were kept at 1600 °C for a few hours. The samples that were used have a diameter and height of 50 mm. An output of the measurement is linear deformation per rising temperature. From the measurement, ' T_0 ' could be retrieved. This is the temperature where the maximum amount of positive deformation occurs within the desired temperature range. Following from T_0 are the temperatures at which an additional 0.5%, 1.0% and 2.0% negative deformation occurs. These temperatures are defined as $T_{0.5}$, T_1 and T_2 . The RuL determination at the CRC at Tata Steel IJmuiden is measured according to the NEN-EN-993-8 standard. In this study, the RuL results will be used to determine if the refractoriness of the samples is adequate enough for real-life operating conditions.

Hot compressive strength

During hot compressive strength testing, a sample of 30 mm diameter and 50 mm height was used for testing. Pistons moving at a constant speed compress the sample, after the sample was heated to a desired test temperature. The force that the sample exerts on the pistons was measured. An output of this technique is a force-displacement curve, which can be translated to a stress-strain curve. The latter can be used to determine the yield stress, Young's modulus and the Ultimate Compressive Strength (UCS). The UCS can be used when experiments, such as creep testing, require measuring at higher loads. The UCS is then used as a design parameter to ensure that the sample does not fail during the experiment. At the CRC at Tata Steel IJmuiden, the hot compressive strength measurement is done on a ZwickZ250 apparatus according to the ISO 22685 standard, using TestXpert II to process the experimental data.

3.2.3. Creep testing

Measurement technique

To improve simulations of creep behaviour, instead of using the standardised creep test (ISO3187:1989(EN)), loads are increased step-wise during testing at a specific temperature. The setup of the creep testing rig (Zwickstron 8561) is shown in [Figure 3.1](#). Arrows indicate the heating elements that were used to heat up the sample. The sample was placed with the required oxidation protection, between the upper and lower piston. A schematic representation of the sample setup is shown in [Figure 3.2](#). Cylindrical samples of 30 mm diameter and 50 mm height were prepared for the experiments. To prevent oxidation of the material during experimenting, samples were placed in an reducing environment. As seen in [Figure 3.2](#), oxidation protection is achieved via graphite rings surrounding the sample, and pet coke particles scattered on top of the sample.

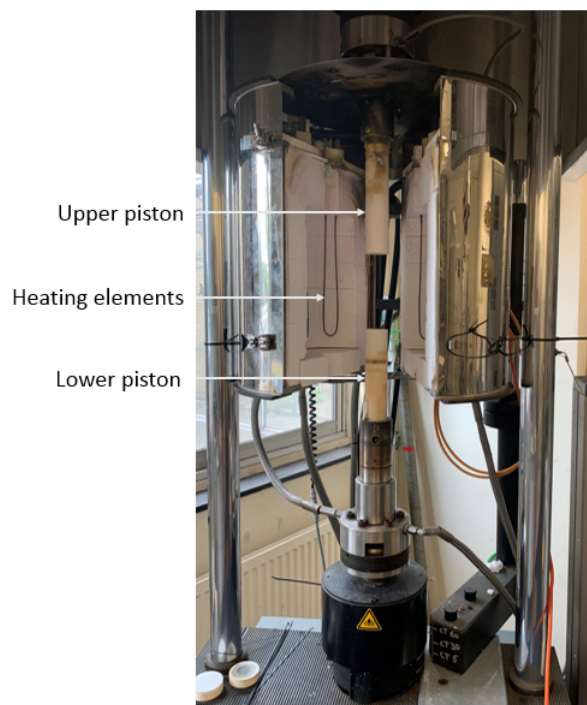


Figure 3.1: Experimental setup of the compressive creep testing rig at the CRC at Tata Steel IJmuiden.

A graphical representation of the multi-stage creep test program is shown in [Figure 3.3](#). Once the sample was placed inside the apparatus, the setup heats up to the desired test temperature in 5 hours. Whilst heating up, a preload of 0.5 or 1 MPa was applied in order to fix the sample properly. Homogenisation of the temperature in the sample was achieved by a dwell time of 5 hours after reaching the test temperature. Subsequently, the material was loaded in 5 consecutive stages. Each stage lasted 5 hours and load was increased by 2 MPa for each stage.

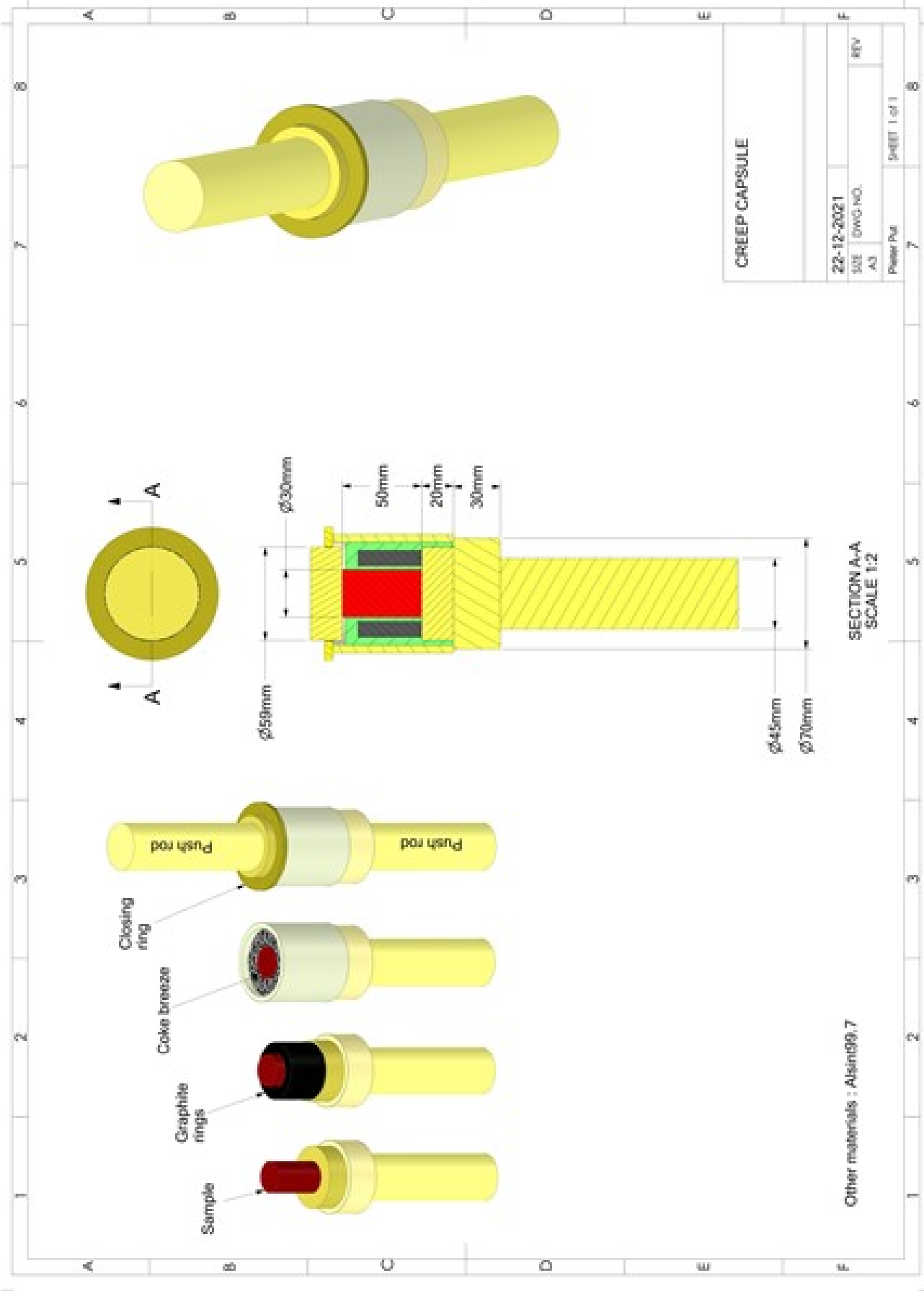


Figure 3.2: Schematic representation of sample set up. Sample is protected by graphite rings, pet coke, a TFF 180 alumina ring and Alisint alumina disks.

To validate data from the multi-stage creep experiment, a single stage measurement was performed. Here, a constant load and temperature were applied on the sample. Resulting creep rates will then be compared to show over- or underestimation of the multi stage experiment.

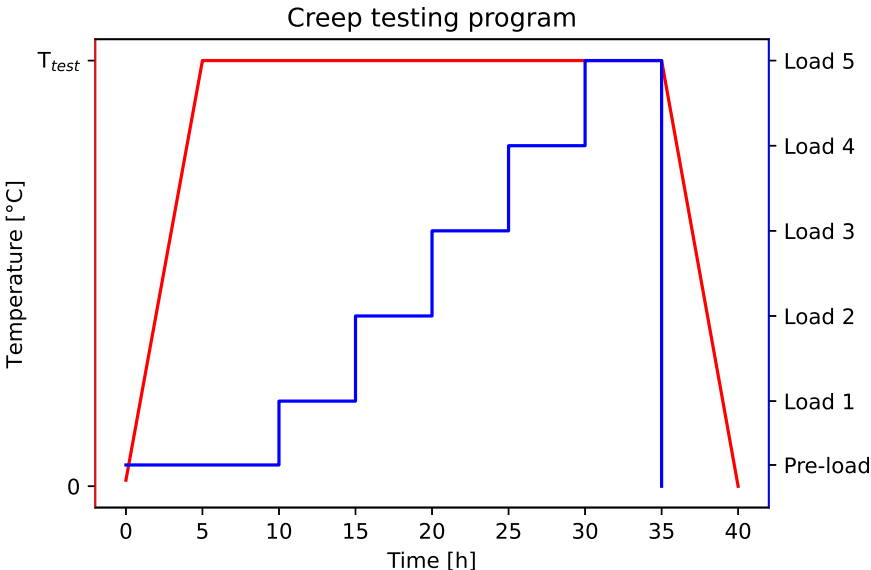


Figure 3.3: Schematic representation of multi stage creep measurement.

Data processing

Experimental data is processed in TextXpert II. During the experiment, the displacement of the lower piston is measured over time. The displacement (d), together with the original sample length (L), can be used to determine the total experimental strain. Displacement and sample length are related via:

$$\varepsilon_{tot} = \frac{d}{L} \tag{3.3}$$

The total strain (ε_{tot}) can also be represented as a sum of plastic (ε_{pl}) and elastic strains (ε_{el}). It is important to exclude elasto-plastic strains from the data, as the objective is to only include secondary creep strains (ε_{cr}) in the creep model. A schematic representation of an experimental stress-strain curve is shown in Figure 3.4. The black curve follows a regular loading-unloading regime, where plastic strains (ε_{pl}) and elastic strains (ε_{el}) are shown. However, in this study, during creep testing the load is kept constant for 5 hours, and subsequently increased. This is shown by the blue curve, where the load is kept constant at σ_1 , and subsequently increased to σ_2 . By definition, during creep, applying a constant load for a longer periods of time at high temperatures, will cause for formation of creep strains (ε_{cr}). The different strain components that will arise from creep testing are shown in blue in Figure 3.4.

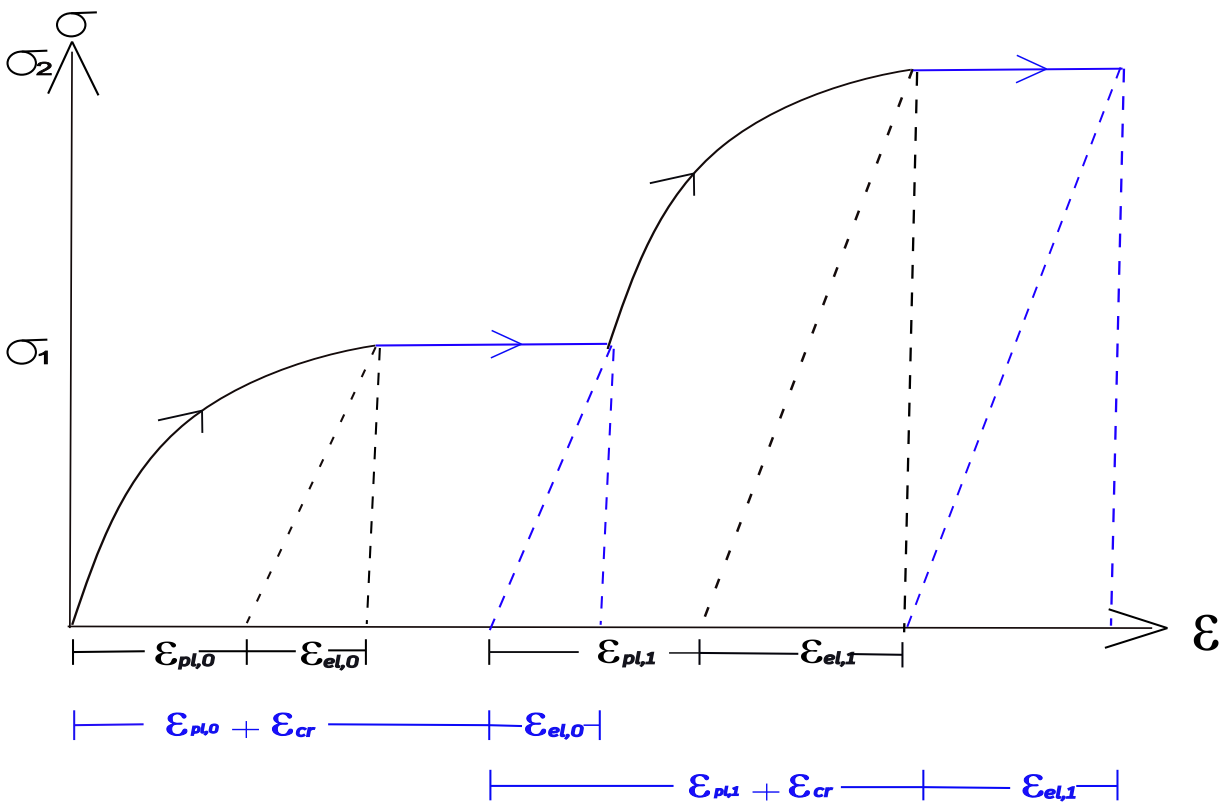


Figure 3.4: Schematic stress-strain curve. Black curve indicates regular loading-unloading curve. Blue curve shows results for a creep test. Dotted lines indicate unloading path.

After creep testing, the total experimental strain (ε_{tot}) data can be visualised in a strain vs time plot, as is done in Figure 3.5. Note that these strains contain all components: $\varepsilon_{el} + \varepsilon_{pl} + \varepsilon_{cr}$.

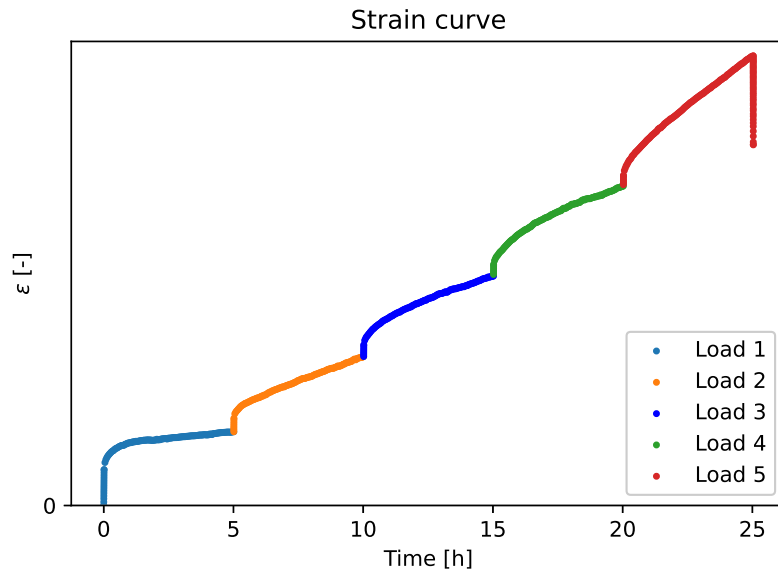


Figure 3.5: Example of a schematic strain curve.

Once the total strain is known, the experimental strain rate can be determined by dividing the change in total strain by the change in time:

$$\dot{\epsilon} = \frac{\Delta\epsilon}{\Delta t} \quad (3.4)$$

Experimental strain rates resulting from Equation 3.4 can then be visualised. An example of this is shown in Figure 3.6.

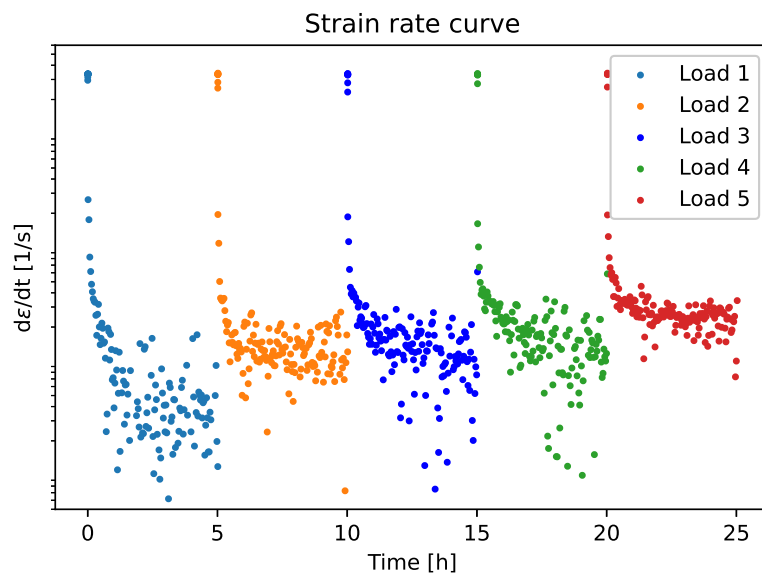


Figure 3.6: Example of a schematic strain rate curve.

The creep model, which will be discussed in the next section, requires the following:

1. Experimental creep rates which do not contain $\dot{\epsilon}_{el}$ and $\dot{\epsilon}_{pl}$, but only $\dot{\epsilon}_{cr}$.
2. For the experimental creep rates to be in the secondary stage. This is where the slope of the strain rate curve is constant, and thus follows a horizontal trend.

3. Experimental creep rates must result from applied loads that are <50% of that materials ultimate compressive strength (UCS). This criteria is in place to ensure that the material is not in a "critical" state when testing, i.e. close to failure.

Requirement 1 and 2 are met by determining the average creep strain rate over the last two hours of a load regime. This part of the curve (as seen in [Figure 3.6](#)) has a constant slope and hence only contains secondary experimental creep strain rates $\dot{\epsilon}_{cr}$. Therefore, if an experiment was successful, five average experimental creep strain rates can be determined from a single measurement. These values can then be inserted in to the creep model.

3.2.4. Creep modeling

Different creep models, for instance the Norton Bailey model, may be applied to evaluate experimental creep data. This model can be used to define all three creep stages. According to its strain hardening/softening formulation, it includes a stress, temperature and creep strain dependency on the creep rate. Implementation of this model is often found in finite element programs. The Norton-Bailey equation in its strain hardening/softening form is formulated as [\[26\]](#):

$$\dot{\epsilon}_{cr,j} = K(T) \cdot \sigma^{n_j} \cdot \epsilon_{cr}^{a_j} \quad (3.5)$$

In [Equation 3.5](#), $\dot{\epsilon}_{cr}$ denotes the creep strain rate, parameter $K(T)$ is a temperature function, σ^n defines the stress with stress exponent n , and ϵ_{cr}^a is the creep strain. The exponent a is negative if primary creep is occurring (strain hardening), zero for secondary creep (balance between hardening and softening) and a is positive for tertiary creep (strain softening). The subscript j denotes the creep stage ($j = 1,2,3$) [\[26\]](#).

In this research, a version of the Norton Bailey equation was used to evaluate the experimental data. This equation, governing steady state creep, can be formulated as:

$$\epsilon_{II} = f_1(\sigma) \cdot f_2(t) \cdot f_3(T) \quad (3.6)$$

Where:

$$\begin{aligned} f_1(\sigma) &= C_1 \cdot \sigma^{C_2} \text{(Norton)} \\ f_2(t) &= t \text{(Secondary creep)} \\ f_3(T) &= e^{-(Q_{act}/RT)} \text{(Arrhenius)} \end{aligned} \quad (3.7)$$

Combining the equations above, results in the Norton-Bailey secondary creep strain equation. This takes the following form:

$$\dot{\epsilon}_{II} = A \cdot \sigma^n \cdot e^{-(Q_{act}/RT)} \quad (3.8)$$

$$\dot{\epsilon}_{II} = C_1 \cdot \sigma^{C_2} \cdot e^{-(C_3/T)} \quad \text{where } C_1 = A, C_2 = n, C_3 = \frac{Q_{act}}{R} \quad (3.9)$$

In [Equation 3.8](#), A is a material constant, σ^n defines the stress with stress exponent n and $\exp(-\frac{Q_{act}}{RT})$ is derived from the Arrhenius equation [\[26\]](#), where Q_{act} represents the activation energy.

The model, using [Equation 3.9](#), is fed with experimental creep rates, temperatures and pressures. Inversely estimated creep rates and the corresponding creep parameters (C_1 , C_2 and C_3) are then determined. The sum of the squared differences between the resulting experimental creep strain data and estimated data is minimised.

A flow diagram which summarises all steps taken during creep testing (experimental, data processing and modelling) is shown in [Figure 3.7](#)

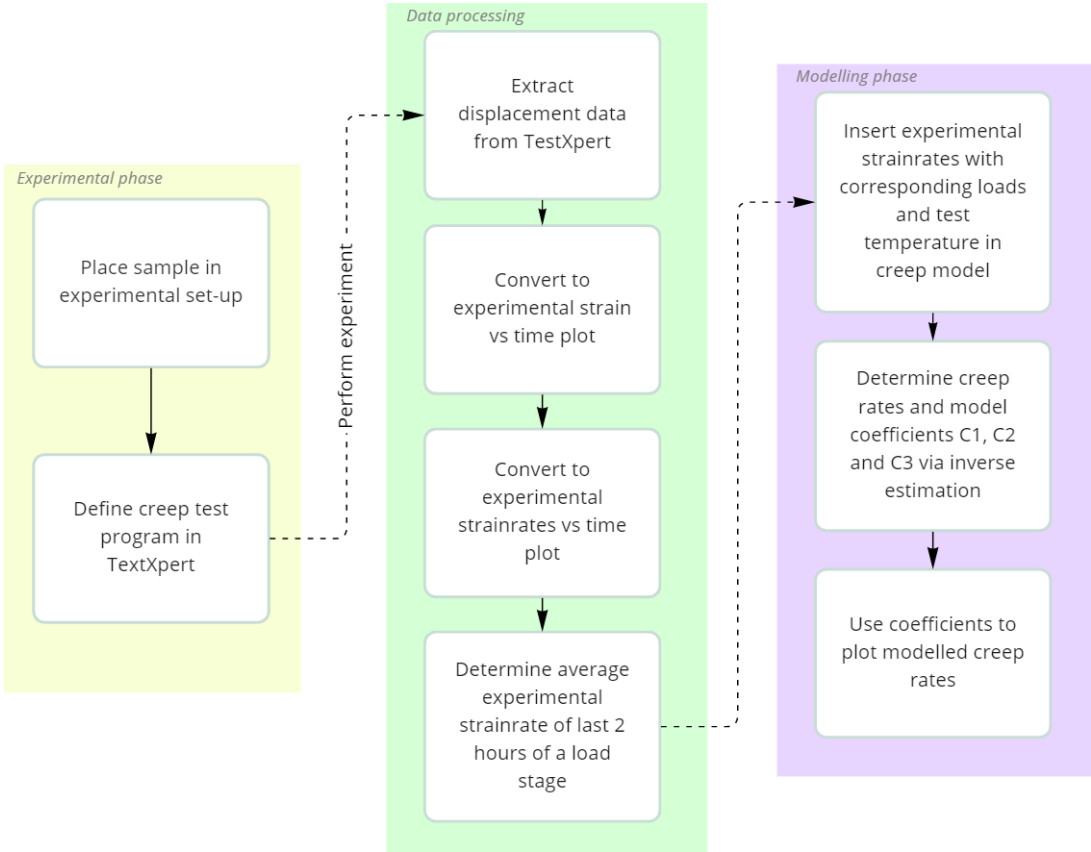


Figure 3.7: Flow chart of the creep testing methodology

4

Results and Discussion

This chapter is divided into two sections. The first describes the microstructural characterisation. Here, microscopy, SEM and XRD findings are presented and interpreted. Thereafter, the second section describes the (thermo-)mechanical characterisation of the tested recipes. The PLC, CCS, HMOR, dilatometry, RuL, HCS results are shown. These may be used to understand the influence of spinel on thermo-mechanical properties. More importantly, these results can be drawn on when interpreting certain creep behaviour.

4.1. Microstructural characterisation

A visual representation of the material is shown in [Figure 4.1](#). Note that a green sample of the PMC-3%-binder recipe was used here. Three main features may be recognised: the MgO grains, the graphite and binder. The MgO grains show up as grey features, and the graphite and binder surround the grains.

[Figure 4.1](#) shows inhomogeneous grain size distribution, which is to be expected based on the weight fractions of the added materials, as described in [Appendix B](#). The shape of the magnesia grains can be described as angular. A few pores are present in [Figure 4.1](#), indicated by the black spots. Other defects such as (micro-)cracks are found within the magnesia grains. In [Figure 4.1](#), impurities that formed on the magnesia grains are indicated as well. Microscopy images were taken on green and fired samples for each recipe. These images can be found in [Appendix C](#).

Magnesia, due to its high CTE ($13-15 \cdot 10^{-6}/^{\circ}\text{C}$ [4]) will most likely expand into a semi-continuous network of magnesia grains at high temperatures. This conglomeration of grains may be described as an 'MgO skeleton'. It is expected that this will be the most profound for the PMC-2% binder recipe. The magnesia grains can move more freely due to less binder serving as an adhesive. This expansion will be accompanied by pore closure. Due to the volume expansion of the MgO grains, the stress state within the material is increased. As a result, microcracking may occur. A visual representation of the MgO skeleton can be seen when observing the microscopy image in [Figure 4.2](#). It can be seen that the MgO grains have expanded, and grainboundaries are touching continuously throughout this cross section. The MgO skeleton is less profound in [Figure 4.3](#). This is expected, as this sample had a binder content of 4%.

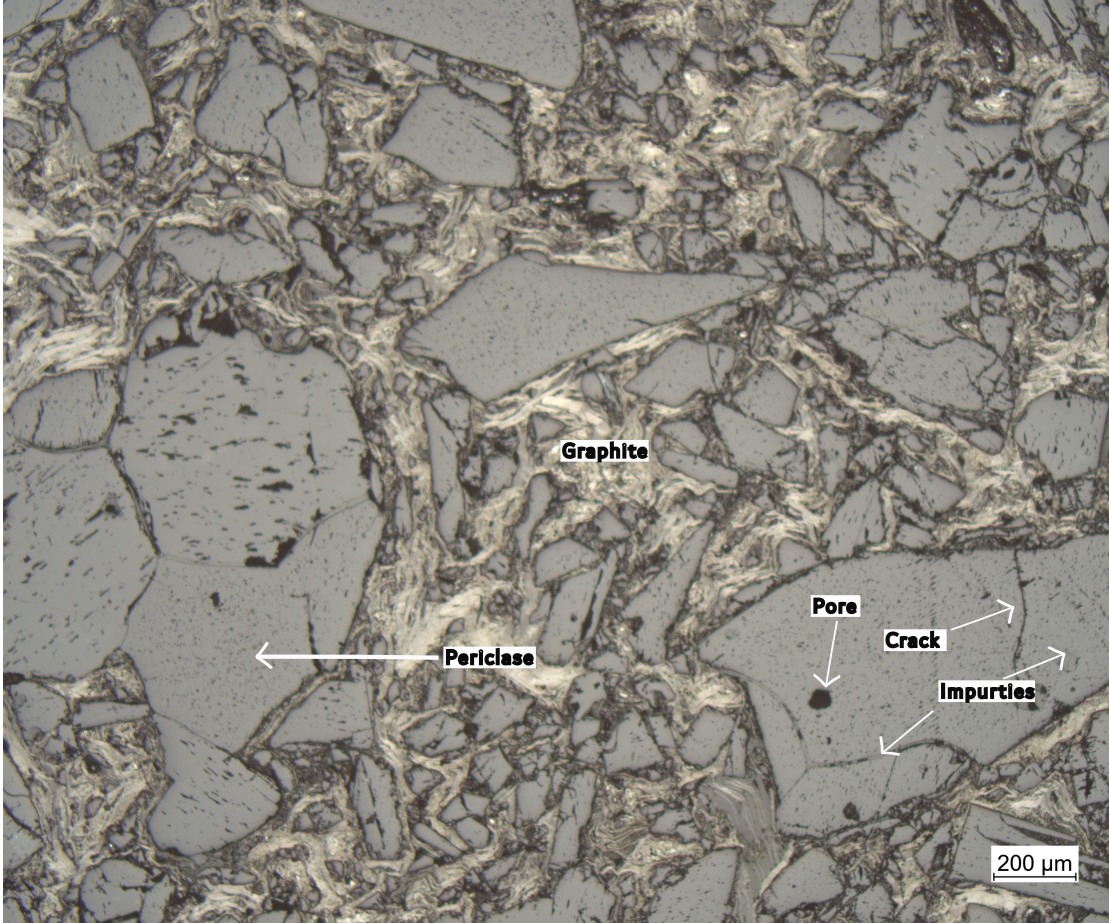


Figure 4.1: Microscopy image of a green PMC-3% binder sample. Microscopy image shows top-view of a cylindrical sample

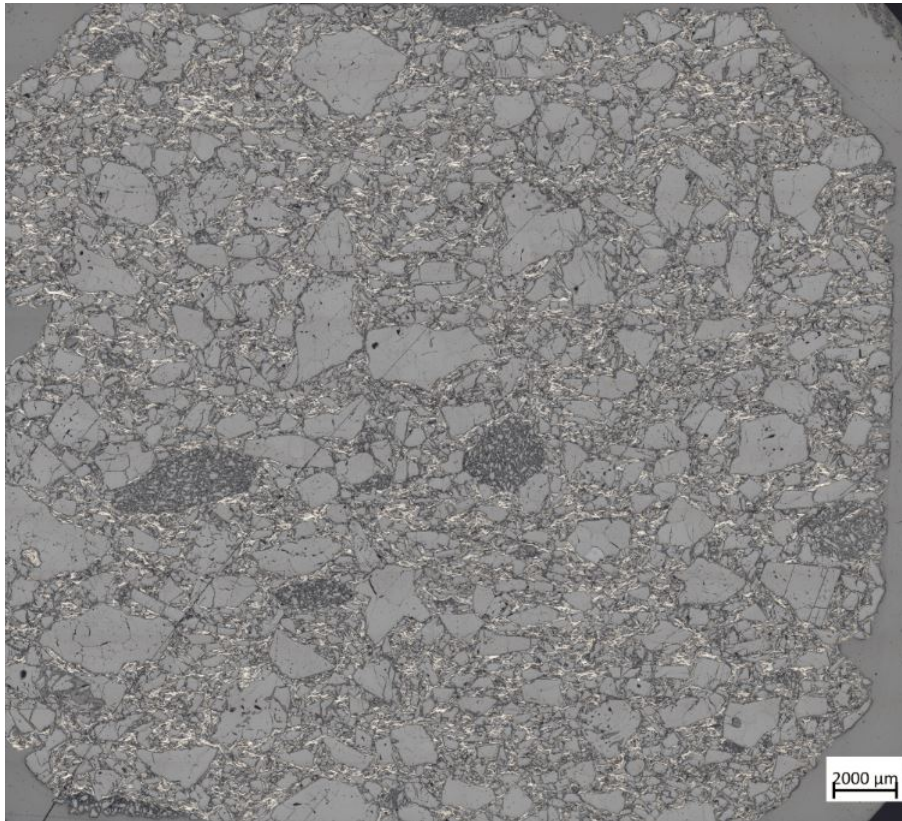


Figure 4.2: Microscopy image of a PMC-2% binder sample, fired at 1350 °C. Microscopy image shows lengthwise cross section of a cylindrical creep sample.

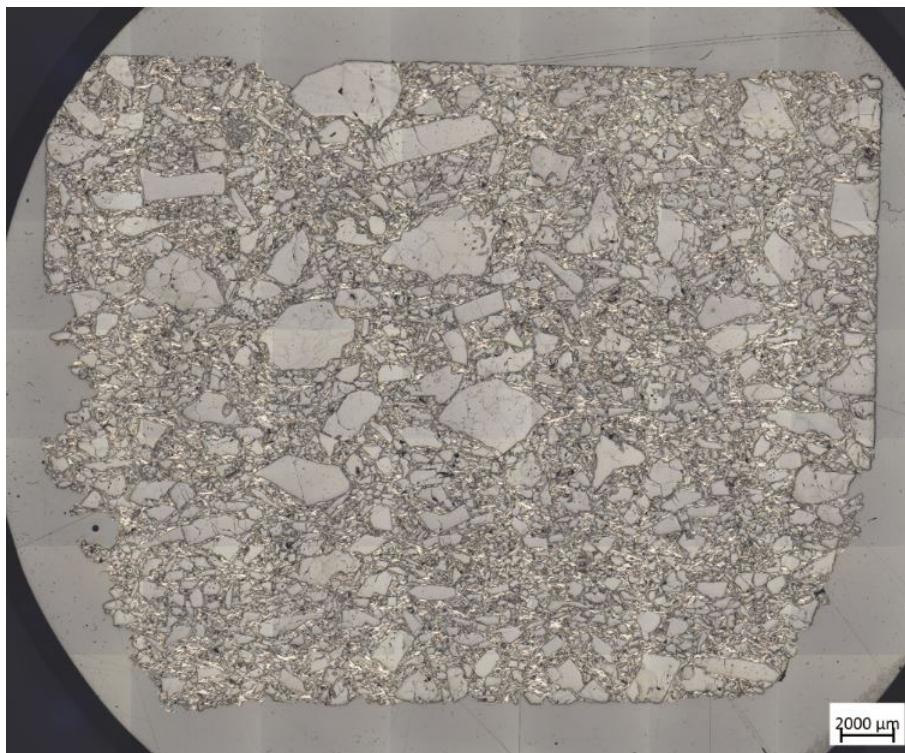


Figure 4.3: Microscopy image of a PMC-4% binder sample, fired at 1350 °C. Microscopy image shows lengthwise cross section of a cylindrical creep sample.

A green PMC-3% binder-1% Al sample was placed in the SEM, and EDS analyses were performed. The SEM image can be seen in [Figure 4.4](#), where the top-view of a cylindrical sample was shown. Here, angular magnesia grains, with a varying grainsizes are present. Aluminium is well dispersed between the magnesia grains, and shows up as light grey features in the SEM. Impurities, classified as CaO and SiO₂ via EDS, are present between the magnesia grains.

A PMC-3% binder-1% Al sample was thermally treated at 1500 °C and placed in the SEM. The result of this can be seen in [Figure 4.5](#). The image location within the total sample, can be seen in [Appendix C](#). Analysis was done to show which secondary phases may have formed due to additions of aluminium. [Figure 4.5](#) shows MA spinel, aluminium carbide and some magnesia. MA spinel mainly formed on the magnesia grains. Furthermore, compared to the samples containing no aluminium, an increase in the amount of microcracking within the magnesia grains is observed. These additional results may be found in [Appendix C](#). Microcracking occurs as the stress state within the material is increased due to spinel formation [9]. SEM results showed aluminium carbide whisker formation. Whisker formation can improve creep resistance, as they are able to pin grain boundaries and hence prevent grain boundary sliding in low stress regions [23]. However, the whiskers formed locally within the sample, and were not evenly dispersed. This may locally prevent grains from sliding, but will most likely not have a substantial effect on the creep resistance.

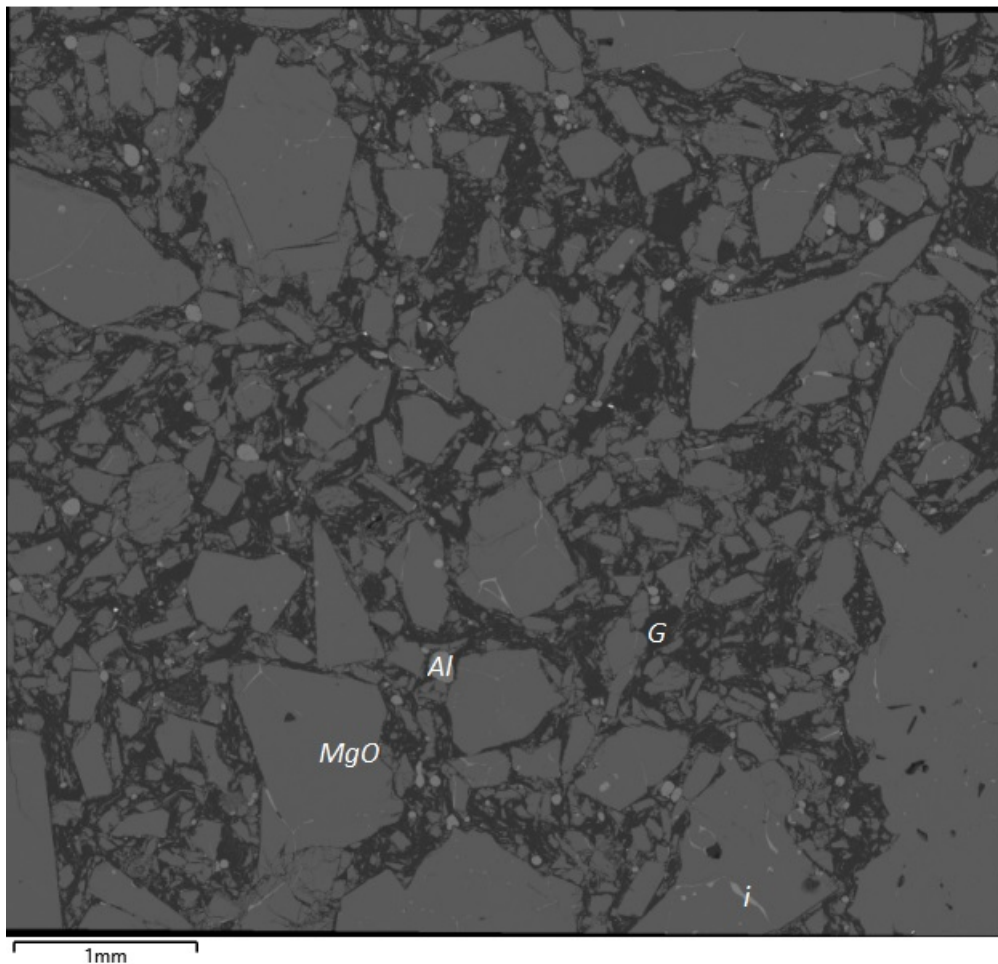


Figure 4.4: SEM image of a PMC-3% binder-1% Al green sample. Image shows aluminium (Al), magnesia (MgO), graphite (G) and impurities (i).

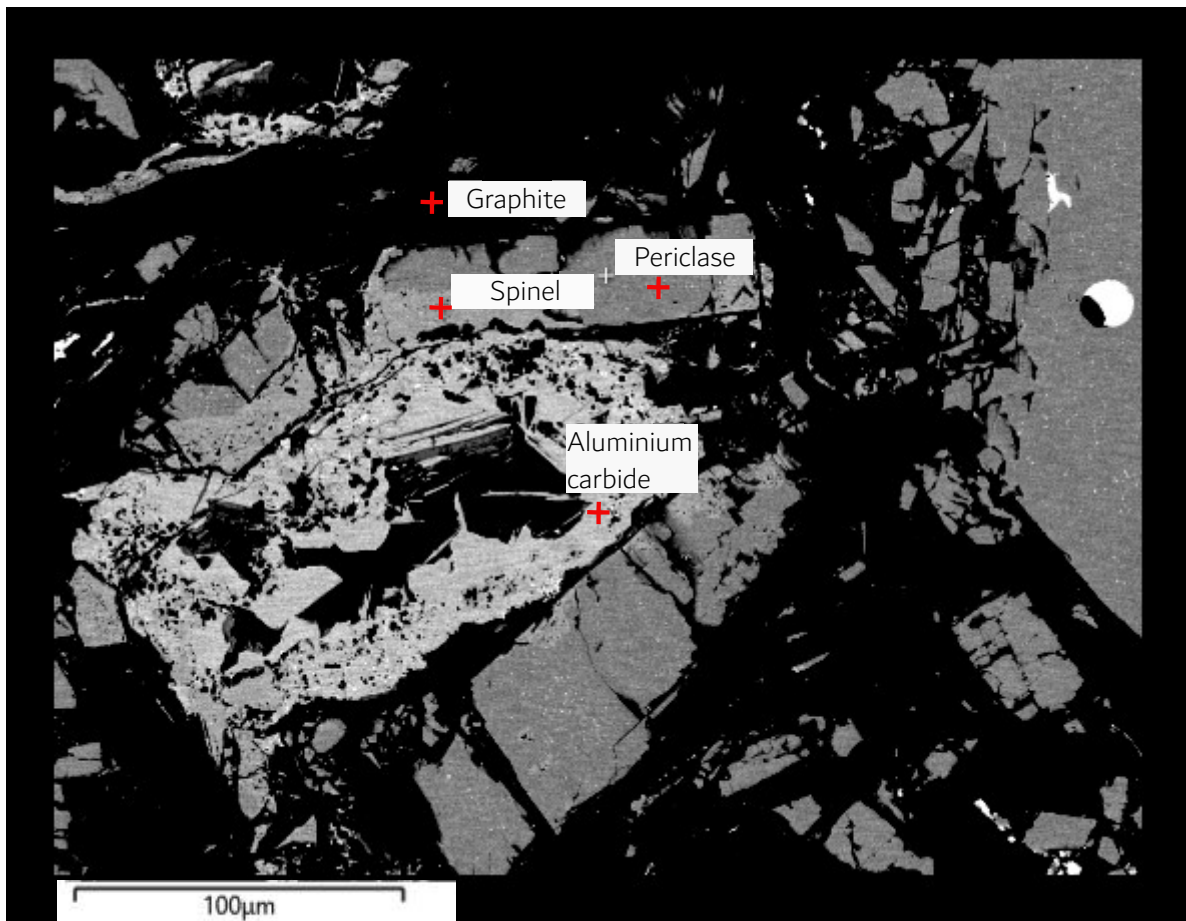


Figure 4.5: SEM image of a PMC-3% binder-1% Al sample, pre-treated at 1500 °C. Image shows carbides (AC), whiskers, MA spinel (MAS) and magnesia (MgO).

4.2. X-Ray Diffraction

The results of the XRD measurements are listed in [Table 4.1](#). These measurements were performed on green samples. The outcomes of the Rietveld refinement analyses and the XRD patterns of all the recipes are given in [Appendix C](#). All the phases present in [Table 4.1](#) are to be expected based on the used raw materials. Small amounts of wt% of Merwinite ($\text{Ca}_3\text{Mg}(\text{SiO}_4)_2$), Cronstedtite ($\text{Fe}_3[\text{Si}_2\text{O}_3](\text{OH})_4$) and Brownmillerite ($\text{Ca}_2(\text{Al,Fe})_2\text{O}_5$) formed due to impurities that are present in the MgO precursor.

Phase	PMC-2% binder		PMC-3% binder		PMC-4% binder		PMC-3% binder -1% Al		PMC-3% binder -3% Al	
	wt%	2 σ	wt%	2 σ	wt%	2 σ	wt%	2 σ	wt%	2 σ
Periclase	93.4	1.2	92.2	1.3	90.8	2.0	92.0	2.0	89.9	1.6
Graphite	5.5	1.2	7.2	1.4	8.7	2.2	6.3	2.2	6.8	1.8
Merwinite	n.d.	n.d.	0.3	0.2	0.2	0.2	n.d.	n.d.	n.d.	n.d.
Aluminium	0.2	0.1	0.2	0.1	0.2	0.1	0.9	0.1	2.6	0.1
Cronstedtite	0.3	0.1	n.d.	n.d.	n.d.	n.d.	0.3	0.1	0.2	0.1
Brownmillerite	0.4	0.2	n.d.	n.d.	n.d.	n.d.	0.3	0.2	0.3	0.2

Table 4.1: Phase distributions of all the recipes. n.d. not detected; with detection limit of $\pm 0.5\text{wt}\%$.

XRD measurements were conducted on pre-treated samples as well. Samples of the PMC-3% binder-1% Al recipe were heated to 1400 °C and 1500 °C. After cooling down to room temperature, XRD measurements were performed on the samples. The resulting phases that were present are listed in [Table 4.2](#). The outcomes of the Rietveld refinement analyses and the XRD patterns are given in [Appendix C](#). It should be noted that the XRD results from the PANalytical measurement are not shown.

The aim of this measurement was to highlight in which temperature range spinel formation could take place. However, this measurement was unsuccessful and is therefore not included.

A comparison can be made, between the XRD results of a green PMC-3% binder-1% Al sample from [Table 4.1](#) and the XRD results of the pre-treated samples in [Table 4.2](#). At 1400°C, a small amount of MA spinel (≈ 1.3 wt%) formed. This resulted in a decrease in wt% of aluminium and periclase (magnesia). A slight increase in wt% formed MA spinel at 1500 °C can be observed (≈ 1.6 wt%). For both pre-treated samples, an amorphous phase was detected. This is most likely due to formation of a glassy phase.

Phase	T=1400 °C		T=1500 °C	
	wt%	2 σ	wt%	2 σ
Periclase	91.1	0.6	89.4	0.3
Graphite	5.0	0.5	6.1	0.4
Aluminium	0.2	0.0	0.1	0.0
MA spinel	1.3	0.1	1.6	0.1
Amorphous	2.4	0.9	2.8	0.8

Table 4.2: Phase distributions of a PMC-3% binder-1% Al sample after pre-treating at 1400 °C and 1500 °C.

4.3. Permanent linear change (PLC)

The results of the PLC measurements are given in [Table 4.3](#). It should be noted that all experiments were performed twice per test temperature. The results shown in [Table 4.3](#) are average values between these two experiments. Densities and porosities were measured before and after thermal treatment at $T=T_{measure}$.

It can be observed that for all samples the density decreased and porosity increased after thermal treatment. Here, the aluminium-containing samples have the highest density and lowest porosity. Moreover, the change in porosity before and after heat treatment is the lowest for the PMC-3% binder-3% Al sample. A smaller increase in porosity after heat treatment is observed for the PMC-3% binder-3% Al samples, than for the PMC-3% binder-1% Al samples. Regarding the PLC, of all samples containing no aluminium, the PMC-2% binder samples have the lowest PLC.

	PMC-2% binder		PMC-3% binder		PMC-4% binder		PMC-3% binder -1% Al		PMC-3% binder -3% Al	
	1400	1500	1400	1500	1400	1500	1400	1500	1400	1500
$T_{measure}$ [°C]	1400	1500	1400	1500	1400	1500	1400	1500	1400	1500
Density (green) [kg/m ³]	2960	2969	3017	2998	2988	2988	2983	2994	2980	2973
Porosity (green) [%]	7.18	7.04	4.28	3.85	2.76	2.90	4.76	4.13	4.26	4.76
Density (after treatment) [kg/m ³]	2852	2863	2881	2859	2837	2838	2897	2931	2915	2901
Porosity (after treatment) [%]	13.60	13.05	12.67	12.53	12.97	13.14	11.31	10.31	6.49	7.61
PLC [%]	0.71	0.68	0.89	0.85	0.91	0.90	0.68	0.40	0.58	0.71

Table 4.3: Bulk densities and porosities of green samples (before heat treatment) and after heating up, and permanent linear change of all recipes. Experiments were conducted at room temperature.

Decreasing densities after heat treatment can be explained by increasing porosity. An increase in porosity is most likely due to volatilisation of the binder [16]. A possible explanation of the high porosity of the PMC-2% binder sample may be due to additional porosity resulting from volatilisation of magnesium. For this recipe, less binder material is available to hold the MgO grains in place. Volatilisation of magnesium is therefore expected to occur especially for the PMC-2% binder samples. Once volatilised, the magnesium will react with oxygen in the air to form MgO. This corroborates with the [Figure C.6a](#) in [Appendix C](#), where newly formed MgO was deposited on the outside of the samples.

It is most likely that more spinel was able to form for the PMC-3% binder-3% Al recipe compared to the PMC-3% binder-1% Al recipe. As a result, more volume expansion occurs and hence more pore closure. The higher volume expansion of the PMC-3% binder-3% Al can be confirmed by the higher PLC at 1500 °C. An increase in spinel content may therefore contribute to a smaller increase in porosity after thermal treatment.

The results imply that a competition may exist between: pore filling due to expansion of phases, and pore forming due to volatilisation. Which process dominates at certain temperatures, may differ for each recipe. If more material is volatilised, this will most likely decrease the PLC after heat treatment. For instance, the lowest PLC was obtained for the PMC-2% binder samples, compared to the other recipes which did not contain aluminium. This might be due to increasing volatilisation of the binder and magnesium, which is in agreement with the observed porosities. The highest PLC is obtained for the PMC-4% binder samples. A possible explanation of this result can be attributed to the higher binder content. As there is more binder material available to hold the MgO grains in place, this may lead to less magnesium volatilisation since the binder volatilisation is expected to increase.

It should be noted that the PLC is a sensitive measurement. Therefore all results are subjected to measurement uncertainties. In addition, all samples are taken from bricks which have a heterogeneous microstructure. Therefore, densities and porosities differ throughout samples taken from the same brick. Sample heterogeneity and measurement uncertainties can therefore lead to discrepancies in the data shown in [Table 4.3](#).

4.4. Cold crushing strength (CCS)

The CCS was measured twice for each recipe, and is represented in [Figure 4.6](#). It can be observed that an increase in binder content resulted in an increase in CCS. In addition, the CCS further increased for the aluminium-containing samples. The highest CCS was obtained for the PMC-3% binder-1% Al sample.

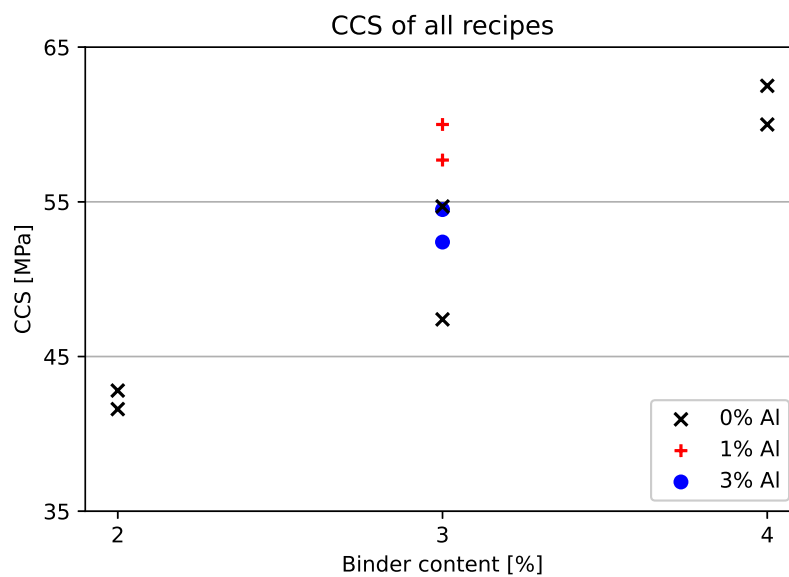


Figure 4.6: Cold crushing strength of all recipes versus binder content.

The binder serves as a bonding agent, and hence acts as reinforcement of the magnesia grains [15]. Therefore, a decrease in binder content may decrease the adhesive strength and subsequently weaken the bond between the binder and magnesia grains. This may be a possible explanation for the decreasing CCS with decreasing binder content. Aluminium may add rigidity and impede crack propagation [21] within the samples. It was therefore expected that the samples containing 3% Al would yield a higher CCS. However, the results shown in [Figure 4.6](#) are not in agreement with this hypothesis. An explanation for this may be sample heterogeneity. The samples used for the CCS measurement may have been taken from a part of the brick where the aluminium was not as well dispersed. This may lead to a locally lower aluminium content in the 'PMC-3% binder-3% Al' sample, and hence may result in a lower CCS.

4.5. Hot modulus of rupture (HMOR)

The HMOR was determined for all recipes at 1400 °C and 1500 °C, and is shown in [Figure 4.7](#) and [Figure 4.8](#), respectively. Increasing HMOR with increasing binder and aluminium content can be observed here. Moreover, it can be seen that the HMOR decreased with increasing test temperature.

From the XRD measurements, it can be concluded that at 1400 and 1500 °C, MA spinel is able to form. Due to the volume expansion, the stress state within the material is increased. As a result, microcracking may occur. Microcracks enhance the strength, as they decrease the amount of available energy required for crack propagation [9]. This may explain the increase in strength with increasing aluminium content. However, an optimum amount of spinel is required, as an excess may lead to a higher extent of micro cracking. As a result, the strength deteriorates [9]. Nevertheless, the results indicate that in this regime (1-3% Al), having spinel in the material is beneficial.

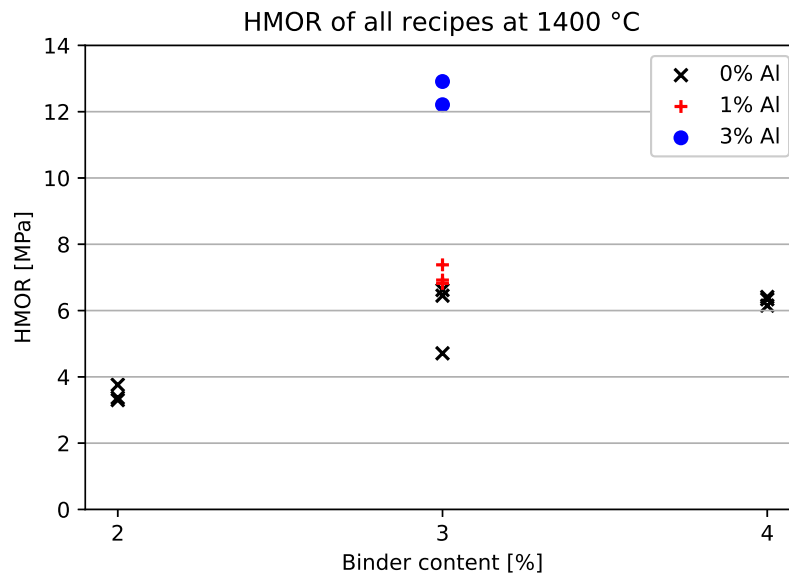


Figure 4.7: Hot modulus of rupture of all recipes, tested at 1400 °C.

A decrease in strength at higher temperatures may be related to an increase in volatilisation and formation of defects. The HMOR values at 1500 °C are indeed lower than the HMOR values found at 1400 °C. In [Figure 4.8](#), the HMOR at 1500 °C of the PMC-3% binder-1% Al is ≈ 1.5 times higher than the HMOR of the PMC-3% binder sample. XRD measurements showed a spinel content of only 1.6 wt% at 1500 °C. This HMOR increase provides a first indication of the contribution of MA spinel formation on this thermo-mechanical property.

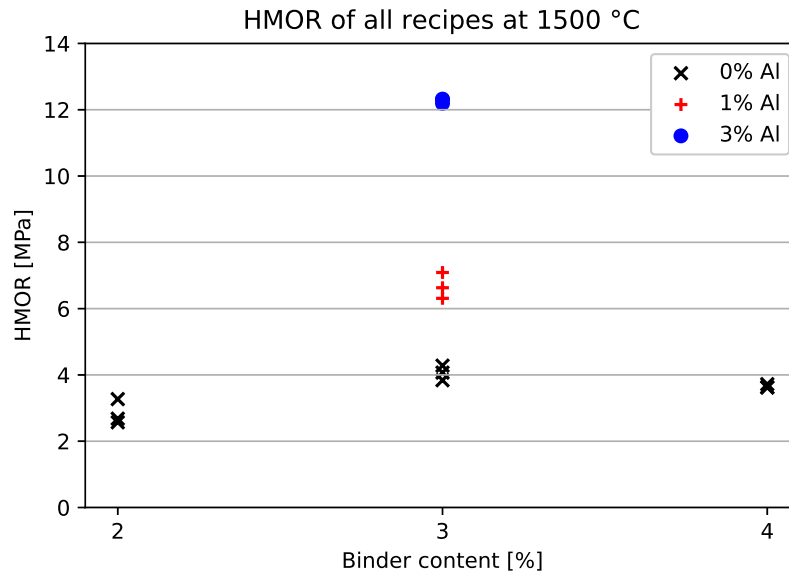


Figure 4.8: Hot modulus of rupture of all recipes, tested at 1500 °C.

4.6. Dilatometry

The dilatometry measurements were conducted to show the materials expansive behaviour at high temperatures. This can be related to phase transformations and burnout of material within the samples. All samples were heated up to 1600 °C and then cooled down. The results are shown in [Figure 4.9](#), [Figure 4.10](#) and [Figure 4.11](#). It should be noted that the dilatometry measurement for the PMC-2% binder recipe was conducted in a non-reducing environment. Other measurements were conducted in a reducing environment.

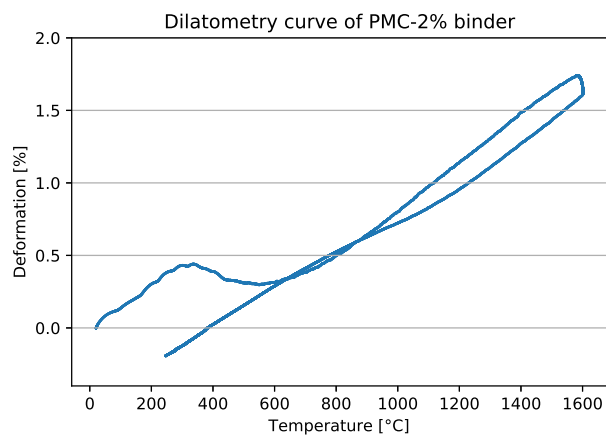


Figure 4.9: Dilatometry curve of a PMC-2% binder sample.

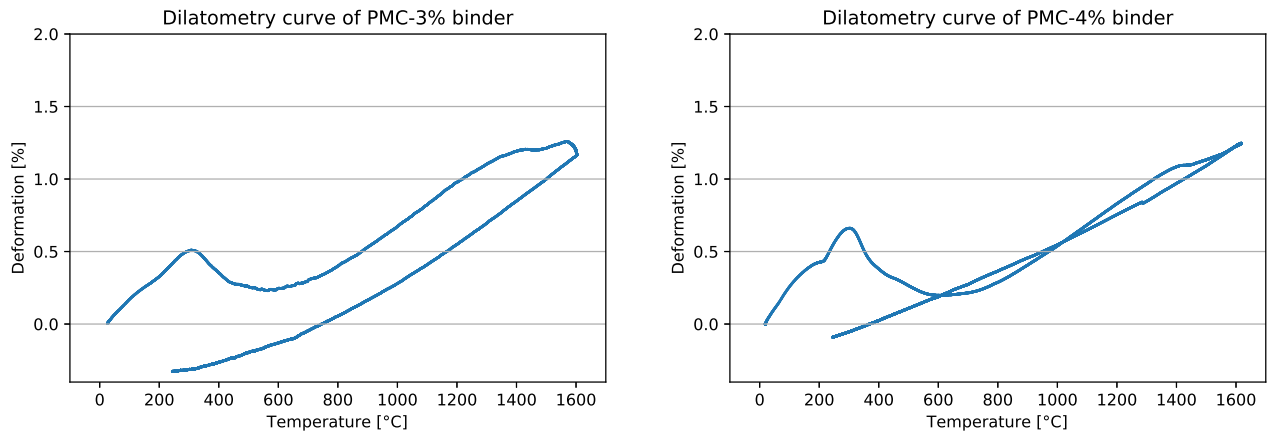


Figure 4.10: Dilatometry curve of a PMC-3% binder sample (left) and a PMC-4% binder sample (right).

When comparing the results between the PMC-2%, 3% and 4% binder samples, a similar trend can be seen between 0-400 °C. An increase in the amount of expansion is seen between 0-300 °C. A possible explanation for this expansion may be that the samples were heated through their glass transition temperature (T_g). When the material is heated through its T_g , the structural units are free to move and the volume of the glass increases at a faster rate than at temperatures below T_g [8]. From 300-400 °C, the samples contract. This may be related to volatilisation of the binder.

When comparing the results in [Figure 4.9](#) and [Figure 4.10](#), it can be observed that the PMC-2% binder sample expanded the most. The PMC-2% binder contained the least amount of material holding the MgO grains together. Due to this, it is likely that the MgO grains could expand more freely. However, it is difficult to corroborate this statement as the experiment for the PMC-2% binder sample was conducted in a non-reducing environment, which most likely influenced the result shown in [Figure 4.9](#).

Comparing the dilatometry results of the PMC-3% binder to the PMC-3% binder-1% and 3% Al ([Figure 4.11](#)) shows the effect of adding aluminium in to the system. It is most likely that spinel formation, and its accompanying volume expansion, explain why the aluminium-containing samples expanded more than the PMC-3% binder sample. The maximum expansion was ≈ 1.33 times higher when increasing aluminium content from 0 to 1%. Moreover, the maximum expansion was ≈ 1.50 times higher when further increasing aluminium content from 0 to 3%.

The offset of the dilatometry curves implicates if the sample shrunk or expanded compared to its original dimension before testing. This offset can be compared to the PLC values, which are expected to be in agreement with each other. However, this is not the case. It is not clearly understood why these two experiments are deviant. Therefore, it is recommended to test the validity of the PLC and dilatometry measurements for future works.

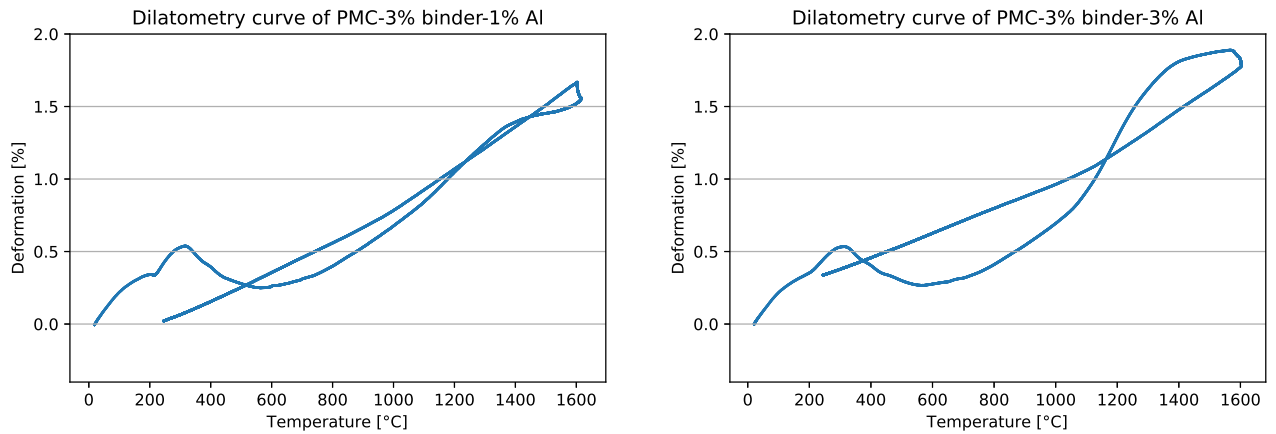


Figure 4.11: Dilatometry curve of a PMC-3% binder-1% Al sample (left) and a PMC-3% binder-3% Al sample (right).

CTEs can be determined for all samples from the dilatometry curves. This is done in the temperature range of 1000-1600 °C, as the material will find its usage at these temperatures. The CTEs are listed in [Table 4.4](#). PMC-3% binder-3% Al has the highest CTE. This is expected as more spinel formation (compared to the 1% Al sample) will result in more expansion. The CTE of the PMC-2% binder sample could be attributed due to the free expansion of MgO as less binder is holding the grains in place. Another explanation may be related to the oxidising atmosphere during testing. Testing in a non-reducing environment may have resulted in more volatilisation of the matrix. This may have exposed the MgO grains further and allowed faster expansion, resulting in a higher CTE. The PMC-3% binder sample has the lowest CTE. It is possible that, an increase in binder content results in more cross-linking between the carbon chains. As a result, the material will be more rigid at higher temperatures. This will decrease the amount of expansion and therefore result in a lower CTE.

The XRD results showed a spinel content of only 1.6 wt% at 1500°C for the PMC-3% binder-1% Al recipe. The dilatometry results for this recipe showed an increase of 33% of maximum obtained expansion, and a 61% increase in CTE. This results provide another indication of the contribution of MA spinel formation on these thermo-mechanical properties.

	PMC-2% binder	PMC-3% binder	PMC-4% binder	PMC-3% binder -1% Al	PMC-3% binder -3% Al
CTE [$10^{-5} \text{ } ^\circ\text{C}^{-1}$]	1.463*	0.871	1.151	1.405	1.880

Table 4.4: Coefficients of thermal expansion for all recipes, determined between 1000-1600 °C. * measured in non-reducing atmosphere.

4.7. Refractoriness under load (RuL)

The refractoriness under load shows the sample deformation whilst heating up. These results are shown in [Table 4.5](#). It should be noted that the device was only able to heat up until 1600 °C. Therefore, samples were kept at 1600 °C for a few hours with the purpose of possibly retrieving $T_{0.5}$. However, only T_0 was found, and is reported in [Table 4.5](#). As no $T_{0.5}$ was found during the experiments, it can be said that the refractoriness of all recipes is adequate enough for them to be safely used at 1600 °C. Graphical representations of the refractoriness under load, can be found in [Appendix C](#).

	PMC-2% binder	PMC-3% binder	PMC-4% binder	PMC-3% binder -1% Al	PMC-3% binder -3% Al
T_0 [°C]	1485	1579	1565	1608	1401
Max deformation [%]	1.2523	1.4695	1.2501	1.5875	1.6822

Table 4.5: Refractoriness under load results for all recipes.

4.8. Hot compressive strength (HCS)

The hot compressive strength (HCS) is measured to determine the ultimate compressive strength (UCS). This is the maximum amount of stress that the samples can withstand whilst being compressed before breaking [20]. The UCS will be used as a measure to determine which load regimes may be applied to the samples during creep testing. It should be noted that the UCS was not determined for the PMC-3% binder-3% Al recipe, as creep testing could not be performed on these samples. This will be discussed in Section 4.9.

The HCS graphs can be found in Appendix C, and the UCS values are shown in Table 4.6. A trend is observed of decreasing UCS with increasing temperature. Similar behaviour was seen for the HMOR results. A decrease in strength at higher temperatures may be related to an increase in volatilisation and formation of defects. It is expected that the material may soften with increasing temperature. This can be corroborated by the Young's Moduli.

PMC-2% binder has the lowest UCS at both test temperatures. This is in agreement with the CCS and HMOR results. PMC-3% binder-1% Al has the highest UCS. This is most likely due to spinel formation. When comparing to PMC-3% binder, a low spinel content at 1400 °C (1.3wt%) and 1500 °C (1.6wt%) resulted in an increase in UCS of 15% and 27%, respectively. The UCS is another thermo-mechanical property which improved due to contribution of MA spinel formation.

	PMC-2% binder		PMC-3% binder		PMC-4% binder		PMC-3% binder -1% Al	
$T_{measure}$ [°C]	1400	1500	1400	1500	1400	1500	1400	1500
UCS [MPa]	17.33	13.67	26.93	21.25	28.06	23.45	31.04	26.98
E modulus [MPa]	1200	900	3600	2600	2900	2600	2100	1900

Table 4.6: Ultimate compressive strength values measured at 1400 °C and 1500 °C.

4.9. Creep in compression

Multi stage creep experiments were conducted for all recipes that did not contain aluminium. In addition, creep testing was done on the PMC-3% binder-1% Al recipe as well. This recipe was chosen, to highlight the effect of increasing aluminium content from 0 to 1% on creep resistance.

A main outcome of the creep measurements are experimental strains and strain rates. An example of this data is visualised in Figure 4.12 and Figure 4.13, respectively. The different colours in Figure 4.12 and Figure 4.13 indicate the different loads that were altered after every 5 hours. The temperature of the experiments are kept constant, in this case at $T = 1500$ °C.

A single stage creep measurement was performed to test the validity of the multi stage creep experiments. A PMC-3% binder sample was tested at $T = 1500$ °C and loaded with 8 MPa. The result is shown in Figure 4.14. The experimental creep rates are determined by taking the average experimental strain rate over the last 2 hours of each load regime. This was done for the multi- and single stage measurement, and is shown in Table 4.7.

As described in Section 3.2.2, criteria are in place for selecting experimental creep rates for the model. As a result, it should be noted that:

- All experimental creep rates stated in this chapter are the average rates taken over the last 2 hours of data from a load stage.
- If the UCS is known, the experimental load regimes can be defined with certainty. Experimental creep rates must result from applied loads that are <50% of that materials UCS. The UCS is therefore ideally a parameter that is determined before creep testing commences. However, during this thesis, the UCS was determined after creep testing. This decreased the efficiency of all previously conducted experiments. As a result, experimental data had to be disregarded.

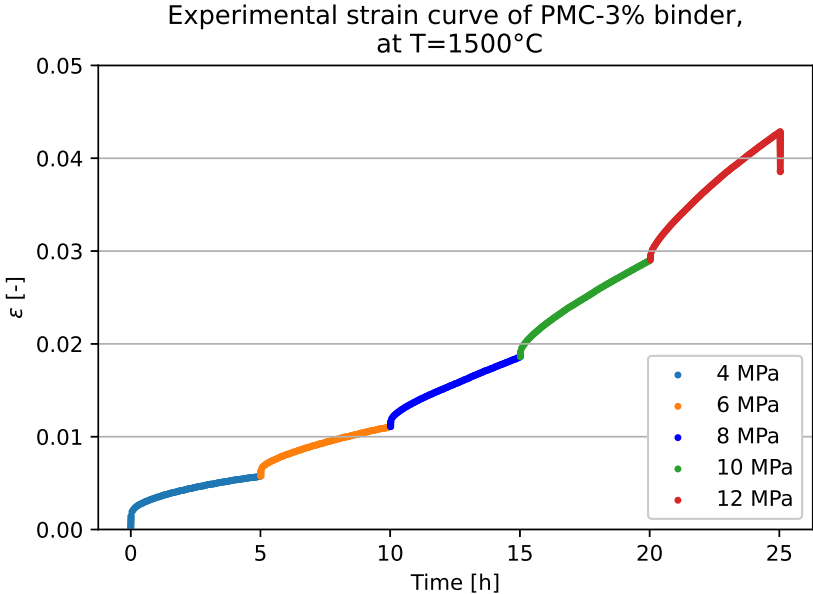


Figure 4.12: Experimental strain curve of PMC-3% binder T = 1500 °C.

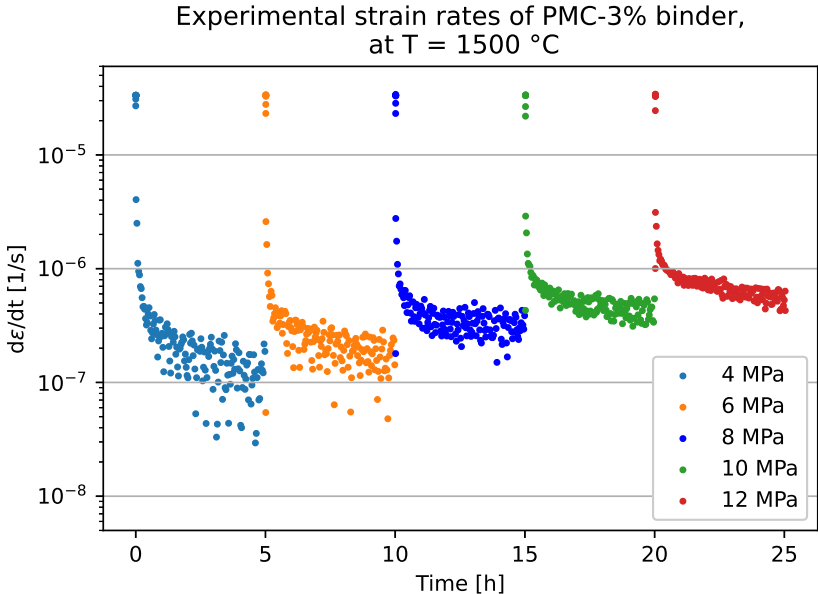


Figure 4.13: Experimental strain rates of a multi stage measurement, testing a PMC-3% binder sample at T = 1500 °C.

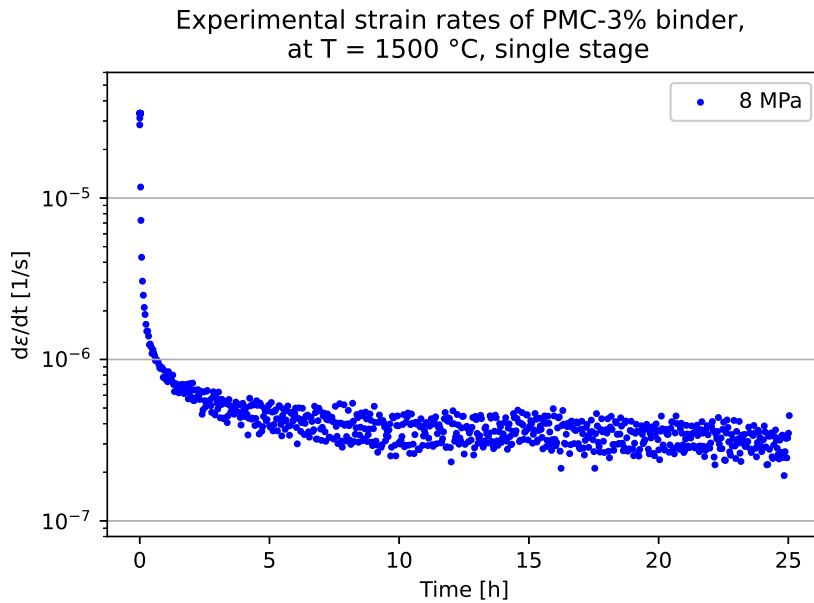


Figure 4.14: Experimental strain rates for a single stage measurement at 8 MPa for a PMC-3% binder sample at T=1500 °C.

Time [h]	Load single [MPa]	Experimental creep rate single [$\cdot 10^{-9} s^{-1}$]	Load multi [MPa]	Experimental creep rate multi [$\cdot 10^{-9} s^{-1}$]
5	8	479	4	127
10	8	372	6	182
15	8	364	8	320
20	8	332	10	440
25	8	307	12	589

Table 4.7: Creep rates with corresponding loads for single and multi stage experiment.

As seen in [Table 4.7](#), a decreasing trend of creep rates for the single stage measurement is present. However, the rates fluctuate less after $t=10$ h. This can be seen in [Figure 4.14](#) as well, where the slope of the graph becomes more constant. A statement can therefore be made, regarding the validity of the multi stage measurement. The creep rate of the multi stage measurement at $p = 8$ MPa, shown in [Table 4.7](#), is $320 \cdot 10^{-9} s^{-1}$. This is faster than the final single stage creep rate ($307 \cdot 10^{-9} s^{-1}$). The difference in rates between the multi and single stage is 5%. The current experimental configuration (5h per load stage) therefore overestimated the creep rates, compared to the single stage configuration. However it can be argued that an overestimation of creep rates of 5% is within the allowed measurement error. This implies that creep testing can be less conservative compared to standardised testing. As a result, more data can be retrieved in a shorter period of time. The comparison between the multi- and single stage creep rates, highlights the benefits of the experimental configuration used in this thesis. Nevertheless, in order to reduce the overestimation of 5%, it is suggested to re-evaluate the multi stage set-up. A suggestion may be to reduce the amount of load stages from 5 to 3, and increase the testing time per load stage, from 5h to 10h. However, this statement requires further validation.

An overview of all creep experiments per recipe is shown in [Section C.5](#). Here data which was discarded based on the model criteria is shown. The pressures, temperatures and experimental creep rates that were used for the model, are shown in [Table 4.8](#).

PMC-2% binder			PMC-3% binder			PMC-4% binder			PMC-3% binder-1% Al		
Pressure [MPa]	Temperature [°C]	Experimental creep rate [1/s]	Pressure [MPa]	Temperature [°C]	Experimental creep rate [1/s]	Pressure [MPa]	Temperature [°C]	Experimental creep rate [1/s]	Pressure [MPa]	Temperature [°C]	Experimental creep rate [1/s]
4	1350	6.08E-08	6	1350	5.81E-08	8	1350	1.11E-07	4.3	1350	7.81E-08
6	1350	1.71E-07	8	1350	5.96E-08	10	1350	2.24E-07	6.4	1350	7.81E-08
8	1350	3.83E-07	10	1350	1.11E-07	6	1400	5.97E-08	8.6	1350	1.45E-07
4	1350	4.39E-08	12	1350	1.50E-07	8	1400	1.05E-07	6	1375	4.40E-08
6	1350	1.45E-07	4	1400	3.09E-08	10	1400	1.28E-07	8	1375	6.82E-08
8	1350	1.65E-07	6	1400	1.16E-07	12	1400	1.61E-07	10	1375	7.43E-08
4	1375	2.37E-08	8	1400	1.04E-07	4	1425	5.27E-08	2	1400	2.35E-08
6	1375	4.72E-08	10	1400	1.15E-07	8	1425	1.17E-07	4	1400	3.49E-08
8	1375	1.15E-07	12	1400	2.35E-07	12	1425	2.49E-07	6	1400	6.20E-08
4	1400	1.01E-07	4	1425	5.53E-08	6	1450	9.65E-08	8	1400	1.02E-07
6	1400	9.83E-08	6	1425	7.62E-08	8	1450	1.66E-07	10	1400	2.12E-07
8	1400	1.55E-07	8	1425	1.48E-07	10	1450	2.32E-07	2	1450	7.53E-09
2	1400	1.07E-07	10	1425	1.72E-07	12	1450	4.00E-07	4	1450	4.09E-08
4	1400	2.14E-07	4	1450	6.72E-08	6	1475	1.14E-07	6	1450	1.24E-07
6	1400	5.11E-07	6	1450	9.60E-08	8	1475	1.83E-07	8	1450	1.71E-07
2	1425	4.67E-08	8	1450	1.92E-07	10	1475	2.21E-07	10	1450	3.16E-07
4	1425	8.79E-08	10	1450	2.40E-07	2	1500	5.53E-08	2	1500	1.48E-08
6	1425	1.79E-07	6	1500	1.83E-07	4	1500	1.41E-07	4	1500	8.07E-08
8	1425	3.19E-07	8	1500	3.20E-07	6	1500	1.83E-07	6	1500	1.80E-07
6	1450	1.30E-07	2	1525	9.53E-08	8	1500	2.38E-07	8	1500	2.07E-07
4	1475	2.31E-07	4	1525	1.79E-07	10	1500	3.12E-07	10	1500	2.67E-07
6	1475	4.99E-07	6	1525	3.58E-07	4	1550	3.37E-07	2	1525	7.41E-08
4	1500	1.37E-07	8	1525	5.10E-07	6	1550	5.11E-07	6	1525	2.69E-07
4	1500	2.33E-07	4	1550	3.19E-07	8	1550	7.35E-07	8	1525	3.55E-07
6	1500	2.55E-07	6	1550	5.54E-07				10	1525	4.83E-07
6	1500	1.67E-07									

Table 4.8: Experimental pressures, temperatures and creep rates that were used for the model.

After inserting the data from [Table 4.8](#) in to the model, coefficients C_1 , C_2 and C_3 could be retrieved and listed in [Table 4.9](#). Their definitions are described in [Section 3.2.2](#). Model coefficients C_2 is the highest for the PMC-2% binder recipe, compared to the other recipes which did not contain aluminium. As C_2 represents the stress exponent n , an increase in C_2 will result in an exponential increase in the creep rate. Furthermore, a higher n may imply that the creep rate of the material was more influenced by stress than the other recipes. The higher sensitivity to influence of applied stress was seen during HCS, CCS and HMOR measurements as well. For all aforementioned measurements, it was found that this recipe has the lowest strength, which could have resulted in faster failure mechanisms.

The PMC-2% binder recipe has the lowest C_1 and C_3 of all non aluminium-containing recipes. C_3 is defined as \exp^{-C_3} , where $C_3 = Q_{act}/R$. Therefore, a lower C_3 will result in a lower Q_{act} and hence an increase in creep rate. It might be that, a lower activation energy lowers the energy barrier for the material to creep. It is therefore desirable to have a high C_3 , as this increases Q_{act} and hence decreases the creep rate. C_1 is defined as a material constant. By definition, an increase in C_1 will lead to an increase in creep rate. However, this factor influences the creep rate less than C_2 and C_3 , as it is inserted as a multiplier and not an exponential like C_2 and C_3 .

Modelled creep rates are represented in isoplots in [Figure 4.15](#), [Figure 4.16](#), [Figure 4.17](#) and [Figure 4.18](#). It should be noted that modelled data was discarded based on the UCS of the materials. As the material fails beyond the UCS, modelled creep rates should not be shown here. The UCS was experimentally determined at 1400 °C and 1500 °C and interpolated to other temperatures. The region where data was discarded is white in [Figure 4.15](#).

A few data points were chosen from the model. A comparison between modelled and experimental data was made. This may help draw conclusions on the quality of the model. Differences [%] ([Table 4.10](#)) represent the increase or decrease in creep rate between the experimental and modelled data. This was calculated as follows:

$$Differences[\%] = \frac{\dot{\epsilon}_{cr,modelled} - \dot{\epsilon}_{cr,experimental}}{\dot{\epsilon}_{cr,experimental}} \cdot 100\% \quad (4.1)$$

To further draw conclusions on the quality of the model, R^2 is determined for all recipes. This value indicates the 'goodness of fit', or in other words: it describes the quality of the model [7]. It can range between values of 0 and 1. The closer R^2 is to 1, the better the fit. All R^2 values are shown in [Table 4.11](#).

	PMC-2% binder	PMC-3% binder	PMC-4% binder	PMC-3% binder -1% AI
C1	$1.26 \cdot 10^{-9}$	$2.69 \cdot 10^{-6}$	$9.13 \cdot 10^{-5}$	$6.04 \cdot 10^{-11}$
C2	1.29	1.28	1.17	1.39
C3	$2.49 \cdot 10^4$	$3.97 \cdot 10^4$	$4.28 \cdot 10^4$	$2.43 \cdot 10^4$

Table 4.9: Model coefficients for all recipes. Recall: $\dot{\epsilon}_{II} = C_1 \cdot \sigma^{C_2} \cdot e^{-(C_3/T)}$ where $C_1 = A$, $C_2 = n$, $C_3 = \frac{Q_{act}}{R}$.

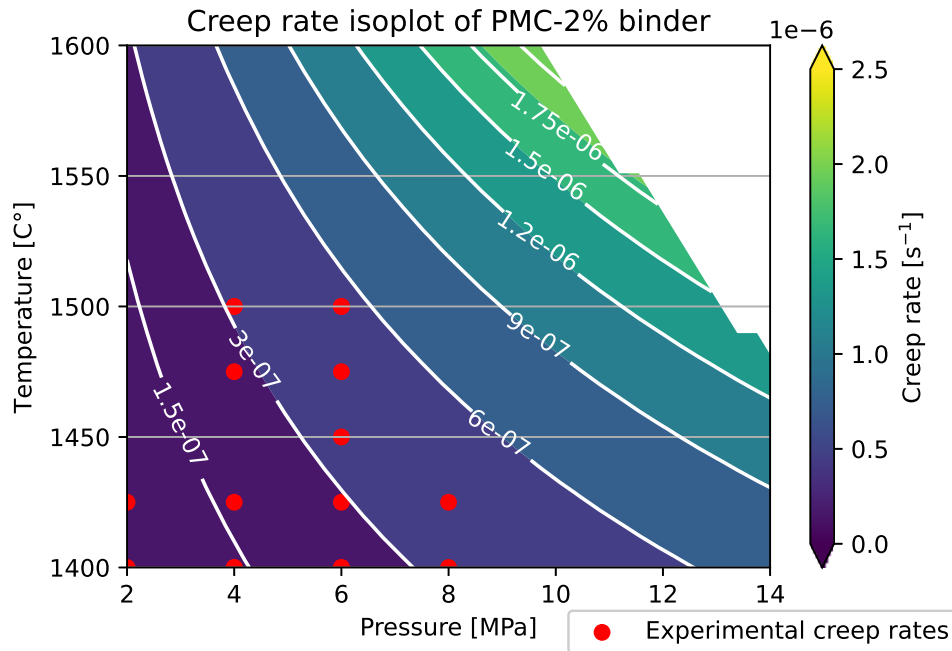


Figure 4.15: Modelled creep rate isoplot for PMC-2% binder recipe.

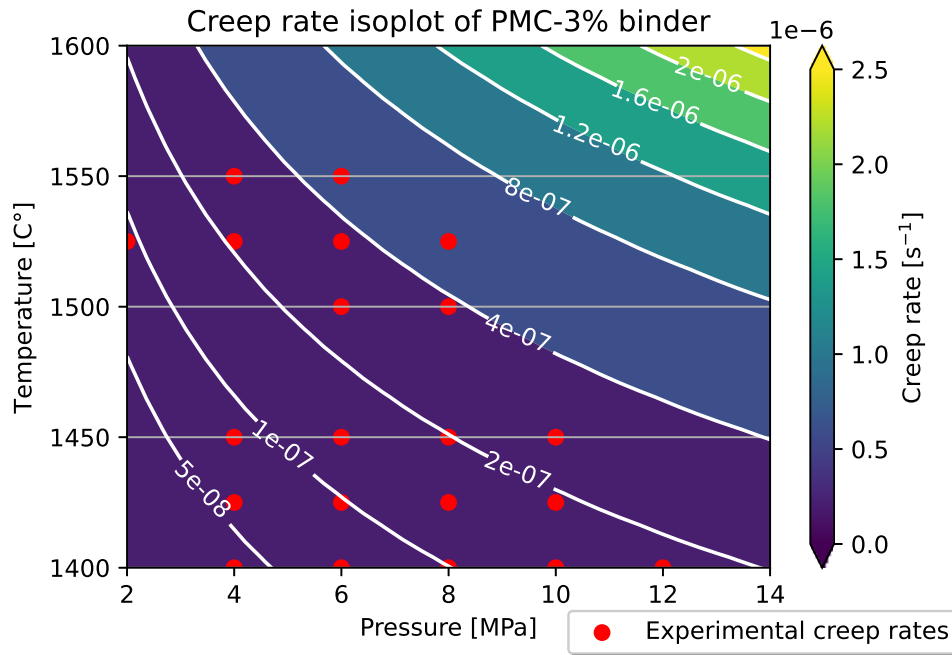


Figure 4.16: Modelled creep rate isoplot for PMC-3% binder recipe.

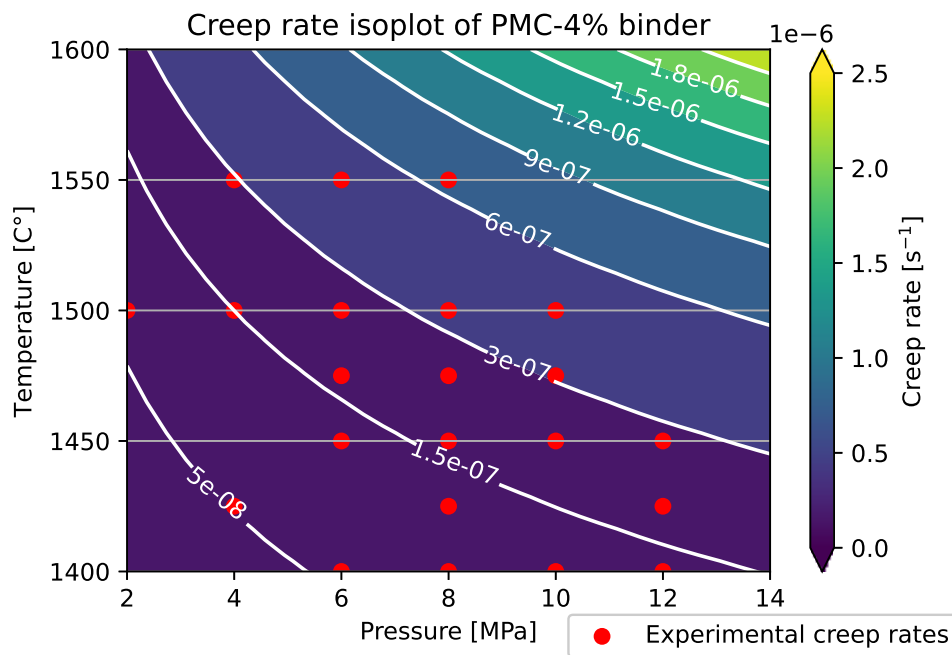


Figure 4.17: Modelled creep rate isoplot for PMC-4% binder recipe.

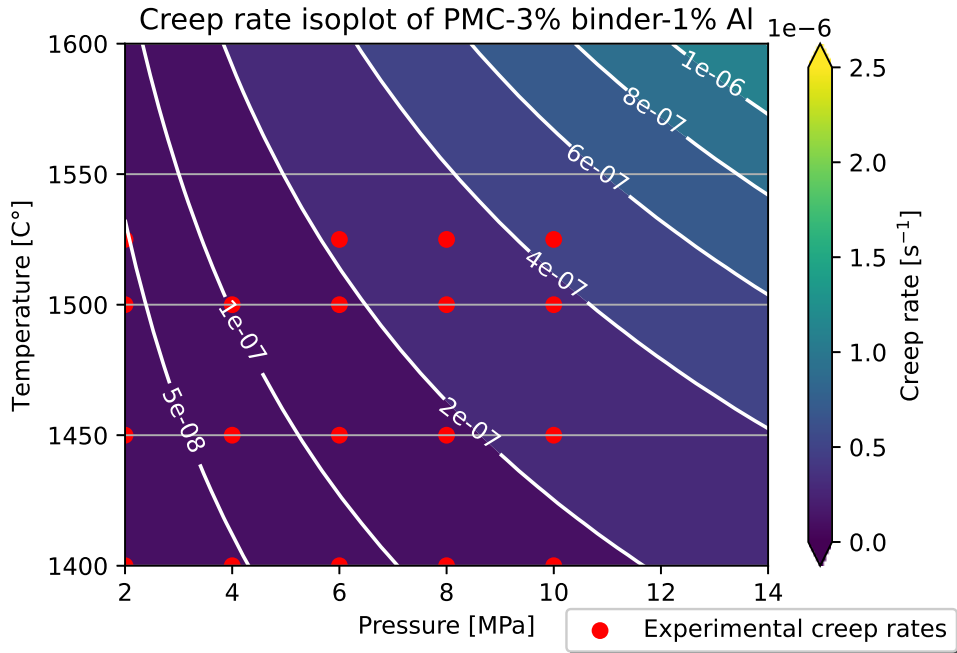


Figure 4.18: Modelled creep rate isoplot for PMC-3% binder-1% Al recipe.

Pressure [MPa]	T [°C]	PMC-2% binder Differences [%]	PMC-3% binder Differences [%]	PMC-4% binder Differences [%]	PMC-3% binder -1% Al Differences [%]
4	1500	+47.6	n.d.	+16.3	+2.22
6	1500	+115.3	+47.5	+36.6	+37.5
6	1450	+183.8	+49.0	+30.6	+0.8
4	1425	+113.9	+16.6	+9.68	n.d.
8	1425	+32.3	-2.03	+2.56	n.d.
6	1400	+146	-37.0	+2.35	+33.7
8	1400	+120	-1.92	-20.8	+17.6

Table 4.10: Experimental and modelled creep rates and their corresponding differences.

	PMC-2% binder	PMC-3% binder	PMC-4% binder	PMC-3% binder -1% Al
R ² [-]	0.59	0.70	0.91	0.96

Table 4.11: R² for all recipes.

Residual creep rate maps were made as well. The residual maps show the difference in modelled creep rates between the different recipes. These can be found in Section C.5. The residuals can be translated into difference maps. These maps show the decrease and/or increase in the amount of differences in modelled creep rates, when increasing binder or aluminium content. These values are determined by:

$$Differences[\%] = \frac{\dot{\epsilon}_{cr,i} - \dot{\epsilon}_{cr,i+1}}{\dot{\epsilon}_{cr,i}} \cdot 100\% \quad (4.2)$$

Where in Equation 4.2, the *i* represents the binder or aluminium content. The difference maps are shown in Figure 4.19, Figure 4.20 and Figure 4.21.

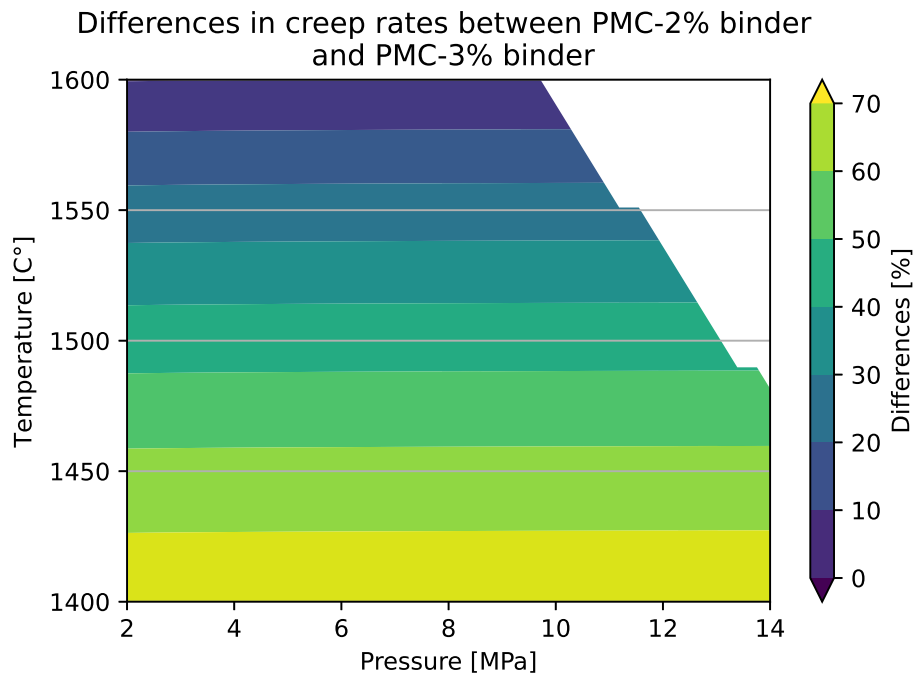


Figure 4.19: Differences in creep rates between PMC-2% binder and PMC-3% binder.

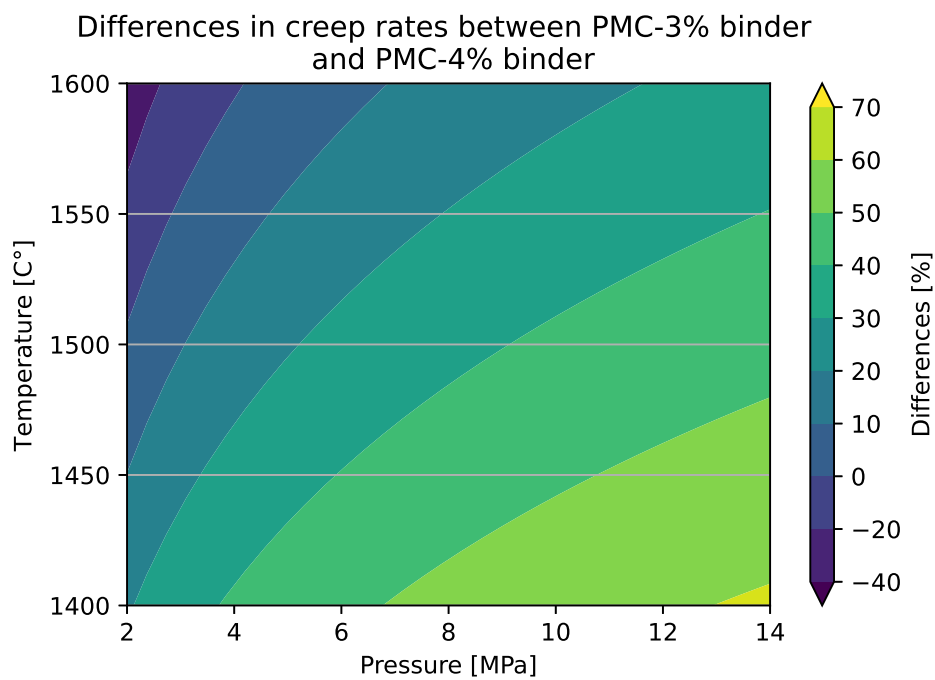


Figure 4.20: Differences in creep rates between PMC-3% binder and PMC-4% binder.

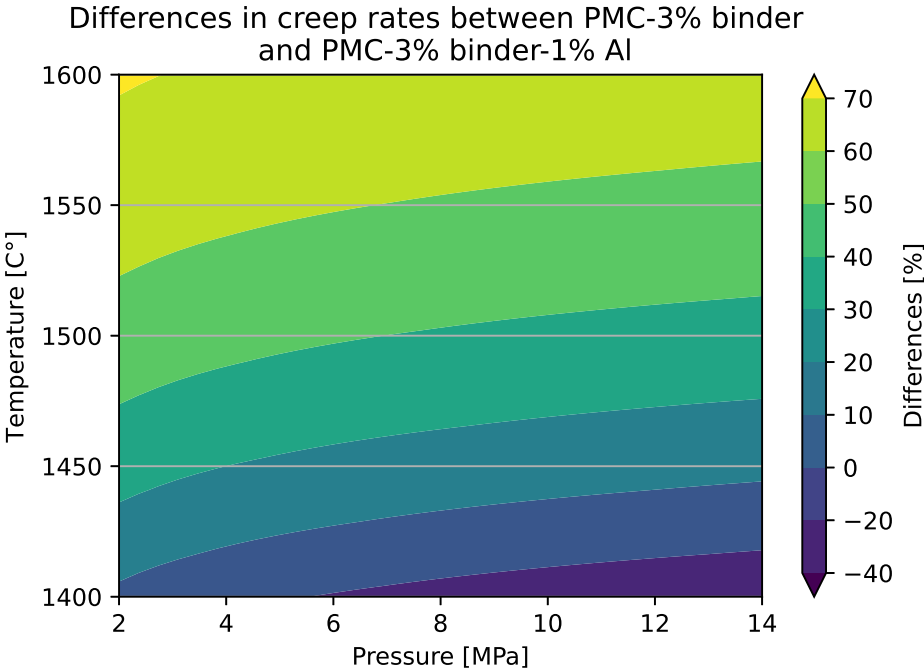


Figure 4.21: Differences in creep rates between PMC-3% binder and PMC-3% binder-1% Al.

4.9.1. Effect of increasing binder content on creep development

When comparing [Figure 4.15](#), [Figure 4.16](#) and [Figure 4.17](#), a trend is seen of decreasing creep rates with increasing binder content. A competition may exist between the amount of carbonisation and volatilisation. Both processes will occur within the samples with increasing temperature. This statement can be corroborated by the dilatometry results as all samples showed negative and positive deformation. Which of the two processes is dominant at a certain temperature, may influence the creep resistance.

Increasing carbonisation with increasing binder content is expected, due to the higher carbon content as seen from the XRD results in [Table 4.1](#). Increasing carbonisation and CTE mismatch may decrease porosity and increase the density of the total material at high temperatures. This behaviour can be confirmed by the PLC results in [Table 4.3](#). Increasing carbonisation may improve the rigidity due to cross-linking of the carbon chains. This could contribute to an improvement in strength, which can be confirmed by the CCS, HMOR and UCS results. In addition, increasing carbonisation may decrease the effective CTE of the total material. This can be verified by the CTE data in [Table 4.4](#). A decrease in porosity and effective CTE, and an increase in density and strength, will most likely increase the grain boundary sliding resistance. As a result, creep resistance increases with increasing binder content.

Increasing volatilisation may weaken the material. The creep samples of the PMC-2% binder recipe showed deposition of MgO on the outside of the samples ([Figure C.6a](#)) due to volatilisation. This phenomena did not occur for the other recipes. Volatilisation of magnesium may be an indication that the forces between the particles in the material was weaker compared to other recipes. This may be a possible explanation for the poor creep resistance of the PMC-2% binder recipe.

To further quantify the effect of increasing binder content on creep resistance, the difference maps in [Figure 4.19](#) and [Figure 4.20](#) should be analysed. A high percentage of positive differences translates to an improvement in creep resistance with increasing binder content. [Figure 4.19](#) shows a trend of increasing creep resistance with increasing binder content, and decreasing temperature. Here, a maximum decrease in creep rate of 80% was obtained. This is in agreement with the hypotheses that were made in the previous paragraphs. Increasing binder content resulted in an increase in HMOR and UCS, a decrease in porosity and effective CTE.

At higher temperatures, the difference in creep rates between the PMC-2% binder and PMC-3% binder is less profound (20%, seen in [Figure 4.19](#)). Weakening of both recipes is expected with increasing temperature, due to increasing volatilisation and porosity (confirmed by the HMOR and UCS results). However, this is not in agreement with the PLC results. A decrease in porosity was observed for the PMC-2% binder recipe from 1400 °C to 1500 °C. This is most likely due to the free expansion of the magnesia grains, and as a result conglomeration to form the magnesia skeleton. This magnesia skeleton formation can be verified by the microscopy image in [Figure 4.2](#). Increasing porosity due to volatilisation, in symbiosis with decreasing porosity due to the magnesia skeleton, may have decreased the porosity with increasing temperature for the PMC-2% binder sample. As a result, decreasing creep resistance with increasing temperature is observed.

[Table 4.10](#) shows that PMC-2% binder had the highest % differences between the experimental and modelled data, and the lowest R^2 value ([Table 4.11](#)). This questions the validity of the PMC-2% binder creep model, especially at high temperatures and pressures. The spread in experimental data points, seen in [Figure 4.15](#) is less compared to the other recipes. Experimental data at high pressures (>8 MPa) and temperatures (>1500 °C) could not be retrieved for this recipe. Having a better spread of experimental data should improve the quality of the model.

A further increase of binder content from 3% to 4% showed a trend of increasing creep resistance with increasing binder content. The difference map in [Figure 4.20](#) showed an increase in creep resistance with decreasing temperature and increasing pressure. Here, a maximum decrease in creep rate of 30% was obtained. Interestingly, a negative difference is seen in the low pressure region (2-3 MPa) between ≈ 1550 -1600 °C. This translates to better creep resistance of the PMC-3% binder recipe in this region. Here, as seen in [Table 4.8](#) experimental data was scarce. The model did not have experimental

creep rates at low pressures and high temperatures as an input. This may have decreased the quality of the model. In addition, this behaviour is not in agreement with the other deformation experiments (dilatometry and refractoriness under load). The results from these experiments show more deformation (at low pressures and high temperatures) for the PMC-3% binder sample. Therefore, the negative amount of differences may be attributed due to poor quality of the model in this region. Elsewhere, the PMC-4% binder recipe creeps at a slower rate than the PMC-3% binder recipe.

Figure 4.20 shows an extra dependency of pressure, which Figure 4.19 did not. Figure 4.20 highlights a trend of increasing creep resistance with decreasing temperature and increasing pressure. Increasing pressure may cause for further densification and conglomeration of the material, hence strengthening it. In Figure 4.19 this trend was not observed. This is most likely counterbalanced due to the densification of the material due to formation of the magnesia skeleton.

4.9.2. Effect of increasing aluminium content on creep development

Analysing the difference map in Figure 4.21 shows a trend of increasing creep resistance with increasing aluminium content from 0 to 1%. A maximum decrease in creep rate of 70% can be observed. When observing the results from the CCS, HMOR and UCS experiments, increasing the aluminium content from 0% to 1% increases the strength of the material. Where the CCS increased by 15%, HMOR and UCS increased by 34% and 15% at 1400 °C (respectively) and 65% and 27% at 1500 °C (respectively).

Before creep testing, all samples are kept at the test temperature for 5 hours to allow homogenisation of the sample. For the PMC-3% binder-1% Al, it was assumed that all spinel formed before creep testing commenced. However, it could be that during the first few hours of testing, spinel formed. Spinel formation may counterbalance compressive creep, and as a result creep rates are biased. This may have impacted the creep data during the first, and possible the second load stage. It is assumed that after these stages, all spinel will have formed.

The increase in creep resistance and strength is most likely due to spinel formation. Spinel formation, due to its irreversible expansion, may form microcracks, as the stress state within the material is increased. It might be that microcracking inhibit further crack propagation, which could explain the improvement in strength and hence creep resistance. Another explanation could be that volatilisation of magnesium decreased due to spinel formation, as the MgO grains are less exposed. Improvement in strength can be confirmed by the HMOR and UCS results.

In addition, it is hypothesised that spinel may act as a sponge. Hereby entrapping impurities within the crystal lattice [9]. This inhibits the impurities from forming low melting phases. Low melting phases, if formed on grain boundaries, may decrease the sliding resistance and hence decrease creep resistance. Therefore, it could be that an improvement in strength and creep resistance may be due to the sponge-like behaviour of spinel. However, the validity of this hypothesis requires further research.

The SEM images show aluminium carbide whiskers. As stated, it is hypothesised that whiskers may be able to pin grain boundaries, and hence prevent grain boundary sliding [23]. However, SEM results showed that these whiskers formed in small quantities, and locally within the material. Therefore, the impact that these whiskers may have on creep resistance is expected to be negligible.

Figure 4.21 shows a trend of increasing creep resistance with increasing temperature and decreasing pressure. Interestingly, negative differences of -20 to -40 % can be seen in the low temperature region ($T < 1425$ °C). A possible explanation could be related to the experimental creep rates at these temperatures. Uneven dispersion of aluminium in the creep samples, may influence if spinel formed prior to creep testing. It could be that, spinel did not form and hence did not improve creep resistance. This may have lead to the negative differences in this region. Even dispersion of aluminium should be achieved when fabricating the bricks, to ensure the material benefits globally (not locally) from the additions of aluminium.

Table 4.2 showed a spinel content of 1.3wt% at 1400 °C, and 1.6 wt% at 1500 °C. The improvement

in creep resistance and strength (HMOR and UCS), indicate the substantial contribution of spinel formation on the thermo-mechanical properties. It is expected that, with increasing aluminium content (PM-3% binder-3% Al), and hence increasing spinel content, thermomechanical properties will improve further. However, an optimum amount of spinel is required. Increasing spinel content to over 20% will most likely deteriorate thermomechanical properties, as was found by Ghosh et al. [9]. A high spinel content may lead to crack propagation due to a higher extend in micro cracking. This could explain the deterioration in strength. However, where this optimum lies for MgO-C refractories, remains to be investigated.

5

Conclusion and Recommendations

In this chapter, conclusions are drawn based on the experimental results. These are linked to the predefined research objectives. Thereafter, shortcomings in this work are solved for by stating recommendations for further research.

5.1. Conclusions

The main objective was to investigate the influence of binder and aluminium content on creep development in magnesia-carbon refractories. To achieve this objective, sub-objectives were defined:

- **To evaluate if a multi-stage creep test can shorten the creep testing campaign.**

In this work, five load stages were applied during creep testing. If all were within the secondary creep stage, and the load applied was >50% of the UCS, a maximum of five data points could be retrieved in 33 hours. As opposed to a single stage test, where only a maximum of one data point can be retrieved in the same time period. This result shows that the multi stage creep test can shorten the creep test campaign.

- **To validate data from a multi-stage creep test against a single-stage creep test**

The multi-stage creep testing method comes with the advantage of retrieving more data. However, with the experimental configuration assumed in the present study (5h per stage) the creep rates were overestimated compared to the single-stage creep test. However, a 5% difference in creep rates was observed. This indicates that the multi- and single-stage results are within range of each other. Therefore, the multi-stage creep test can be considered a viable creep testing method.

- **To quantify the effect of increasing binder content in MgO-C on creep development**

A trend of increasing creep resistance with increasing binder content was observed by analysing modelled creep data. Increasing the content from 2% to 3% showed an increase in creep resistance with decreasing temperature. Here, a 80% maximum decrease in creep rate was found. This behaviour is governed by volatilisation and carbonisation of the binder. An increase in volatilisation of the binder and magnesium for the PMC-2% binder recipe, weakened the bonds between the grains and subsequently the total material. This resulted in faster failure mechanisms, which was confirmed by the HMOR and UCS experiments. Weakening of the material decreased the grain boundary sliding resistance, and hence decreased the creep resistance. However, a low R^2 and large differences existed between experimental and modelled data for the PMC-2% binder recipe. This questioned the validity of the PMC-2% binder creep model. Experimental data at

high pressures (>8 MPa) and temperatures (>1500 °C) could not be retrieved for this recipe, as the material was too weak. The spread in experimental data points was therefore less compared to the other recipes, which can be a reason for the high amount of differences. Increasing binder content from 3% to 4% further showed to improve creep resistance. Here, a 30% maximum decrease in creep rate was found. The found trend of increasing creep resistance with increasing binder content is of significance, as it bridges the knowledge gap in refractory science.

- **To determine the contribution of spinel formation on the effective thermo-mechanical properties of the material**

Spinel contributed in increasing the effective thermo-mechanical properties. The XRD results showed an increase in spinel content from 0 wt% to 1.3 wt% at 1400 °C and 1.6 wt% at 1500 °C for the PMC-3% binder-1% Al recipe. Comparing results to the PMC-3% binder recipe, showed an increase in CCS by 15%. Furthermore, HMOR and UCS increased by 34% and 15% at 1400 °C (respectively) and 65% and 27% at 1500 °C (respectively). Spinel, due to its irreversible expansion, decreased porosity and increased the amount of microcracking. The former densified the material, and the latter restricted further crack propagation. As a result, the overall (hot) strength of the material increased. Increasing the aluminium content further, and hence the amount of formed spinel, from 1% to 3%, showed an increase in HMOR of almost 50%, and an increase in UCS of 10%. An increase of 33% in CTE was observed for a further increase in aluminium content as well.

- **To quantify the effect of increasing aluminium content in MgO-C on creep development**

Increasing aluminium content from 0 to 1% resulted in a decrease in creep rates. A maximum decrease in creep rate of 70% was observed. This was attributed to spinel formation. The irreversible volume expansion due to spinel formation, closes pores and increases the density of the material. In addition, the stress state within the material is increased due to the volume expansion. As a result, microcracks form which inhibit further crack propagation and grain boundary sliding. Furthermore, it might be that spinel entrapped impurities in its crystal lattice. This restricts formation of low melting phases, and hence improves creep resistance. However, the validity of this hypothesis requires further research.

This work has bridged the knowledge gap on the influence of binder and aluminium content on creep development. Furthermore, the substantial influence of spinel on the thermo-mechanical properties has been shown. A viable creep testing method has been proposed, which will improve the efficiency of creep testing in the future. The aforementioned outcomes are an important contribution to refractory science. However, further development of refractories is still necessary, especially due to the increasing pressure on the steelmaking sector to make its processes safer and more sustainable.

5.2. Recommendations

In this section, both the shortcomings of this work and suggestions for further research are discussed to determine which questions still need answering. Although this work already provides a novel insight in to understanding the influence of binder and aluminium content on creep behaviour, some improvements can be made to eliminate shortcomings and develop the process further in the future:

- **To decrease the overestimation of the creep rates**, the multi-stage creep test method needs to be re-evaluated. It is recommended to conduct creep experiments with 3 load stages, with each stage lasting 10 hours. Validation is required against a single-stage creep test, to check if the amount of overestimation is decreased. In addition, trial experiments where loads are increased with 1 MPa, instead of 2 MPa, could be conducted. This will provide more insight in to the creep development at intermediate pressures.
- **To increase the efficiency of creep testing**, it is recommended to determine the UCS of the tested material beforehand. This will provide a first insight in to the strength of the material, and

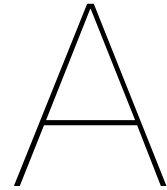
load stages can be defined accordingly.

- **To decrease the effect of sample heterogeneity**, a larger data set should be acquired. This is recommended for all conducted measurements in this work. Regarding creep testing, more data will further improve the quality of the model as well.
- **To assess the influence of further increasing the binder content beyond 4%**. The influence of increasing the binder content on creep development, has been defined within the 2% to 4% range. Beyond this range, further research is still required.
- **To further understand the influence of aluminium content on creep development**, it is recommended to perform more creep tests with aluminium-containing samples. Novel insights have now been provided about the influence of increasing the aluminium content from 0 to 1%. However, a knowledge gap remains on creep behaviour of recipes with a higher aluminium content.
- **To validate the hypothesis that spinel may act as a sponge**, thereby entrapping impurities in its crystal lattice. This might be achieved via SEM and EDS.
- **To further enhance the thermo-mechanical properties of the material**, how the aluminium particles are dispersed within the material needs to be assessed and optimised. Better dispersion will allow the material to benefit globally from the advantageous effects of aluminium carbide (whisker)formation. In this work, whiskers formed locally, and hence had no effect on the thermo-mechanical properties of the material. Better dispersion might possibly be achieved by allowing aluminium to form on the graphite before it is introduced during brick fabrication. This may for instance be achieved by heating up a mixture of aluminium chloride (salt) with graphite. Chloride may evaporate, and aluminium particles remain on the graphite. However, the validity of these arguments require further research and experimental work.

References

- [1] K. Andreev et al. "Compressive fatigue behaviour of refractories with carbonaceous binders". In: *Journal of the European Ceramic Society* 34.2 (Feb. 2014), pp. 523–531. ISSN: 09552219. DOI: [10.1016/j.jeurceramsoc.2013.08.011](https://doi.org/10.1016/j.jeurceramsoc.2013.08.011).
- [2] Yves Berthaud, Nicolas Schmitt, and J Poirier. *Thermomechanical Behaviour of Magnesia-Carbon Refractories*. Tech. rep. 1998. URL: <https://www.researchgate.net/publication/259296657>.
- [3] M. A.L. Braulio, L. R.M. Bittencourt, and V. C. Pandolfelli. "Selection of binders for in situ spinel refractory castables". In: *Journal of the European Ceramic Society* 29.13 (Oct. 2009), pp. 2727–2735. ISSN: 09552219. DOI: [10.1016/j.jeurceramsoc.2009.03.024](https://doi.org/10.1016/j.jeurceramsoc.2009.03.024).
- [4] M. A.L. Braulio et al. "Spinel-containing alumina-based refractory castables". In: *Ceramics International* 37.6 (2011), pp. 1705–1724. ISSN: 02728842. DOI: [10.1016/j.ceramint.2011.03.049](https://doi.org/10.1016/j.ceramint.2011.03.049).
- [5] D Bray. "Creep of refractories: mathematical modeling, New Development in Monolithic Refractories—Advances in Ceramics". In: *The American Ceramic Society* 30 (1995), pp. 69–80.
- [6] William Callister and David Rethwisch. *Fundamentals of Materials Science and Engineering: An Integrated Approach*. New York: John Wiley & Sons, 2018. ISBN: 978-1-119-17550-6.
- [7] A. Colin Cameron and Frank A.G. Windmeijer. "An R-squared measure of goodness of fit for some common nonlinear regression models". In: *Journal of Econometrics* 77.2 (Apr. 1997), pp. 329–342. ISSN: 0304-4076. DOI: [10.1016/S0304-4076\(96\)01818-0](https://doi.org/10.1016/S0304-4076(96)01818-0).
- [8] Roy J. Crawford and James L. Throne. "ROTATIONAL MOLDING POLYMERS". In: *Rotational Molding Technology* (2002), pp. 19–68. DOI: [10.1016/B978-188420785-3.50004-6](https://doi.org/10.1016/B978-188420785-3.50004-6).
- [9] A. Ghosh et al. "Effect of spinel content on the properties of magnesia-spinel composite refractory". In: *Journal of the European Ceramic Society* 24.7 (2004), pp. 2079–2085. ISSN: 09552219. DOI: [10.1016/S0955-2219\(03\)00353-4](https://doi.org/10.1016/S0955-2219(03)00353-4).
- [10] D Gruber and H Harmuth. "Steel Ladle Linings - Key Issues Regarding Thermomechanical Behaviour". In: *RHI Bulletin* (2014), pp. 19–23.
- [11] Henk Visser and Warbout Tesselaar. *Refractory course 2021: converter refractories*. Tech. rep. IJmuiden: Tata Steel Europe, 2021, pp. 8–18.
- [12] Vanessa Hopp et al. "Structure–property functions of inorganic chemical binders for refractories". In: *Materials* 14.16 (Aug. 2021). ISSN: 19961944. DOI: [10.3390/ma14164636](https://doi.org/10.3390/ma14164636).
- [13] Shengli Jin, Harald Harmuth, and Dietmar Gruber. "Compressive creep testing of refractories at elevated loads—Device, material law and evaluation techniques". In: *Journal of the European Ceramic Society* 34.15 (2014), pp. 4037–4042. ISSN: 09552219. DOI: [10.1016/j.jeurceramsoc.2014.05.034](https://doi.org/10.1016/j.jeurceramsoc.2014.05.034).
- [14] W Kingery. "Structure of crystals". In: *Introduction to Ceramics*. New York: John Wiley & Sons, 1960, pp. 81–139.
- [15] Rishabh Kundu and Ritwik Sarkar. "MgO-C Refractories: A Detailed Review of These irreplaceable Refractories in Steelmaking". In: 70 (Sept. 2021), pp. 46–55. URL: www.interceram-review.info.
- [16] Bruno Luchini et al. "On the nonlinear behavior of Young's modulus of carbon-bonded alumina at high temperatures". In: *Journal of the American Ceramic Society* 101.9 (Sept. 2018), pp. 4171–4183. ISSN: 15512916. DOI: [10.1111/jace.15575](https://doi.org/10.1111/jace.15575).
- [17] A. P. Luz et al. "Thermosetting resins for carbon-containing refractories: Theoretical basis and novel insights". In: *Open Ceramics* 3 (Sept. 2020). ISSN: 26665395. DOI: [10.1016/j.oceram.2020.100025](https://doi.org/10.1016/j.oceram.2020.100025).

- [18] A. G. Tomba Martinez et al. "Creep behavior modeling of silica fume containing Al₂O₃-MgO refractory castables". In: *Ceramics International* 38.1 (Jan. 2012), pp. 327–332. ISSN: 02728842. DOI: [10.1016/j.ceramint.2011.07.010](https://doi.org/10.1016/j.ceramint.2011.07.010).
- [19] L. Musante et al. "Mechanical behaviour of MgO-C refractory bricks evaluated by stress-strain curves". In: *Ceramics International* 38.5 (July 2012), pp. 4035–4047. ISSN: 02728842. DOI: [10.1016/j.ceramint.2012.01.062](https://doi.org/10.1016/j.ceramint.2012.01.062).
- [20] Deepak Prajapati, Sasmita Majhi, and Abhijit Mishra. "Material Selection for Plastic Products". In: *Reference Module in Materials Science and Materials Engineering* (Jan. 2022), pp. 379–387. DOI: [10.1016/B978-0-12-820352-1.00095-X](https://doi.org/10.1016/B978-0-12-820352-1.00095-X).
- [21] Q. H. Qin. "Introduction to the composite and its toughening mechanisms". In: *Toughening Mechanisms in Composite Materials* (Jan. 2015), pp. 1–32. DOI: [10.1016/B978-1-78242-279-2.00001-9](https://doi.org/10.1016/B978-1-78242-279-2.00001-9).
- [22] Raymond P Racher, Robert W Mcconnell, and Andreas Buhr. *Magnesium Aluminate Spinel Raw Materials for High Performance Refractories for Steel Ladles*. Tech. rep. 2009.
- [23] J Routbort et al. "Creep of Whisker-Reinforced Ceramics". In: 1991.
- [24] Soheil Samadi et al. "Statistical study of compressive creep parameters of an alumina spinel refractory". In: *Ceramics International* 46.10 (July 2020), pp. 14662–14668. ISSN: 02728842. DOI: [10.1016/j.ceramint.2020.02.267](https://doi.org/10.1016/j.ceramint.2020.02.267).
- [25] Ritwik Sarkar. *Refractory Technology: Fundamentals and Applications*. CRC Press, Nov. 2016. ISBN: 9781315368054. DOI: [10.1201/9781315368054](https://doi.org/10.1201/9781315368054).
- [26] Stefan Schachner et al. "Three stage creep behavior of MgO containing ordinary refractories in tension and compression". In: *Ceramics International* 45.7 (May 2019), pp. 9483–9490. ISSN: 02728842. DOI: [10.1016/j.ceramint.2018.09.124](https://doi.org/10.1016/j.ceramint.2018.09.124).
- [27] Charles A Schacht. *Refractories Handbook*. New York: Marcel Dekker Inc, 2004, pp. 369–394.
- [28] N. Schmitt, Y. Berthaud, and J. Poirier. "Tensile behaviour of magnesia carbon refractories". In: *Journal of the European Ceramic Society* 20.12 (2000), pp. 2239–2248. ISSN: 09552219. DOI: [10.1016/S0955-2219\(00\)00088-1](https://doi.org/10.1016/S0955-2219(00)00088-1).
- [29] W Schulle and J Ulbricht. *Influence of different carbonaceous binders on the properties of refractories*. Tech. rep. Freiberg: Institut für Silikatechnik Bergakademie, 1992, pp. 419–525.
- [30] K V Simonov et al. *Creep in periclase and magnesia-spinel refractories*. Tech. rep. All-Union Institute of Refractories, 1984, pp. 316–320.
- [31] Martin Stueckelschweiger et al. "Creep testing of carbon containing refractories under reducing conditions". In: *Ceramics International* 45.8 (June 2019), pp. 9776–9781. ISSN: 02728842. DOI: [10.1016/j.ceramint.2019.02.013](https://doi.org/10.1016/j.ceramint.2019.02.013).
- [32] Paul Tamis. *BOF Port Talbot, stresses in the refractory lining depending on scrap panel material: Pitch or Resin bonded*. Tech. rep. IJmuiden: Tata Steel Nederland, Apr. 2014, pp. 1–19.
- [33] Paul Tamis. *Calculations on the cooling rate of BOF IJmuiden*. Tech. rep. IJmuiden: Tata Steel, Nov. 2013, pp. 1–10.
- [34] Lucas Teixeira et al. "Experimental Investigation of the Tension and Compression Creep Behavior of Alumina-Spinel Refractories at High Temperatures". In: *Ceramics* 3.3 (Sept. 2020), pp. 372–383. ISSN: 25716131. DOI: [10.3390/ceramics3030033](https://doi.org/10.3390/ceramics3030033).
- [35] A. Terzic, Lj Pavlović, and A. Milutinović-Nikolić. "Influence of the phase composition of refractory materials on creep". In: *Science of Sintering* 38.3 (2006), pp. 255–263. ISSN: 0350820X. DOI: [10.2298/S0S0603255T](https://doi.org/10.2298/S0S0603255T).
- [36] I Vishnevskii et al. "Structure and creep of mullite-corundum refractories". In: 11 (1985), pp. 592–598.



Processing

A.1. Pressing of refractory bricks

Weighing the raw materials

An extractor hood is turned on above the scale and the raw materials are weighed accordingly. This set-up is shown in [Figure A.1](#)



Figure A.1: Weighing the raw materials

Mixing the raw materials

First, the dry materials (i.e. everything except for the binder) are mixed for 30-45 minutes until the mixture has warmed up to about 80-90 °C. Then, the binder is added and mixed with the dry material for 30 minutes and kept at a temperature of 80-85 °C. The mixer is shown in [Figure A.2](#).

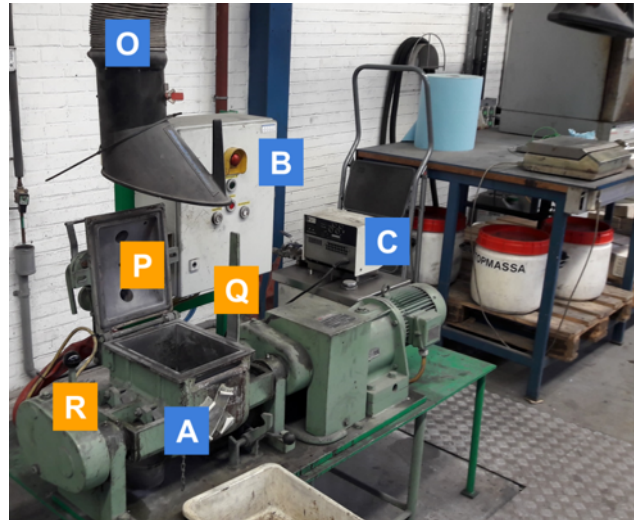


Figure A.2: Mixer (A) with operating cabinet (B), heating unit (C), extractor hood (O), cover (P), rod used to tip over and empty the mixer (Q) and security handle (R).

Pressing of the bricks using a hydraulic press

After mixing, the material is placed in the press. A stamp weighs down on the material and shapes it into bricks. The hydraulic press is shown in [Figure A.3](#). After pressing, the bricks are placed in an oven at 185 °C, at which the hexamethylenetetramine will react with the novolac binder. At this temperature the bricks will harden and form a rigid polymer network. The final resulting bricks are shown in [Figure A.4](#).



Figure A.3: Hydraulic press used to make the refractory bricks



Figure A.4: Final bricks after pressing

B

Materials and Methods


CRC Stenenpers - Persboek												
Recept	PMC-182											
Onderzoek	Effect %Resin & %Al-metal on creep behaviour MC											
Opmerking	MgO-C met 12% grafiet, 0% Al-metal en 2% hars											
Datum-tijd												
Lava												
Droogmengsel					1e deel voor 1e steen		2e deel voor 2e steen					
Grondstoffen	Korrel [mm]	Bak	Lava	Gehalte [%]	Richt [kg]	Afgewogen [kg]	Richt [kg]	Afgewogen [kg]				
Totaal					6.000		6.000					
1	FM97.8 (YAS)	0-0.25	213	17675	23.70	1.422	1.422	1.422				
2	FM97.8 (YAS)	0.25-1	214	17676	22.00	1.320	1.320	1.320				
3	FM97.8 (YAS)	1-2	215	17677	22.00	1.320	1.320	1.320				
4	FM97.8 (YAS)	2-4	216	17678	20.00	1.200	1.200	1.200				
5	Grafiet 92N		303	20256	12.00	0.720	0.720	0.720				
6	Al-metal			18554	0.00							
7	Hexa				0.20	0.012	0.012	0.012				
8												
9												
10												
11												
12												
Totaal				99.90	5.994	5.994	5.994	5.994				
Droogmengsel												
Mengtijd (richt 20:00 min)					45 min		45 min					
Temperatuur [°C]					87		86					
Binder												
13	Hars PF8505F			2.00	0.120		0.120					
Temperatuur [°C]					98		98					
- Begin gewicht [kg]					x	0.889	x	0.761				
- richt: toe te voegen [kg]					x	0.120	x	0.120				
- richt: eindgewicht [kg]					x	0.769	x	0.641				
- Eind gewicht [kg]					x	0.762	x	0.640				
- Toegevoegd [kg]					#VALUE!	0.127	#VALUE!	0.121				
Totaal				101.90	6.114	2.667	6.114	2.283				
Nat mengsel												
Mengtijd (richt 20:00 min)					30 min		30 min					
Temperatuur [°C]					90		85					
Stenenpersen												
Temperatuur matrijs [°C]					80		80					
Geperste steen												
Steen nummer/ID					PMC-182 #1		PMC-182 #2					
Gewicht [kg]					6.123		6.066					
Afmetingen												
- Lengte [cm]					150.5		150.55					
- Breedte [cm]					100.6		100.63					
- Hoogte [cm]					135.08		134.15					
Bulk dichtheid [kg/cm3]					2994		2985					

Figure B.1: Recipe for PMC-2% binder.


CRC Stenenpers - Persboek																
Recept	PMC-183															
Onderzoek	Effect %Resin & %Al-metal on creep behaviour MC															
Opmerking	MgO-C met 12% grafiet, 0% Al-metal en 3% hars															
Datum-tijd																
Lava																
Droogmengsel					1e steen		2e steen		3e steen							
Grondstoffen	Korrel [mm]	Bak	Lava	Gehalte [%]	Richt [kg]	Gewogen [kg]	Richt [kg]	Gewogen [kg]	Richt [kg]	Gewogen [kg]						
Totaal					6.000	6.000	6.000	6.000	6.000	6.000						
1	FM97.8 (YAS)	0-0.25	213	17675	23.70	1.422	1.422	1.422	1.422	1.422						
2	FM97.8 (YAS)	0.25-1	214	17676	22.00	1.320	1.320	1.320	1.321	1.320						
3	FM97.8 (YAS)	1-2	215	17677	22.00	1.320	1.320	1.320	1.320	1.320						
4	FM97.8 (YAS)	2-4	216	17678	20.00	1.200	1.200	1.200	1.200	1.200						
5	Grafiet 92N		303	20256	12.00	0.720	0.720	0.720	0.722	0.720						
6	Al-metal			18554	0.00											
7	Hexa				0.30	0.018	0.018	0.018	0.018	0.018						
8																
9																
10																
11																
12																
Totaal				100.00	6.000	6.000	6.000	6.000	6.000	6.000						
Droogmengsel																
Mengtijd					55 min		45 min		50 min							
Temperatuur [°C]					79		80?		80							
Binder																
13	Hars PF 8505F			3.00	0.180		0.180		0.180							
Temperatuur [°C]									93							
- Begin gewicht [kg]					X	1.017	X	0.829	X	1.027						
- richt: toe te voegen [kg]					X	0.180	X	0.180	X	0.180						
- richt: eindgewicht [kg]					X	0.837	X	0.649	X	0.847						
- Eind gewicht [kg]					X	0.838	X	0.649	X	0.849						
- Toegevoegd [kg]						0.179		0.180		0.178						
Totaal					103.00	6.180	6.179	6.180	6.183	6.180						
Nat mengsel																
Mengtijd					30 min		30 min		30 min							
Temperatuur [°C]					90		87		87							
Stenenpersen																
Temperatuur matrijs [°C]					80		80		80							
Geperste steen																
Steen nummer/ID					PMC-183 #1		PMC-183 #2		PMC-183 #3							
Gewicht [kg]					5.907		6.166		6.064							
Afmetingen																
- Lengte [mm]					150.53		150.75		150.50							
- Breedte [mm]					100.60		100.69		100.53							
- Hoogte [mm]					128.29		134.82		132.28							
Bulk dichtheid [kg/cm ³]					3041		3013		3030							

Figure B.2: Recipe for PMC-3% binder.


CRC Stenenpers - Persboek												
Recept	PMC-181											
Onderzoek	Effect %Resin & %Al-metal on creep behaviour MC											
Opmerking	MgO-C met 12% grafiet, 0% Al-metal en 4% hars											
Datum-tijd												
Lava												
Droogmengsel					1e deel voor 1e steen		2e deel voor 2e steen					
Grondstoffen	Korrel	Bak	Lava	Gehalte	Richt	Afgewogen	Richt	Afgewogen				
	[mm]			[%]	[kg]	[kg]	[kg]	[kg]				
Totaal					6.000		6.000					
1	FM97.8 (YAS)	0-0.25	213	17675	23.70	1.422	1.422	1.422				
2	FM97.8 (YAS)	0.25-1	214	17676	22.00	1.320	1.320	1.322				
3	FM97.8 (YAS)	1-2	215	17677	22.00	1.320	1.320	1.320				
4	FM97.8 (YAS)	2-4	216	17678	20.00	1.200	1.200	1.200				
5	Grafiet 92N		303	20256	12.00	0.720	0.720	0.721				
6	Al-metal			18554	0.00							
7	Hexa				0.40	0.024	0.024	0.024				
8												
9												
10												
11												
12												
Totaal				100.10	6.006	6.006	6.006	6.009				
Droogmengsel												
Mengtijd (richt 20:00 min)					45 min		45 min					
Temperatuur [°C]					86		90					
Binder												
13	Hars PF8505F			4.00	0.240		0.240					
Temperatuur [°C]												
- Begin gewicht [kg]							0.851	0.609				
- richt: toe te voegen [kg]							0.240	0.240				
- richt: eindgewicht [kg]							0.611	0.369				
- Eind gewicht [kg]							0.612	0.370				
- Toegevoegd [kg]					0.000		0.239	0.239				
Totaal				104.10	6.246	2.553	6.246	1.827				
Nat mengsel												
Mengtijd (richt 20:00 min)					30 min		30 min					
Temperatuur [°C]					95		90					
Stenenpersen												
Temperatuur matrijs [°C]					80		80					
Geperste steen												
Steen nummer/ID					PMC-181 #1		PMC-181 #2					
Gewicht [kg]					6.161		6.259					
Afmetingen												
- Lengte [cm]					150.52		150.65					
- Breedte [cm]					100.59		100.52					
- Hoogte [cm]					135.14		137.28					
Bulk dichtheid [kg/cm ³]					3011		3011					

Figure B.3: Recipe for PMC-4% binder.


CRC Stenenpers - Persboek								
Recept	PMC-184							
Onderzoek	Effect %Resin & %Al-metal on creep behaviour MC							
Opmerking	MgO-C met 12% grafiet, 1% Al-metal en 3% hars							
Datum-tijd								
Lava								
Droogmengsel					1e steen		2e steen	
Grondstoffen	Korrel [mm]	Bak	Lava	Gehalte [%]	Richt [kg]	Gewogen [kg]	Richt [kg]	Gewogen [kg]
Totaal					6.000		6.000	
1	FM97.8 (YAS)	0-0.25	213	17675	23.70	1.422	1.422	1.422
2	FM97.8 (YAS)	0.25-1	214	17676	22.00	1.320	1.320	1.320
3	FM97.8 (YAS)	1-2	215	17677	22.00	1.320	1.320	1.320
4	FM97.8 (YAS)	2-4	216	17678	20.00	1.200	1.200	1.200
5	Grafiet 92N		303	20256	12.00	0.720	0.720	0.720
6	Al-metal			18554	1.00	0.060	0.060	0.060
7	Hexa				0.30	0.018	0.018	0.018
8								
9								
10								
11								
12								
Totaal				101.00		6.060	6.060	6.060
Droogmengsel					45 min		45 min	
Mengtijd					86		85	
Temperatuur [°C]								
Binder					0.180		0.180	
13	Hars PF 8505F			3.00				
Temperatuur [°C]								
- Begin gewicht [kg]					0.647		0.865	
- richt: toe te voegen [kg]					0.180		0.180	
- richt: eindgewicht [kg]					0.467		0.685	
- Eind gewicht [kg]					0.467		0.687	
- Toegevoegd [kg]					0.180		0.178	
Totaal					104.00	6.240	6.240	6.238
Nat mengsel					30 min		30 min	
Mengtijd					85		85	
Temperatuur [°C]								
Stenenpersen					80		80	
Temperatuur matrijs [°C]								
Geperste steen					PMC-184 #1		PMC-184 #2	
Steen nummer/ID								
Gewicht [kg]					6.269		6.13	
Afmetingen								
- Lengte [mm]					150.50		150.55	
- Breedte [mm]					100.58		100.60	
- Hoogte [mm]					137.60		134.60	
Bulk dichtheid [kg/cm3]					3010		3007	

Figure B.4: Recipe for PMC-3% binder-1% Al.


CRC Stenenpers - Persboek												
Recept	PMC-186											
Onderzoek	Effect %Resin & %Al-metal on creep behaviour MC											
Opmerking	MgO-C met 12% grafiet, 3% Al-metal en 3% hars											
Datum-tijd												
Lava												
Droogmengsel					1e steen		2e steen					
Grondstoffen	Korrel [mm]	Bak	Lava	Gehalte [%]	Richt [kg]	Gewogen [kg]	Richt [kg]	Gewogen [kg]				
Totaal					6.000		6.000					
1	FM97.8 (YAS)	0-0.25	213	17675	23.70	1.422	1.422	1.422	1.422			
2	FM97.8 (YAS)	0.25-1	214	17676	22.00	1.320	1.320	1.320	1.320			
3	FM97.8 (YAS)	1-2	215	17677	22.00	1.320	1.320	1.320	1.320			
4	FM97.8 (YAS)	2-4	216	17678	20.00	1.200	1.200	1.200	1.200			
5	Grafiet 92N		303	20256	12.00	0.720	0.720	0.720	0.720			
6	Al-metal			18554	3.00	0.180	0.180	0.180	0.180			
7	Hexa				0.30	0.018	0.018	0.018	0.018			
8												
9												
10												
11												
12												
Totaal				103.00	6.180	6.180	6.180	6.180				
Droogmengsel												
Mengtijd					45 min		45 min					
Temperatuur [°C]					85		83					
Binder												
13	Hars PF 8505F			3.00	0.180	0.180	0.180					
Temperatuur [°C]												
- Begin gewicht [kg]					X	0.680	X	0.497				
- richt: toe te voegen [kg]					X	0.180	X	0.180				
- richt: eindgewicht [kg]					X	0.500	X	0.317				
- Eind gewicht [kg]					X	0.500	X	0.316				
- Toegevoegd [kg]						0.180		0.181				
Totaal				106.00	6.360	6.360	6.360	6.361				
Nat mengsel												
Mengtijd					30 min		30 min					
Temperatuur [°C]					88							
Stenenpersen												
Temperatuur matrijs [°C]					80		80					
Geperste steen												
Steen nummer/ID					PMC-186 #1		PMC-186 #2					
Gewicht [kg]					6.342		6.318					
Afmetingen												
- Lengte [mm]					150.60		150.60					
- Breedte [mm]					100.60		100.65					
- Hoogte [mm]					140.00		139.50					
Bulk dichtheid [kg/cm ³]					2990		2988					

Figure B.5: Recipe for PMC-3% binder-3% Al.

C

Results experiments

C.1. Microstructural characterisation

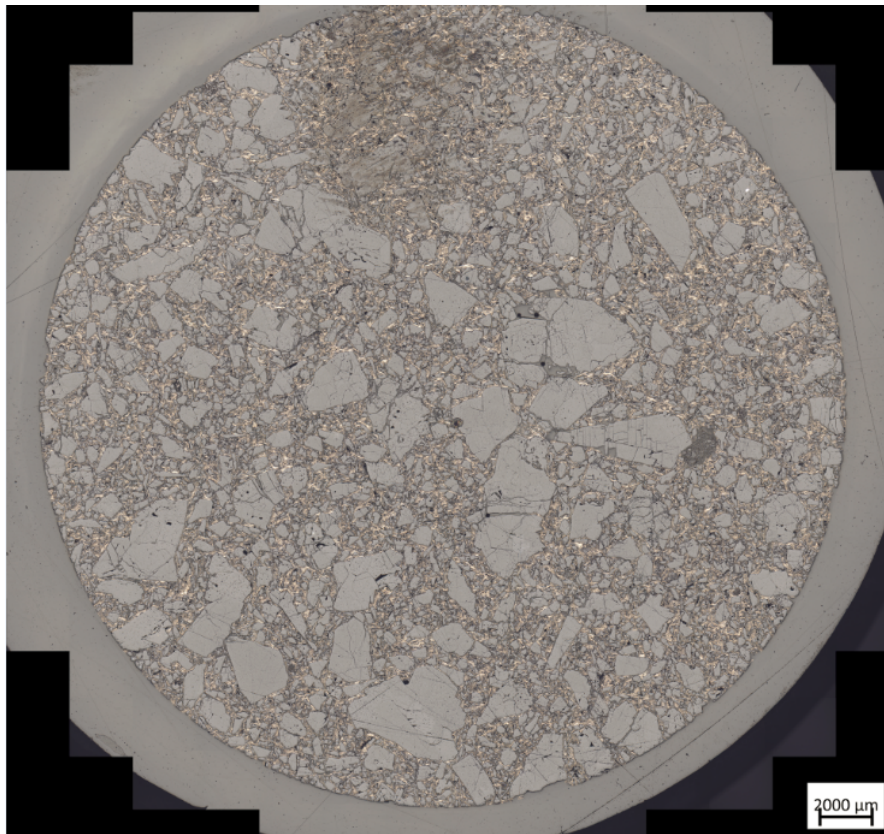
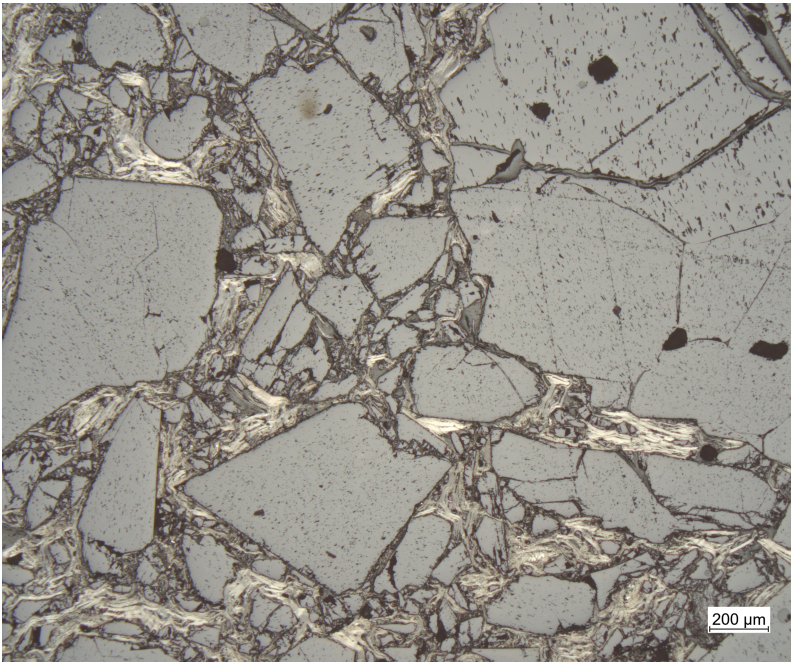


Figure C.1: Detailed overview of a green PMC-3%-binder sample. Taken at magnification of 5 times.



(a) Detailed grains of a green PMC-3%-binder sample. Taken at magnification of 5 times.

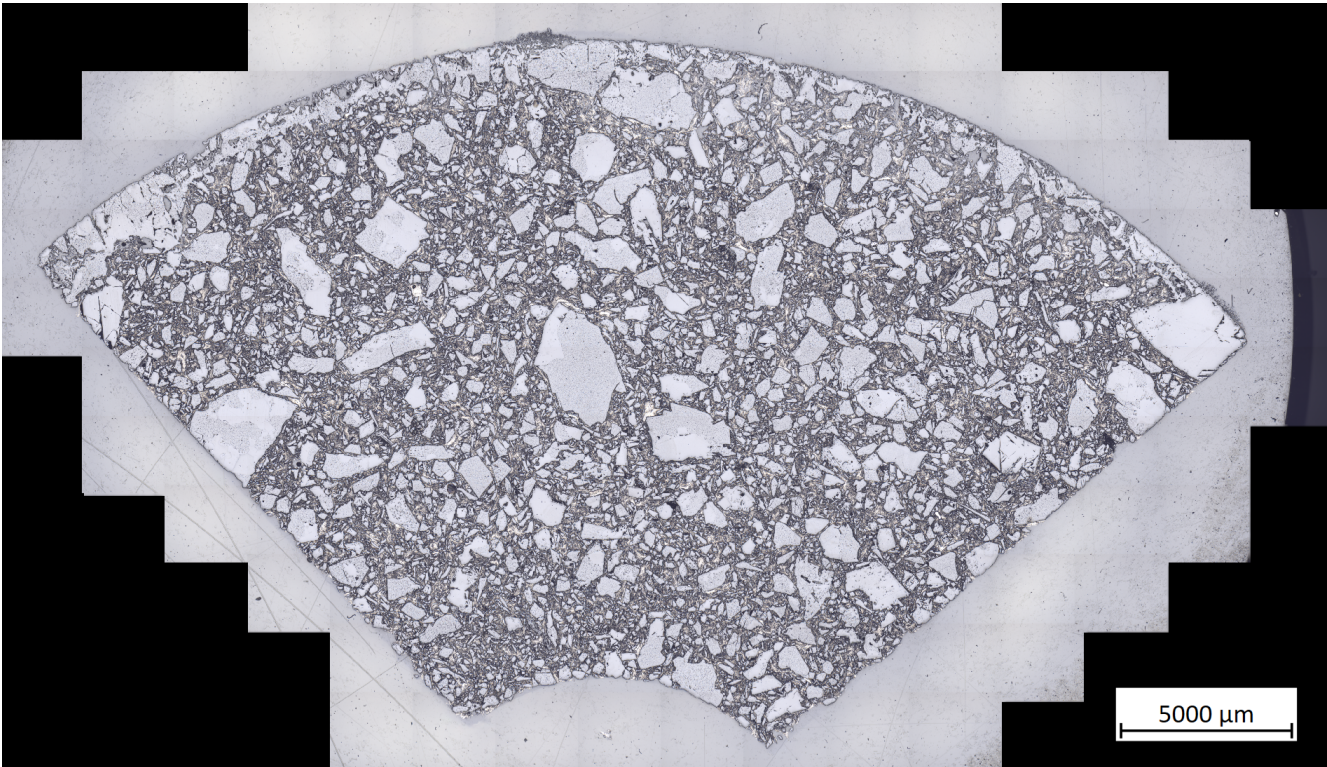


Figure C.3: Mozaic image of a PMC-3%-binder sample that has been fired at 1600 °C.

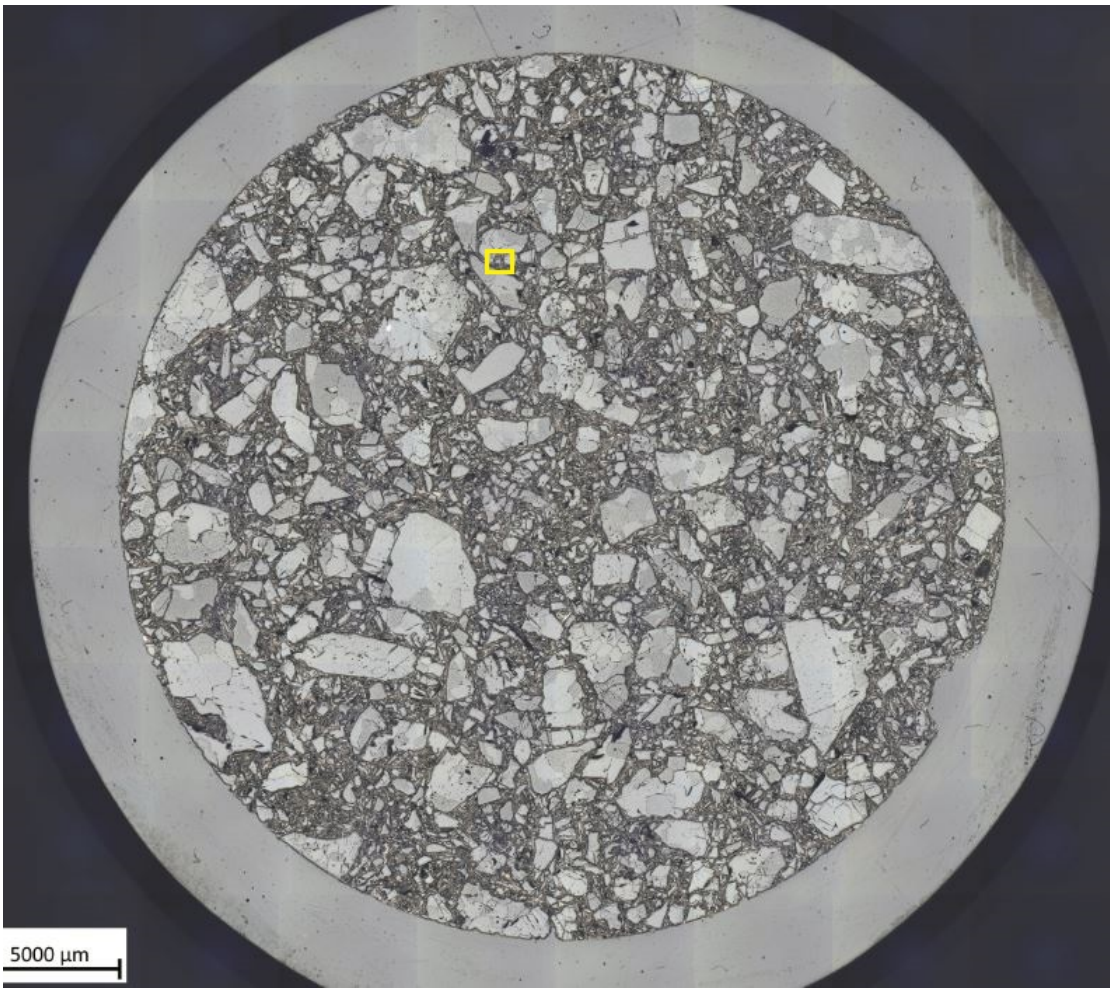


Figure C.4: Mozaic image of a PMC-3% binder-1% Al sample that has been fired at 1500 °C. Yellow square indicates location where SEM was performed.

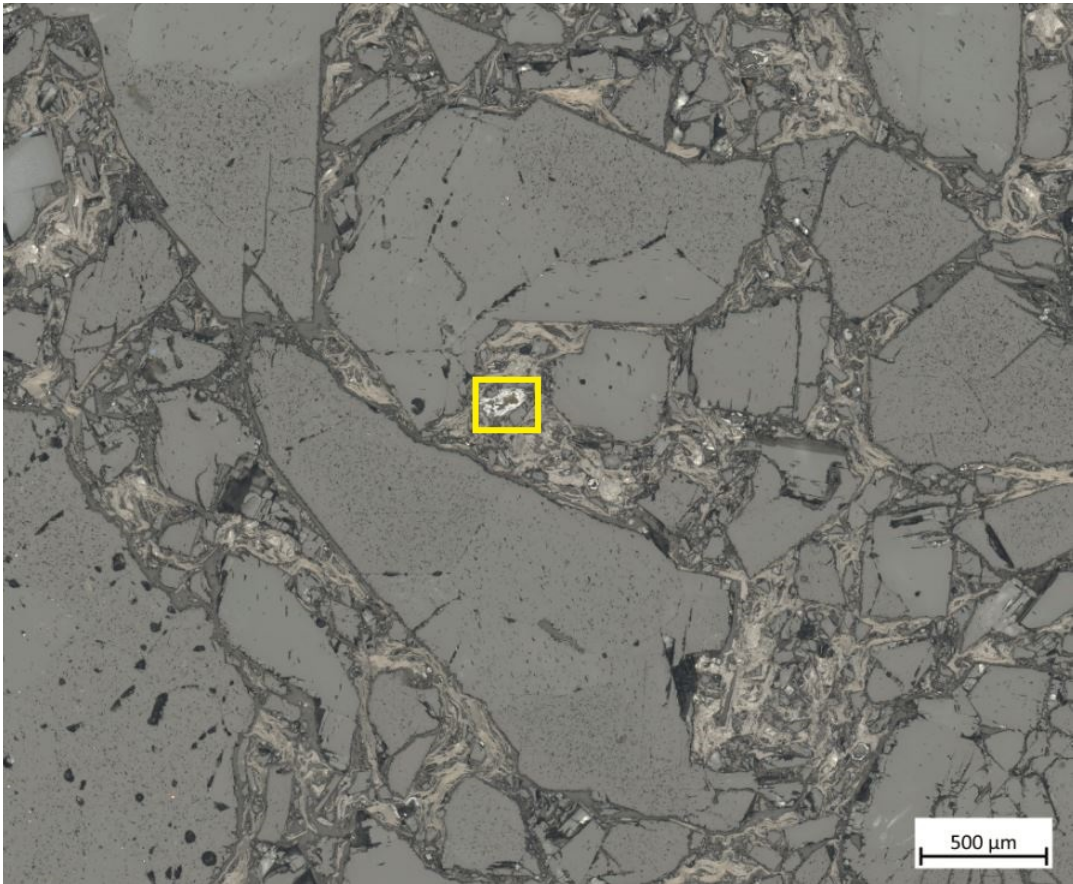
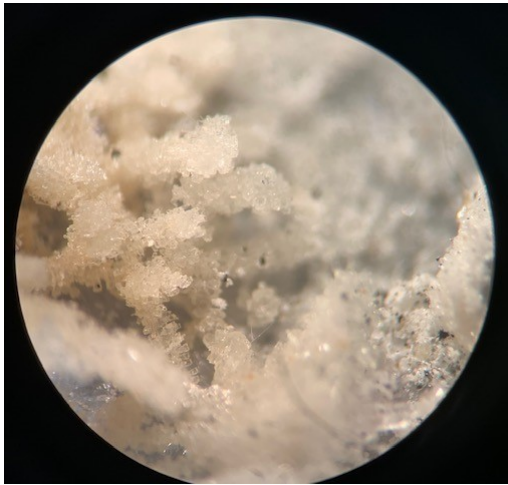


Figure C.5: Image of a PMC-3% binder-1% Al sample that has been fired at 1500 °C. Yellow square indicates location where SEM was performed.



(a) PMC-2% binder sample after creep testing. Magnesium volatilised and deposited as magnesia "needles" on to the sample.



(b) Stereoscopic image of the magnesia needles.

Figure C.6: PMC-2% binder sample after creep testing.

C.2. XRD

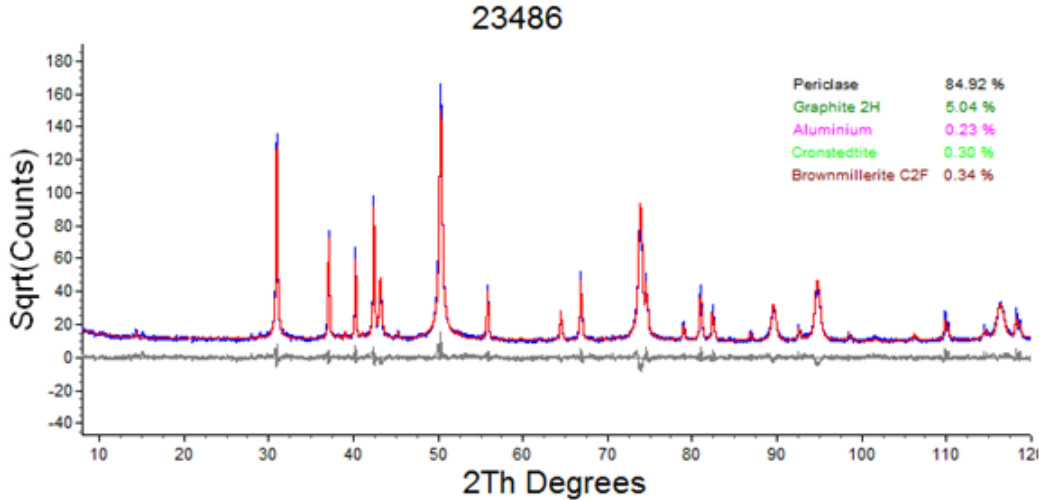


Figure C.7: Recorded and fitted X-ray pattern along with phase proportions of green PMC-2%-binder sample. Reported Rwp=10.59

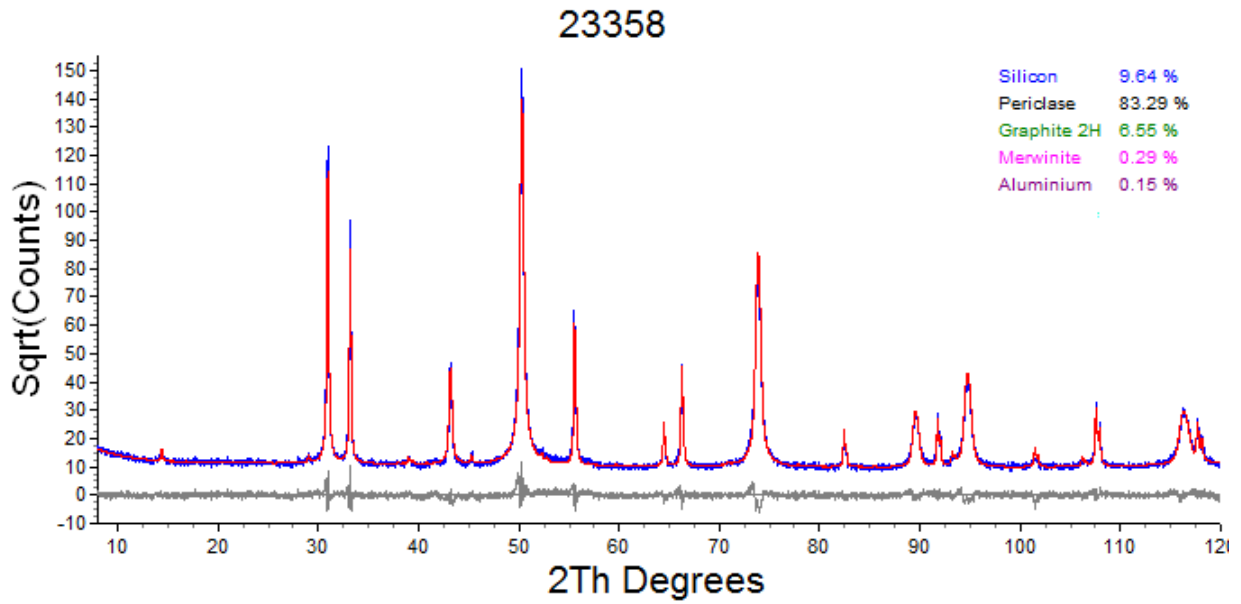


Figure C.8: Recorded and fitted X-ray pattern along with phase proportions of green PMC-3%-binder sample. Reported Rwp=9.54

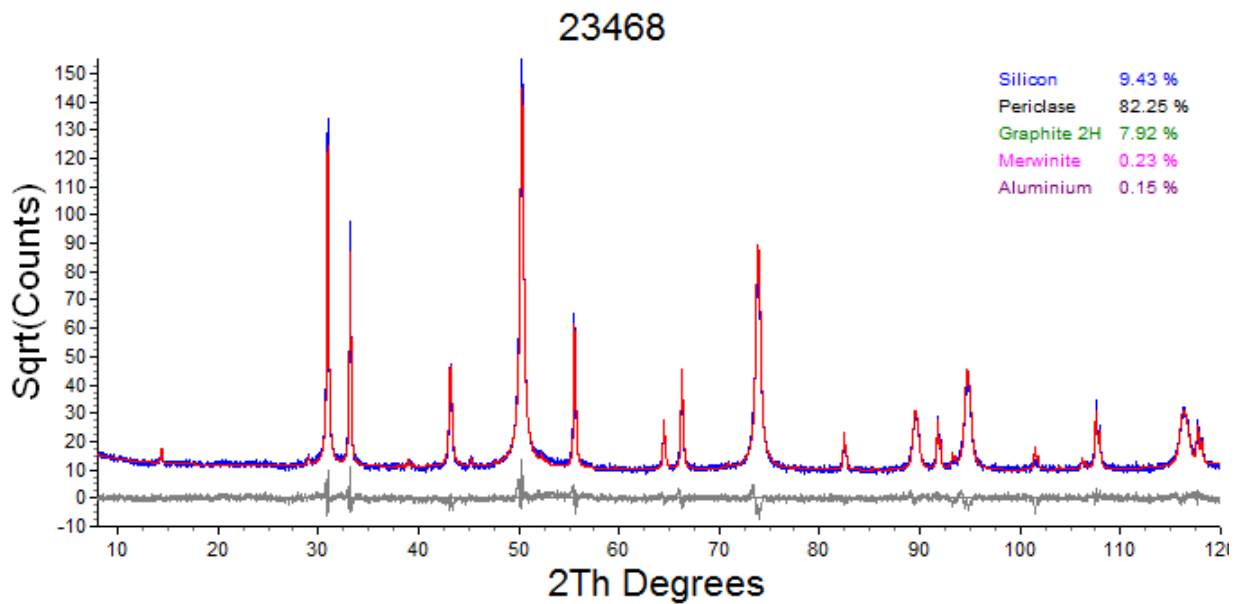


Figure C.9: Recorded and fitted X-ray pattern along with phase proportions of green PMC-4%-binder sample. Reported Rwp=9.91

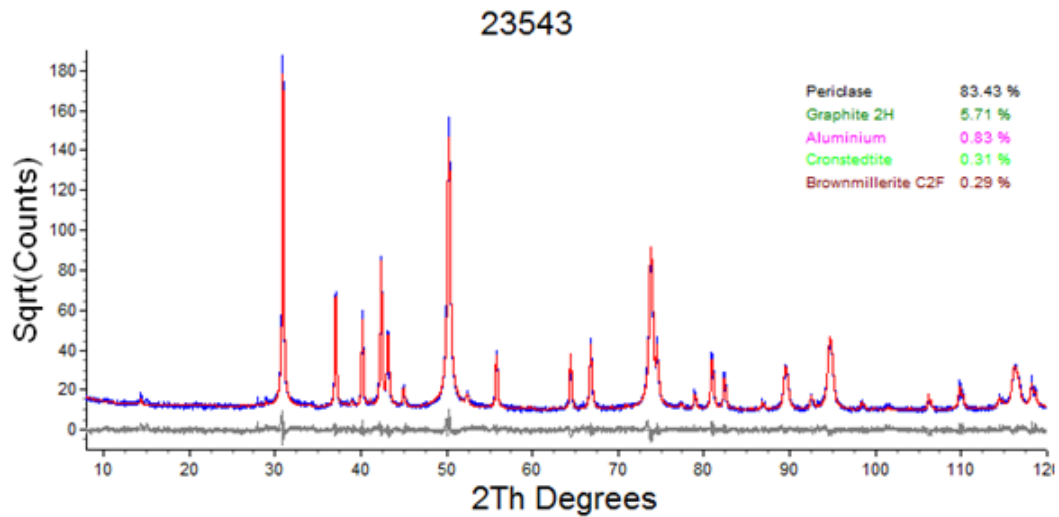


Figure C.10: Recorded and fitted X-ray pattern along with phase proportions of green PMC-3% binder-1% Al sample. Reported Rwp=8.39

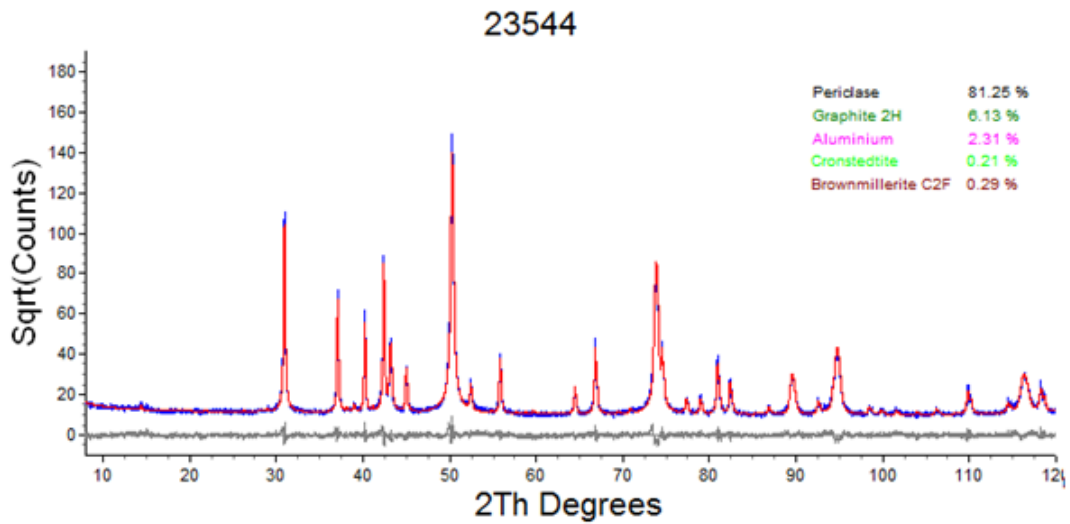


Figure C.11: Recorded and fitted X-ray pattern along with phase proportions of green PMC-3% binder-3% Al sample. Reported Rwp=8.47

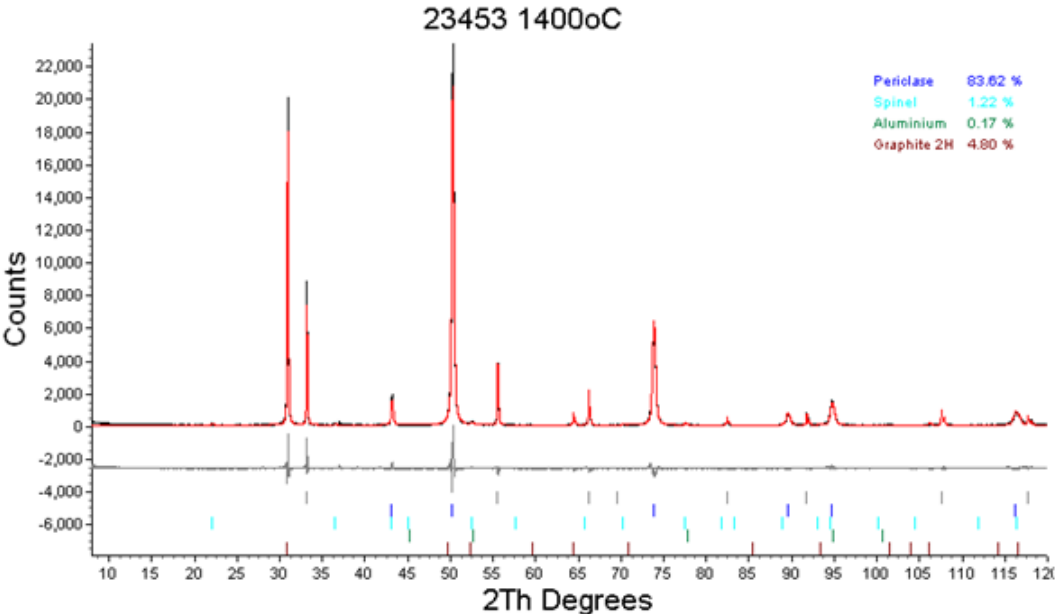


Figure C.12: Recorded and fitted X-ray pattern along with phase proportions of pre-treated PMC-3% binder-1% Al sample.

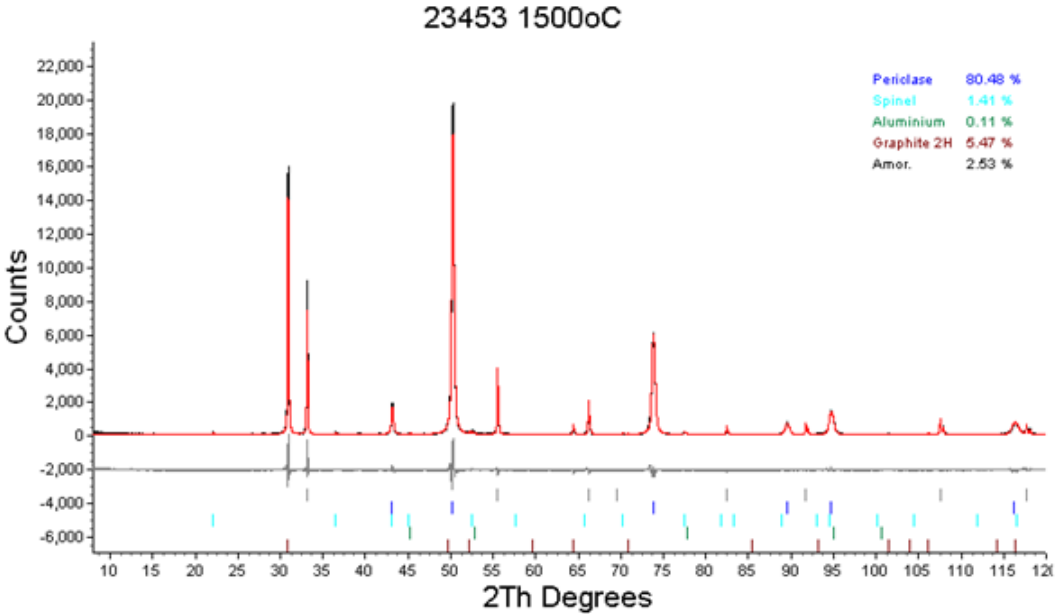


Figure C.13: Recorded and fitted X-ray pattern along with phase proportions of pre-treated PMC-3% binder-1% Al sample.

C.3. Refractoriness under load

RuL curve PMC-2% binder

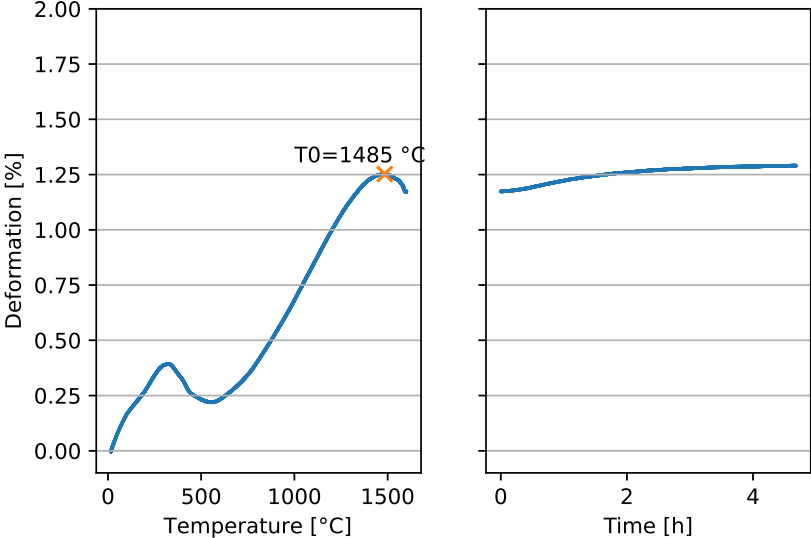


Figure C.14: Refractoriness under load curve of a PMC-2% binder sample.

RuL curve PMC-3% binder

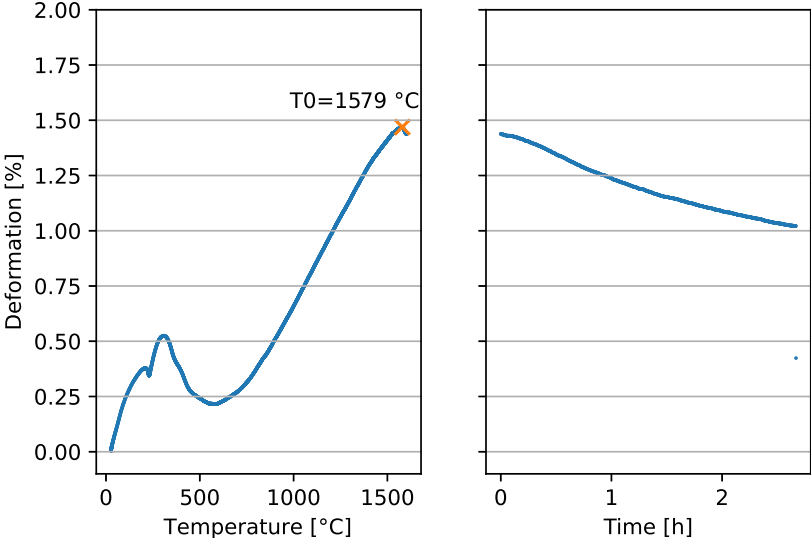


Figure C.15: Refractoriness under load curve of a PMC-3% binder sample.

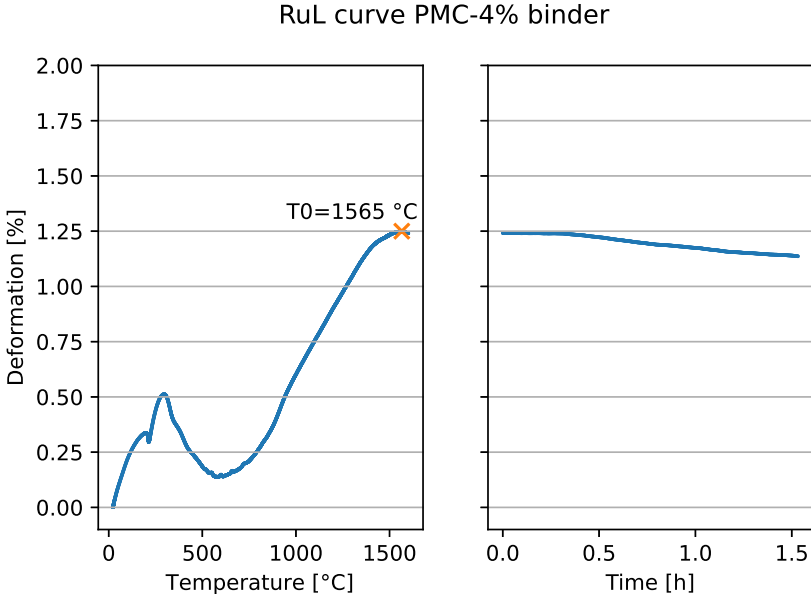


Figure C.16: Refractoriness under load curve of a PMC-4% binder sample.

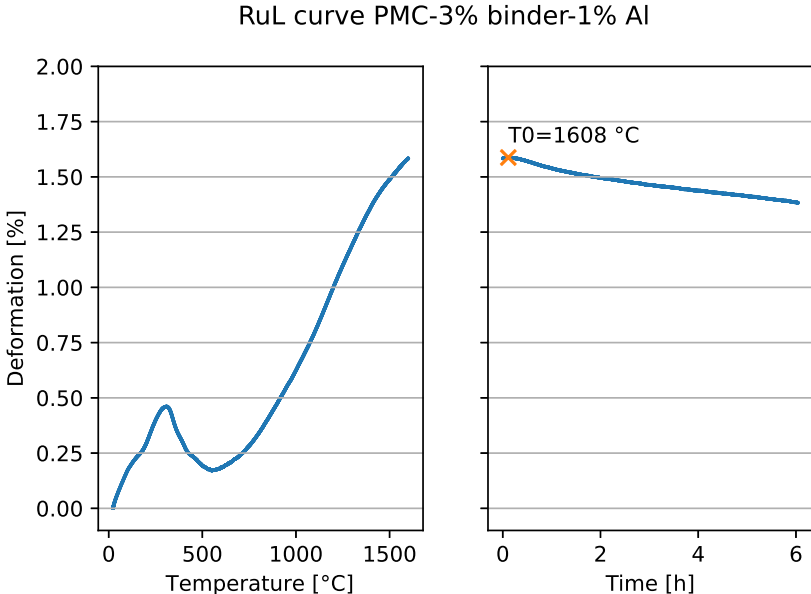


Figure C.17: Refractoriness under load curve of a PMC-3% binder-1% Al sample.

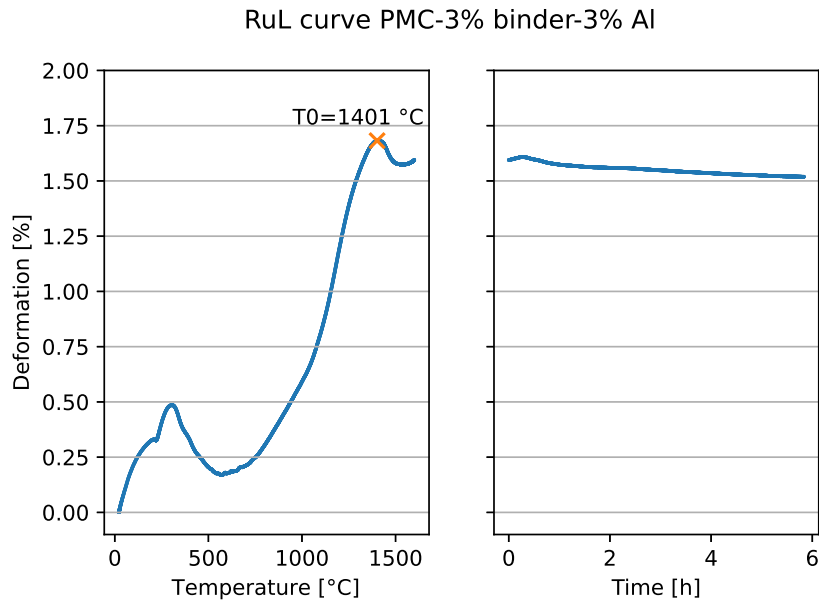


Figure C.18: Refractoriness under load curve of a PMC-3% binder-3% Al sample.

C.4. Hot compressive strength

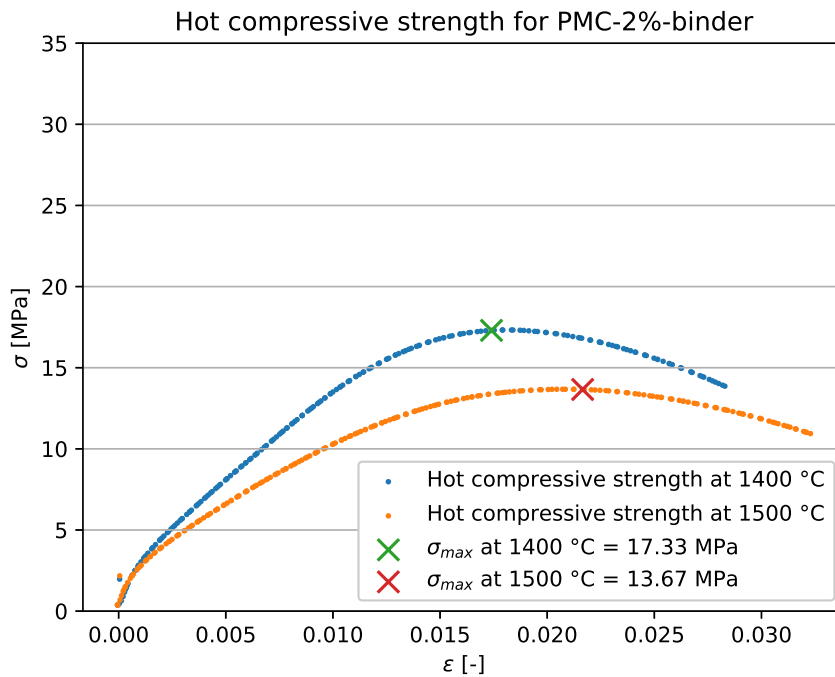


Figure C.19: Hot compressive strength, tested at 1400 and 1500 ° for PMC-2% binder.

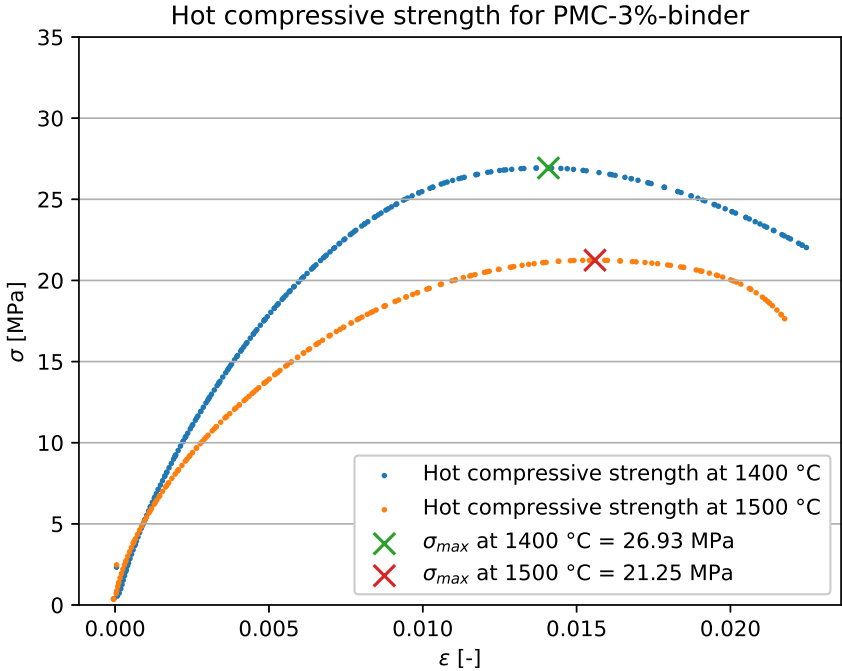


Figure C.20: Hot compressive strength, tested at 1400 and 1500 °C for PMC-3% binder.

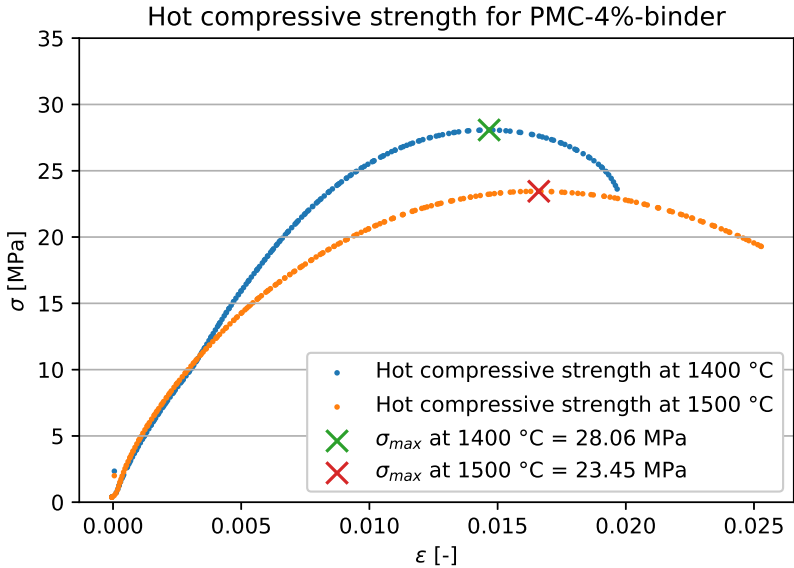


Figure C.21: Hot compressive strength, tested at 1400 and 1500 °C for PMC-4% binder.

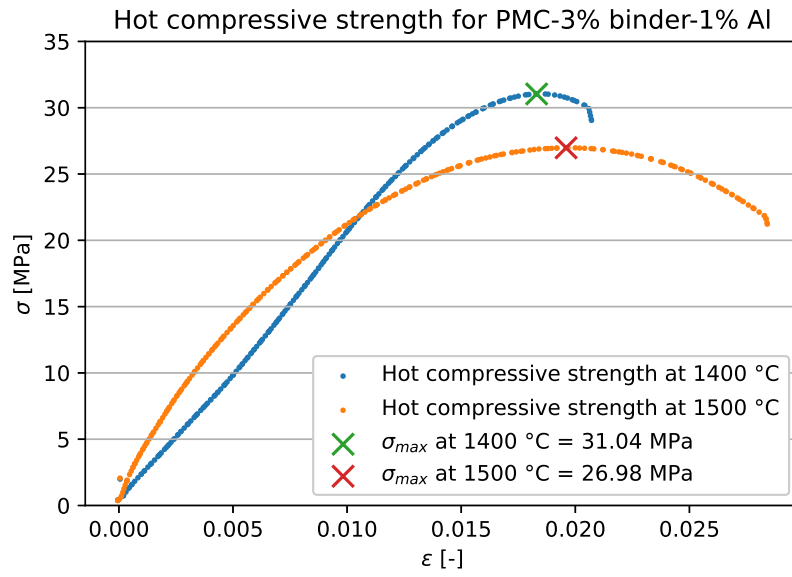


Figure C.22: Hot compressive strength, tested at 1400 and 1500 °C for PMC-3% binder-1% Al.

C.5. Creep in compression

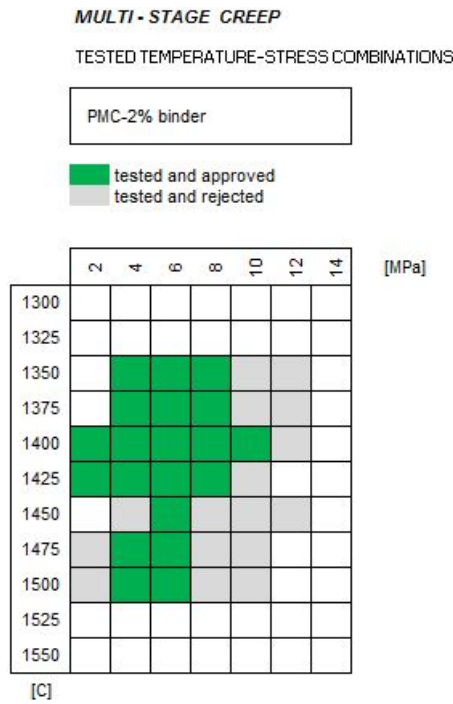


Figure C.23: Accepted and rejected data for PMC-2% binder recipe.

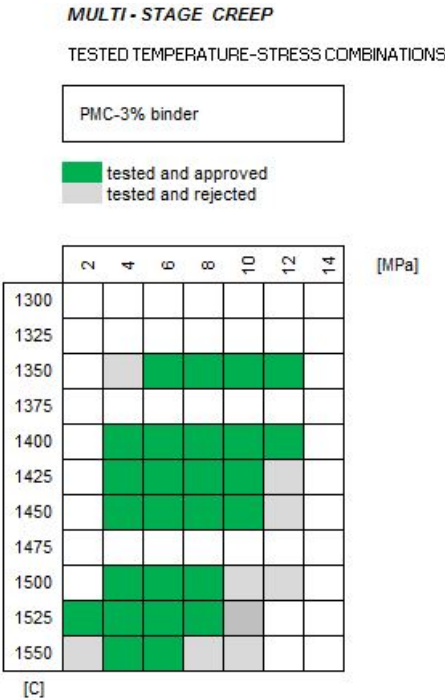


Figure C.24: Accepted and rejected data for PMC-3% binder recipe..

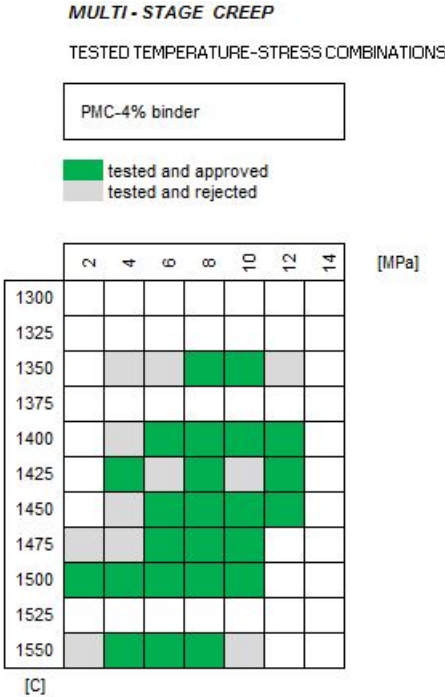


Figure C.25: Accepted and rejected data for PMC-4% binder recipe.

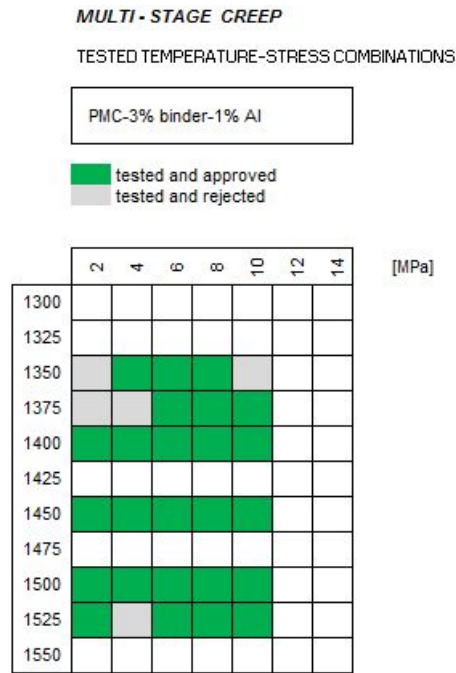


Figure C.26: Accepted and rejected data for PMC-3% binder-1% Al recipe.

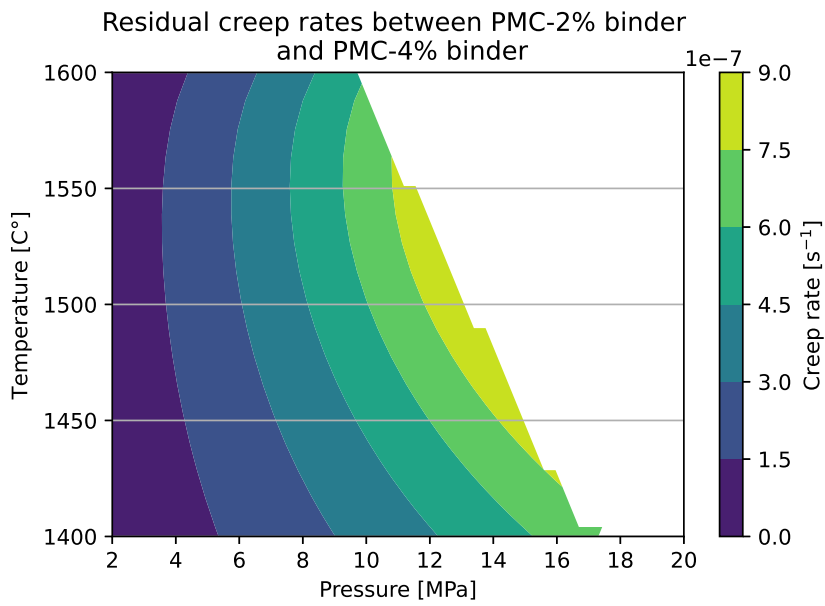


Figure C.27: Residual modelled creep rates. Determined by subtracting rates from PMC-4% binder from PMC-2% binder data.

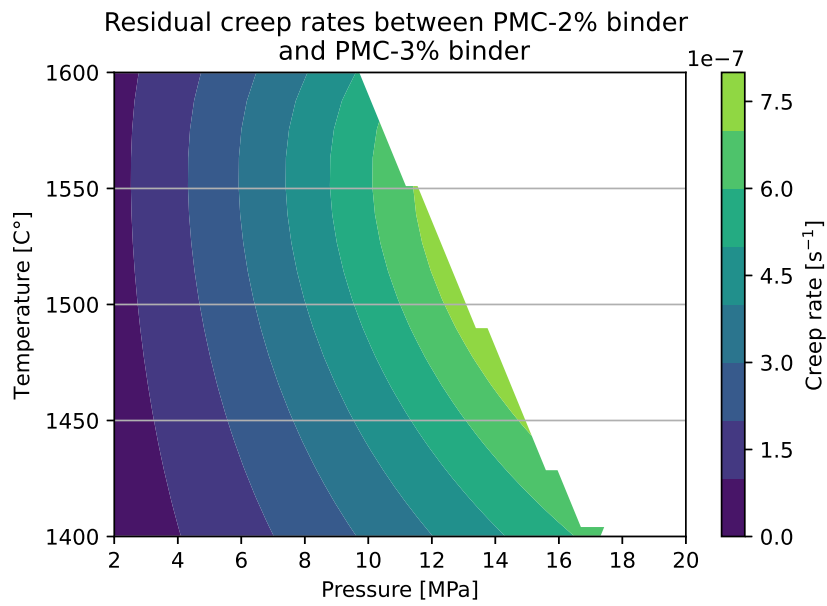


Figure C.28: Residual modelled creep rates. Determined by subtracting rates from PMC-3% binder from PMC-2% binder data.

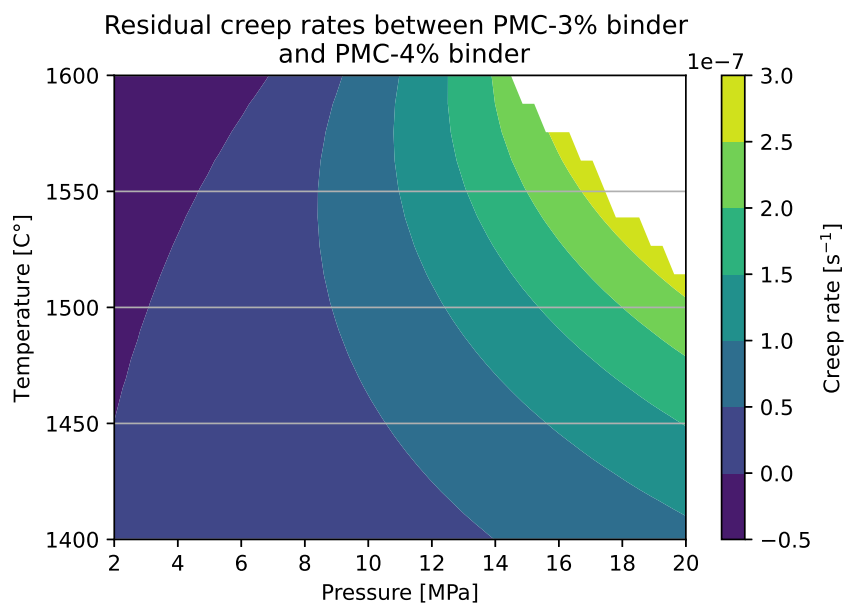


Figure C.29: Residual modelled creep rates. Determined by subtracting rates from PMC-4% binder from PMC-3% binder data.